Design of Visible-light driven catalysts for water oxidation and VOC degradation

Politecnico di Torino

Faculty of Engineering

December-2014

PhD Thesis

In Chemical Engineering

Design of Visible-light driven catalysts for water oxidation and VOC degradation

Thalluri Sitaramanjaneya Mouli

Mentor: Professor Nunzio Russo

Department of Science and Technology

Corso Duca degli Abruzzi 24, 10129 Torino, Italy

Acknowledgments

This thesis is written as completion to the Doctor of Philosophy in Chemical Engineering at Politecnico di Torino. This Ph.D. thesis has been carried out in the Department of Applied Science and Technology (DISAT) of Politecnico di Torino (PoliTo) in cooperation with the Italian Institute of Technology (IIT) as part of the European Project Eco^2CO_2 under the guidance of Prof. Guido Saracco and Prof. Nunzio Russo (PoliTo).

I would like to thank to my instructors and supervisor in Italy for their meaningful guidance. In addition, I would like to thank to Dr. Simelys Hernandez(IIT) and Dr. Svetoslava Vankova in PoliTo for their day to day support and advice in the laboratory, which was vital in the achievement of the current thesis. Furthermore, I kindly thank to PhD Samir Bensaid (PoliTo) for his advice in applying the mathematical model and discussions of the project. Likewise, I truthfully express my gratitude to everyone else in PoliTo and IIT, who gave me their support in so many different manners and occasions in these years of my stay at PoliTo. It would have been really hard to get to this point without your help and company. Finally I would like to thankful to my family members for their support during my PhD.

Contents

Preface

The objectives of the present work are given as prescribed in the Fig. IThe whole figure describes the strategy to be followed to complete two projects in our group. Out of the complete description in the fig. my thesis includes first two processes, comprising of morphology control of the *$BiVO_4$*, doping with Molybdenum and Tungsten and thin film fabrication using dip coating as well as spin coating procedures.

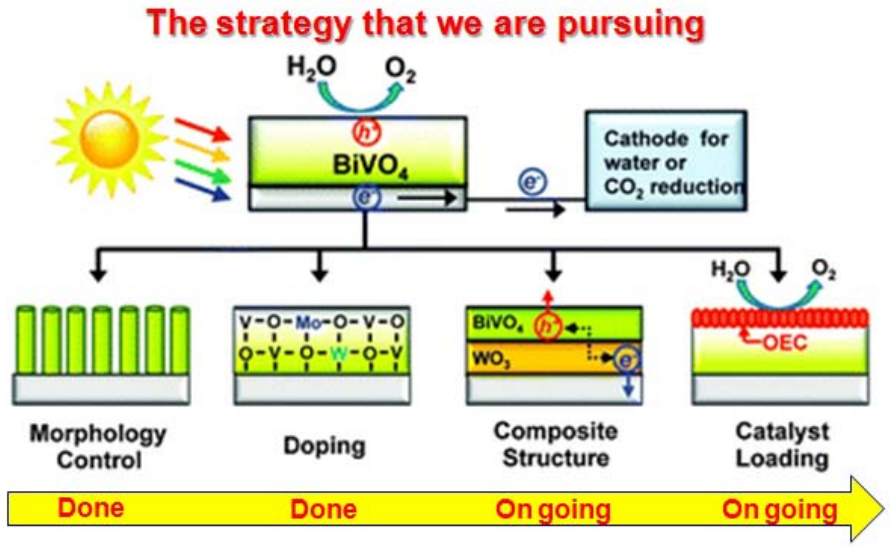

Figure: IThe detailed description of the chapters is stated below with a small overview.

Heterogeneously dispersed semiconductor surfaces provide both a fixed environment to influence the chemical reactivity of a wide range of adsorbates and a means to initiate light-induced redox reactivity in these weakly associated molecules. Upon photoexcitation of several Semiconductors non-homogeneously suspended in either aqueous or nonaqueous solutions or in gaseous mixtures, simultaneous oxidation and reduction reactions occur. This conversion often accomplishes either a specific, selective oxidation or a complete oxidative degradation of an organic substrate present. Molecular oxygen is often assumed to serve as the oxidizing agent although details about the mode of its involvement have not been unambiguously demonstrated except in a few gas/solid reactions. The incident light that initiates this sequence is in a wavelength region (the visible or low-energy range of the ultraviolet regions of the spectrum) absorbed by the semiconductor rather than by the substrate of interest. These reactions therefore involve photosensitization, i.e., an indirect photoactivation of the heterogeneously dispersed particulate absorber rather than the direct formation of an excited state of the substrate. Furthermore, the suspended semiconductor particle that acts asthe photocatalyst is often stable to the photolysis conditions (particularly when a metal oxide is employed) and a large number of oxidative conversions per active site on the catalyst can be attained without significant degradation of the semiconductor's redox catalytic capacity. For these reasons, such semiconductor-mediated redox reactions are often grouped under the rubric of heterogeneous photocatalysis.

The Present PhD Thesis involves one or more articles that are either published, submitted or on their way of manuscript preparation. These all chapters are placed in context to the understandings and advancements involved in the PhD period. The whole thesis

involves insights about synthesis and characteristics of $BiVO_4$ in the form of powder as well as thin films. It also describes their influence in the efficiency of the material.

In chapter 3 the reader had introduced the important parameters of the material in powder form which are important for $BiVO_4$ when considered about the water oxidation. These parameters were considered to be the primary aspects of the material $BiVO_4$ considering water oxidation. This chapter uses a simple method of synthesis conditions with cost effective materials. Further it has been concluded that the band gap, crystalline size and *V-O* bond length are some of the primary parameters that were considered to be important with respect to water oxidation. The insights from anneling temperature with crystalline size were observed and it over all influence over the activity is deduced.

Chapter 4 and 5 deals with the secondary parameter of $BiVO_4$, which had also some influence over the activity. This is evaluated by altering the synthesis conditions in terms of the initial precursor solution. Here the *pH* of the precursor solution is varied keeping the rest of the conditions uniform. It had been observed that the *pH* had an influence over the crystalline faces of the $BiVO_4$. In this chapter the focus was towards the two peaks of XRD which corresponds to the crystal facets labeled as (011) and (040) of the system of $BiVO_4$. The *pH* of the system has an influence on (040) peak of XRD. The *pH* of the precursor solution increases, the (040) peak of the crystal system increases. In chapter 4 it has been discussed the influence of the (040) with the water oxidation activity of the $BiVO_4$. Here it has been showed to have a positive influence of (040) over the water oxidation activity of the system. In chapter 5, the same system of $BiVO_4$ influence over the volatile organic compound decomposition was evaluated. The details about the degradation of ethylene was explained and it is in favor to the (040) crystal plane.

Chapter 6 discusses about the doping properties of the $BiVO_4$. Here in we verified the importance of the doping characteristics of the $BiVO_4$ with enhanced (040) crystal planes. The doping of the system is carried with Tungsten and Molybdenum. In this chapter it has been elucidated the physical properties and the optical properties of $BiVO_4$ undoped and doped with $W^{6+1}wt$,$W^{6+5}wt$, $Mo^{6+1}wt$ and $Mo^{6+5}wt$ into the V^{5+} sites presents in the $BiVO_4$ lattice. Then a photocatalytic O_2 evolution study was performed and correlated with the physical and optical changes. In order to have a more practical system, the fabrication of a $BiVO_4$ photoanode is a practical alternative for the design and construction of the photocatalytic devices. The second part of this work in this chapter refers to the study of $BiVO_4$ electrodes, using the $BiVO_4$ powder prepared by hydrothermal synthesis (HTS), conventional slurry (CS) method for its fabrication and a method called doctor blade for the final deposition of the slurry in the electrode.

In chapter 7 the description of in-situ synthesis of electrode system is studied on a FTO electrode.The deposition of Bismuth Vanadate thin films onto FTO glass electrodes using a simple dip coating procedure is reported herein. The importance of the thickness of the films is highlighted. Details regarding the influence of the thickness on the photo-electrochemical performance for the water splitting reaction have been explained through electrochemical impedance spectroscopy. It has been found that the thickness of the electrode should be around (160 *nm*) in order to obtain a maximum photo-current density of about 0.57 $mA.cm^{-2}$at 1.23 *V* vs. RHE under sunlight illumination.

As of now in this thesis work I improved the current produced without the process of doping to a considerably efficient value which can be improved by further modification and which is in the progress. The present system can be helpful to exploit the sunlight and produce

a current of 0.6 $mA.cm^{-2}$ in 0.1M Na_2SO_4 solution with an applied bias of 1.23 V which is considered as an acceptable potential that can be applied for the process of hydrogen production on the counter electrode in a photo-electrochemical cell. When we compared this with the solar energy efficiency its approximately 1% conversion efficiency deduced from the formulae. $\eta = \mathrm{I}\left(mA/_{cm^{-2}}\right) * \vartheta_{app}\,(V) \Big/ \mathrm{P}\left(mW/_{cm^{-2}}\right)$

1. Chapter 1. Introduction

1.1. Needs and Sources of Energy

As the developed world becomes more populated and that population depends more on technology, energy demand is set to rise. This is illustrated by the rapid growth in energy consumption throughout the world. At the start of the millennium, global energy consumption was estimated to be at around 13 TW.(1, 2)This value is expected to double to almost 27 TW by 2050.(2)The majority of the current demand (around 85 %) is being met by fossil fuels,(3)such as coal and oil, which are decreasing in availability. It is clear from these two points alone that other energy sources are needed, not only to satisfy this increasing demand, but also to replace those sources which are depleting.

Another potential problem in the current age is that of global warming which is commonly accepted to be linked to an increase in the levels of greenhouse gases in the atmosphere. Although there are many greenhouse gases, water included, carbon dioxide attracts the most attention as since the 18th century and the time of the industrial revolution, CO_2 emissions have increased phenomenally, causing a 25 % increase in atmospheric levels.(4)It is being produced constantly from combustion of fossil fuels in power stations and in transport. Thus, there is a clear incentive for the development of processes and energy carriers that have reduced CO_2 emissions, as evidenced by UK government legislation as well as EU initiatives such as the 2020 target. Alternatives have been investigated and implemented on smaller scales over the years. Various methods have used the naturally occurring phenomena, for example, wind, tidal or geothermal. However, due to comparatively low energy production or high cost, such methods can only provide a small percentage of the energy demand.(1)A larger scale and more energy efficient process of energy production is that of nuclear energy. This, however, clearly has environmental implications of its own, namely the disposal of spent uranium and plutonium fuel, currently achieved by burying underground. There is also the high risk of operating nuclear reactors, highlighted by the Chernobyl disaster in Ukraine in 1986(5)and the Fukushima plant in Japan, following the 2011 earthquake.

Hydrogen has been identified as a possible clean alternative fuel to potentially lessen our dependence on fossil fuels,(6)due to the fact that its combustion only produces water, therefore rendering it carbon neutral.

1.2. The Sun and Sunlight

In this section of the literature review an introduction to the main aspects concerning the production of solar fuels is given. In general, three questions will be answered throughout the subsections, namely why is the development of solar fuels relevant in the current energy and environmental scenario. Furthermore, a brief explanation of the solar fuels concept is introduced; and finally, how these solar fuels can be put into practice. Most of the aspects treated in this section will be further discussed in later sections of the review. In particular, the connection between solar fuels and the importance in the study and development of Bismuth Vanadate *($BiVO_4$)* as a photocatalyst for water oxidation is explained.

According to the last “Intergovernmental Panel on Climate Change” IPCC Climate Change report (2007), “Global total annual anthropogenic GHG emissions, weighted by their 100-year “Global Warming Potential” GWPs, have grown by 70% between 1970 and 2004” and unequivocal evidences of increase in global average air and ocean temperatures, snow and ice melting and rising of global average sea level are serious threats for our future sustainable development if no substantial measures are adopted.(7)

On the other hand, several opinions claim that oil peaking has been or will be reached soon.(8, 9) Although forecast scenarios vary and a predicted shift towards coal or natural gas is also expected in terms of fossil fuel sources, a clear sign of alarm of energy security on the global scale is evident; in particular due to the high concentration of these energy supplies in relatively small areas and the increasing political and economic stability.(10) Moreover, the demand for energy around the world is still increasing every year and according to the World Energy Outlook 2011 by “International Energy Agency” IEA, even based on conservative assumptions the energy demand expected to increase be one-third from 2010 to 2035.(11)

As of today, renewable energy sources (*i.e.* biomass, geothermal, ocean, solar, wind, hydropower) contribute with about 89 EJ/yr (Energy Joules)(17% of total primary energy supply) (12), (13); however more than half of this amount is supplied by large hydropower plants and by utilization of traditional biomass, not being optimum from the sustainability point of view. However, according to different forecast scenarios analyzed by IPCC (2011), it is anticipated that renewable energies could contribute with savings between 218 and 561 (Giga Tonnes) Gt CO_2 compared to the predicted 1,530 Gt CO_2 of cumulative fossil and industrial CO_2 emissions during the period 2010-2050, which corresponds to a contribution of savings between 14 and 37%.(14) Finally, it is important to mention that among the available renewable energy technologies, currently modern biomass contributes with the largest share (9.0 EJ in 2009); nevertheless, it is expected that in the future solar and wind will play a more significant role.(13)

Of the many routes to hydrogen production there are currently available, steam reformation from hydrocarbons (mostly natural gas) using a nickel-based catalyst is the most commonly employed.(4, 15, 16) Although this process is widely used, it requires highly elevated temperatures of around 900 $°C$,(4, 17) which is not energy efficient. Nor does the production of the CO_2 and CO coincide with the ‘clean fuel’ objective.(18) Although the possibility of using solar concentrators to provide the thermal energy required for steam reformation has been investigated,(4) the process still requires a finite feedstock, e.g. CH_4. Other methods have been researched for hydrogen production. In the last decade, algae have been investigated as a possible source. Algae bioreactors produce hydrogen,(19) when not exposed to sulphur.(19), (20) However currently only 28% of the products are as hydrogen (others being glucose), and photosynthesis itself is only around 1% efficient with available photons,(21) maximum in plants being 6.7 %.(1) Use of the iodine-sulphur cycle, in which HI is formed and dissociates to form I_2 and H_2, has a number of problems including the production of H_2SO_4 and also the release of sulphur dioxide into the atmosphere. High temperatures are also required for this process.(4) Given the natural abundance of water, it is therefore an ideal source. Direct electrolysis of water can be used to split water into oxygen and hydrogen, however, a large amount of electrical energy is required (1‑10 $kA.m^{-2}$, 4‑4.9 $kWh.m^{-3}$),(6) and therefore more energy is required to generate hydrogen than would be supplied by its combustion. Thermal decomposition of water is particularly unfavourable as it requires extremely high temperatures of up to 3000 K, however, attempts have been made to

reduce this to ca. 800 °*C* using heterogeneous catalysts.(22) An alternative to this is the use of photocatalysts.

1.3.Photocatalysis

The earliest work that suggested photocatalytic behaviour can be dated back to the 1920s, when it was discovered that titania was partially reduced under illumination with sunlight in the presence of an organic compound such as glycerol, and turned from white to grey, blue or black.(23) This showed that these materials were responding to light and changing their electronic structure accordingly. Photocatalysts have been researched more and more in the last 40 years due to the prospective applications in sustainable hydrogen production,(24) first reported by Fujishima and Honda in 1972,(25) and in the degradation of organic matter.(23) There are now more than 130 reported photocatalytic materials and derivatives, although the most widely reported and researched is TiO_2.(26)

1.3.1. Principles

Photocatalysts are typically semiconductor materials and are dependent on the band structure of semiconductors.

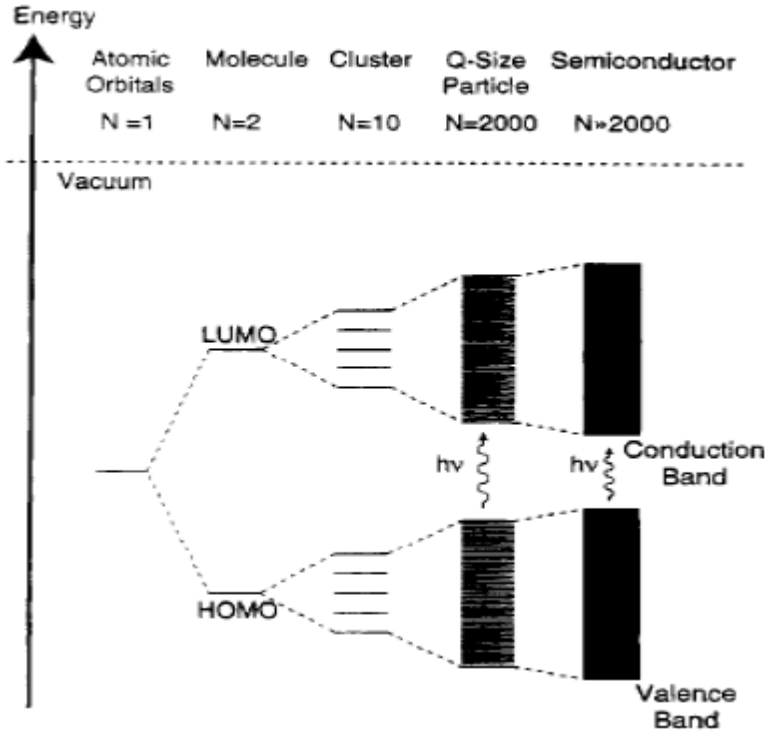

Figure:1.1:Schematic diagram showing the relationship of valence and conduction bands to molecularorbitals.(27)

The valence and conduction bands of a semiconductor are formed as molecular orbitals overlap as more molecules come together to form clusters, and then particles, shown in Fig-1.1.

The difference in energy between the conduction and valence bands is known as the band gap and an electron can be promoted from the valence band to the conduction band

following an optical transition if a photon of energy equal (or greater) than the band gap is absorbed. Photocatalytic reactions occur as when a photocatalytic material absorbs a photon, an electron is promoted from valence band to the conduction band. When this occurs, a positive electron vacancy (hole, h^+) is left in the valance band.

The electrons and holes can then migrate to the surface of the catalyst and undergo oxidation and reduction. For example, in the degradation of organic matter, and for hydrogen production, shown below:

$$H_2O + 2h^+ \rightarrow 2H^+ + \frac{1}{2}O_2$$

$$2H^+ + 2e^- \rightarrow H_2$$

This can be summarized as

$$2h\nu + 2H_2O \rightarrow H_2 + \frac{1}{2}O_2 \qquad \text{Eq}\rightarrow 1.1$$

1.3.2. Applications

As described above, photocatalysts can be used in hydrogen production by absorbing solar energy to split water into oxygen and hydrogen, but photocatalysts also have other applications. For example, antibacterial treatments(28)in the degradation of organic matter. Photocatalysts are also used in water purification, using other similar methods to degrade the organic species.(29, 30) Titanium dioxide has been reported to have been incorporated into operating theatre tiles in hospitals, as it can reduce absorbed bacteria.(31)These photocatalysts are also applied in the degradation of Volatile organic compounds that are evolved from the industries and from pollution. These volatile organic compounds get adsorbed on photocatalysts and then they are broken completely orincompletely into end products or intermediates respectively. Similarly, it has been used in self-cleaning glass and mirrors(23)e.g. the glass roof at St. Pancras Station, London. This is beneficial in glass because when it is cleared of organic matter, moisture droplets on the surface can spread out thereby preventing misting.(32)

1.4.Important aspects of a Semiconductor

1.4.1. Band positions

The suitability of a photocatalyst for solar hydrogen production depends on a number of factors. For example, the band positions of the photocatalyst must be in suitable positions, with respect to the electrochemical potentials for hydrogen and oxygen evolution, as demonstrated in fig. 1.2. In order for a reaction to occur with a semiconductor, the potential of the conduction band must be more negative that the hydrogen evolution potential, and similarly, the potential of the valence band must more positive than the redox couple for oxygen evolution. fig. 1.2 shows that titanium dioxide has bands that are energetically favourable with respect to the oxygen and hydrogen evolution potentials. However, in contrast, Fe_2O_3 is not ideal for hydrogen production if band energies alone are considered, as its conduction band occurs at a more positive potential than is required for hydrogen evolution, therefore an external bias is required to overcome this. Similarly, *GaAs* has a valence band at a more negative potential than that required for the oxygen evolution reaction.

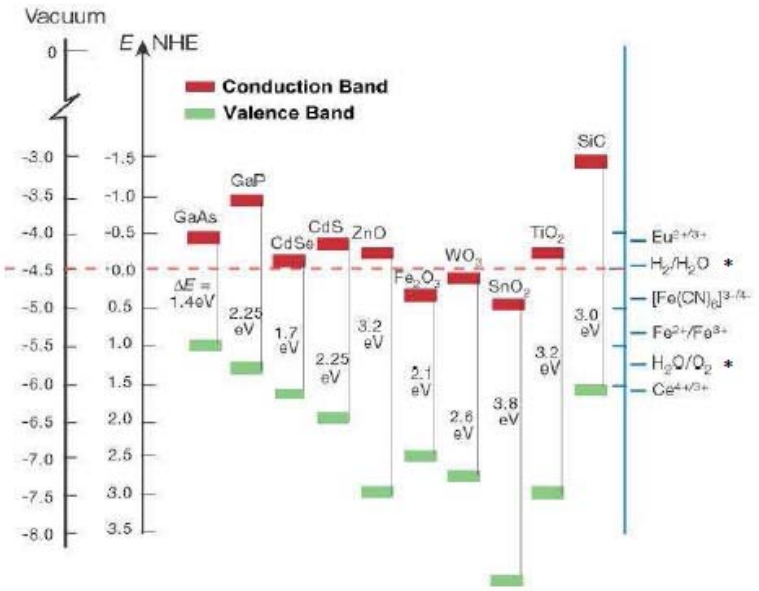

Figure: 1.2: Band positions of selected semiconductor photocatalysts. Redox potentials are given for comparison.(33)

1.4.2. Band gap energy

Although titanium dioxide is currently the most commonly used photocatalysts, one major hindrance is its comparatively large band gap, which as can be seen from fig. 1.2, is 3.2 *eV*.

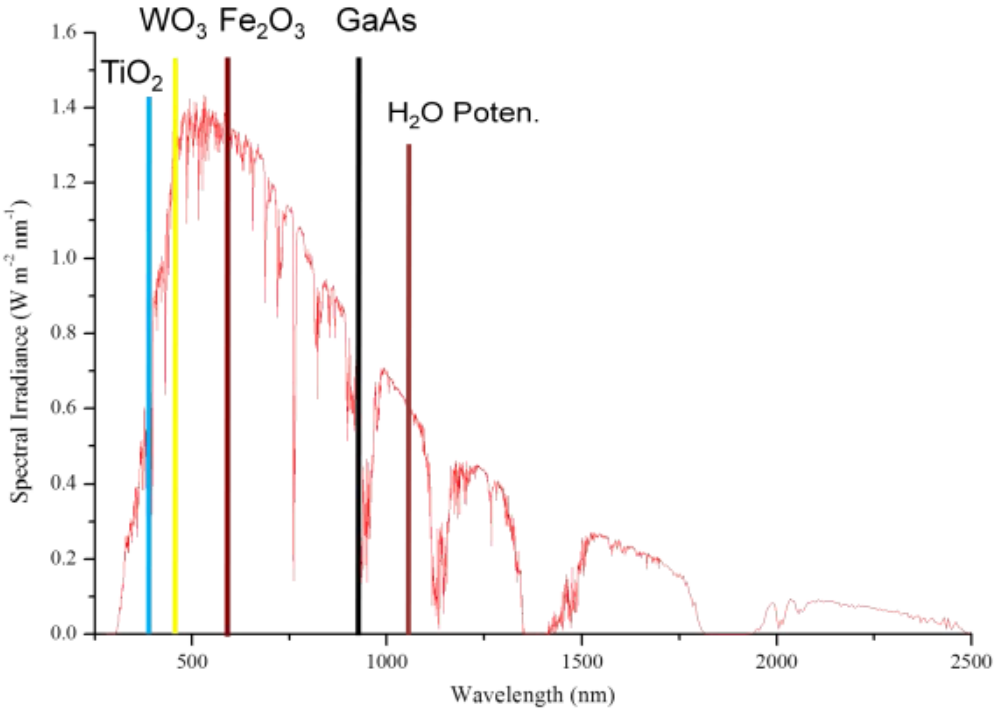

Figure: 1.3: Typical equatorial solar spectrum.(34) Also shown are the band gaps of some photocatalysts and the thermodynamic splitting potential of water.

The thermodynamic potential required to electrolyse water is 1.23 *eV*,(25) with reference to a normal hydrogen electrode. If the band gap of the photocatalyst is too large, it greatly limits the portion of photons in sunlight that can be converted into electrons and holes when the photocatalyst is irradiated. The band gap of 3.2 *eV* in TiO_2, corresponds to 387 *nm* in wavelength. This means that in order for water splitting to occur using TiO_2, only high energy photons of 387 *nm* and below are adequate. Unfortunately, this corresponds to only around 4% of the solar spectrum, and furthermore corresponds only to UV radiation as demonstrated below (fig. 1.3).

1.4.3. Degradation

As shown in fig 1.2, a number of semiconductor materials possess band gaps that are sufficiently low to be of interest. Furthermore, their valence and conduction bands suggest favorable thermodynamics for water splitting. Nevertheless, these materials, such as *CdS*, are not routinely used for water splitting, as they are unstable under the reaction conditions. There are a number of ways that these instabilities can present themselves, such as degradation, photo-degradation and delamination (on thin films). Degradation and photo-degradation can occur when the material is unstable in the electrolyte, and undergoes corrosion. This is caused by electrochemical processes involving charge transfer at the solid/liquid interface.(16) For stability in the aqueous environment, the free enthalpy of oxidation ($E_{p,d}$) of the material must be greater than the energy of the water oxidation reaction, and the free enthalpy of reduction of the material ($E_{n,d}$) must be lower than the energy of water reduction,(16)as shown in figure 1.4.

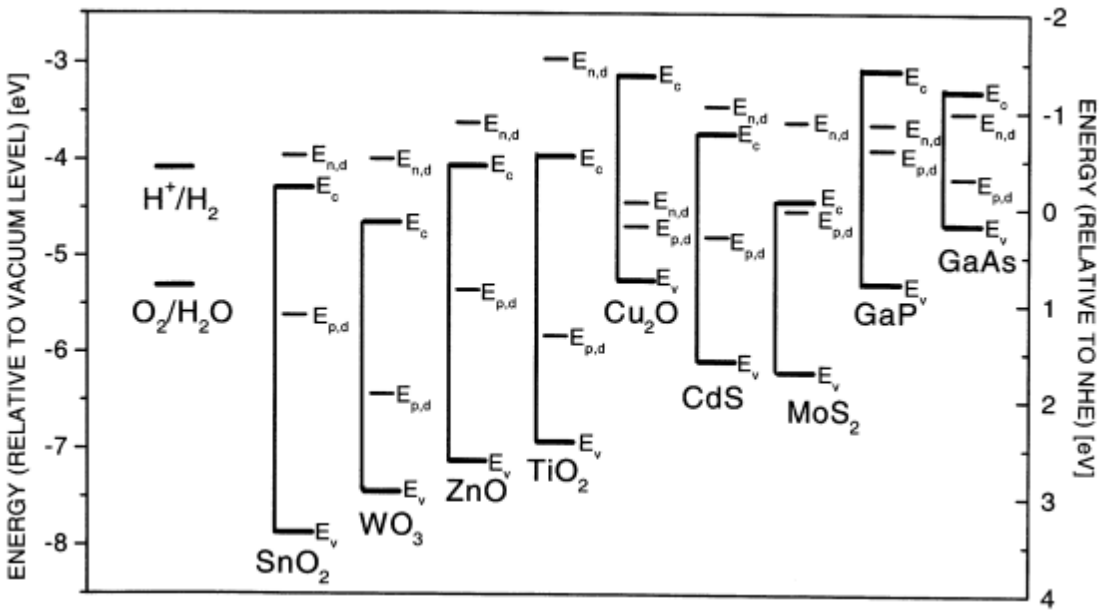

Figure: 1.4: Position of decomposition potentials with respect to band potions and water splitting potentials of stated materials.(16) Where E_v is the energy of the valence band, $E_c$is the free energy of the conduction band, $E_{p,d}$ is the enthalpy of oxidation of the material, and $E_{n,d}$is the free enthalpy of reduction of the material.

Photo-degradation consequently occurs in materials such as *CdS*, *ZnO*(35)and *GaAs* (shown in equation 1.2), while materials such as SnO_2, WO_3 and TiO_2 are much more resistant to corrosion.

$$GaAs + 6H_2O + 6h^+ \rightarrow Ga(OH)_3 + As(OH)_3 + 6H^+ \qquad Eq \rightarrow 1.2$$

Delamination occurs when the material comes off of the electrode substrate due to poor mechanical adhesion to a substrate. This is more an intrinsic property of the semiconductor and can be controlled, or at least mitigated, during the synthesis process.

1.4.4. Charge recombination

Not every photon that is incident on a semiconductor is converted to charge carriers, for example, as discussed previously, not all photons are of sufficient energy to generate electron-hole pairs. Another key issue is recombination. Recombination is the process in which the electron and hole recombine with each other due to the fact they are oppositely charged and so attract each other. This can happen in two ways, they can either recombine before reaching the catalyst surface (volume or bulk recombination), or they recombine at the surface before they can cross the interface into the surrounding medium (surface recombination), due to the fact that surface reactions are not instantaneous. This is shown in fig. 1.5.

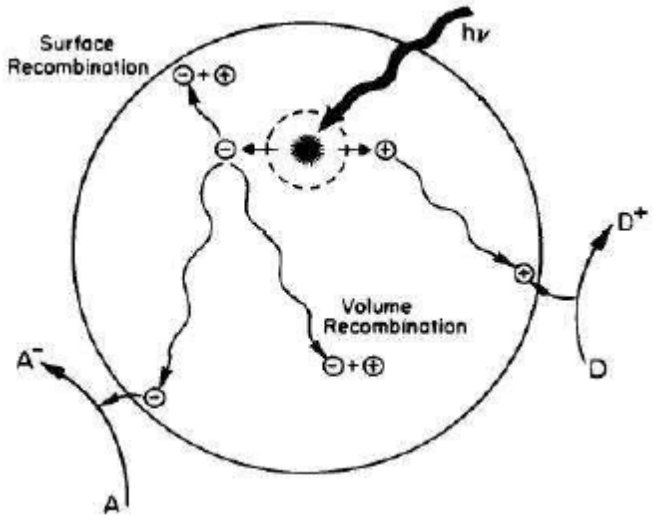

Figure. 1.6: Different recombination processes and surface reactions.(36)

Incident-photon-to-current efficiency (IPCE) is a method of determining the currentproducing efficiency of the catalyst. It indicates how many electrons per photon adsorbed, generate current.

There are a number of methods to limit the effect of recombination. For example, a decrease in particle size reduces the distance in which the generated charges need to migrate to reach the surface of the catalyst to react. Although this greatly reduces the likelihood of volume recombination, it does not reduce surface recombination. One way to do this is to add additional catalysts to the surface, which increases the rate of surface reactions, so the charges can react before they can recombine.

1.4.5. Physical Nature of a catalyst

Once the photophysical and chemical properties of a photocatalyst material have been considered, it remains to decide the physical form the photocatalyst might be employed, for example photolysis of water. There are two principal ways of using a photocatalyst: one is in suspensions and slurries, the other is with a catalyst immobilised on a surface and the choice will influence how easy it is to recover catalyst material, the efficiency of its use and how to overcome any problems associated with band positions. With slurries and suspensions, the dispersed catalyst would have a large surface area in direct contact with the reaction medium, however it can be difficult and time consuming to separate. One difficulty arises as when the catalyst is in a suspension: uniform illumination throughout the suspension is difficult, particularly at high catalyst loadings, which would also limit the efficiency of the catalyst as much of the light may be absorbed by the first few micrometers of the reaction suspension. The band positions of the catalyst with respect to the redox potentials involved would also have to be taken into account in order for the reaction to occur. For example, sacrificial agents would be required to allow WO_3 to be used to split water. Without these, electrons would be promoted to the conduction band but would not be able to transfer into the reaction medium due to the unfavourable position of the hydrogen evolution potential.

Immobilised catalysts, such as thin films on an electrode, are easier to separate from a reaction mixture as they are directly attached to a solid electrode, more stable and can be easily moved into a position where photo-illumination is possible. Another advantage of using electrodes is that it increases the choice semiconductor used, limitations relating to unfavourable band energetics can be overcome by applying a bias. For example, polarisation in an electrolyte causes a change on the surface potential of the semiconductor, resulting in band bending.(16)However, drawbacks of electrodes are that they are less efficient due to less surface area, as particle-particle contacts in the film mean that less of the catalyst material is in intimate contact with the surrounding solution. Immobilised catalysts also exist in materials such self-cleaning glass and mirrors also, by being incorporated into their surface. These functions do not require the removal of the material, but do require that band positions are favorable.

1.5. $BiVO_4$ as photocatalyst

Various attempts to enhance the capabilities of water-splitting photocatalysts have been examined recently. The absorption of photons in the visible-light spectrum range is of particular interest in order to reach a meaningful efficiency for competitive prospective devices. Some photo-active catalysts have been found to be capable of accomplishing water oxidation reactions utilizing UV light, e.g. TiO_2 or $NaTaO_3$ with band gaps above 3 eV.(37)

Recently, Bismuth Vanadate ($BiVO_4$) has gained increasing attention for its use as a photoanode capable of promoting the oxidation of water to O_2 in the half reaction of a complete PEC cell which would include the reduction of water to H_2 or CO_2 to other biofuels/bioproducts. For example, $BiVO_4$ would be suitable for a Z-scheme photoanode.

Some of the commonly quoted advantages found in $BiVO_4$ are: i) low band gap of about 2.4 eV (for the monoclinic scheelite), corresponding roughly to a 520 nm wavelength, which shows a good visible-photon absorbance performance(38, 39) ii) Valance Band (VB) position is negative enough (ca. 2.4 V vs RHE) with respect to water oxidation $H_2O + h^+ \rightarrow O_2$ while Conduction Band (CB) is around 0 V vs RHE, implying a thermodynamic level close to H_2;(38, 40, 41) iii) effective masses of electrons and holes have been estimated to be lower

than similar semiconductors (e.g. In_2O_3 or TiO_2) which would result, in principle, in an improved separation and extraction process of electron-hole pairs;(38, 40, 41) finally, iv) $BiVO_4$ is also appropriate as photoanode material as being composed of inexpensive materials elements and its non-toxic properties.(38, 40)

1.5.1. Crystal Structure

$BiVO_4$ as synthetized in laboratory can crystallize into three different structures, namely: i) tetragonal-scheelite (*t-s*); ii) monoclinic scheelite (*m-s*); and iii) zircon-type (*z-t*) $BiVO_4$ (fig. 1.7). Of these three structures, monoclinic form has found to be the most photocatalytically active. Therefore, more attention is paid to this structure. This monoclinic phase is constituted of V surrounded by *4 O* atoms, forming a tetrahedron, and *Bi* surrounded by *8 O* atoms forming a dodecahedron, as shown in Figure: a. The crystal lattice exhibits a layered structure, with alternating *-Bi-V-* configuration on the *a-* and *c*-axis (Figure: c) and *-Bi-V-V-Bi-* on the *b*-axis (fig. 1.8 d).(38, 40, 41)

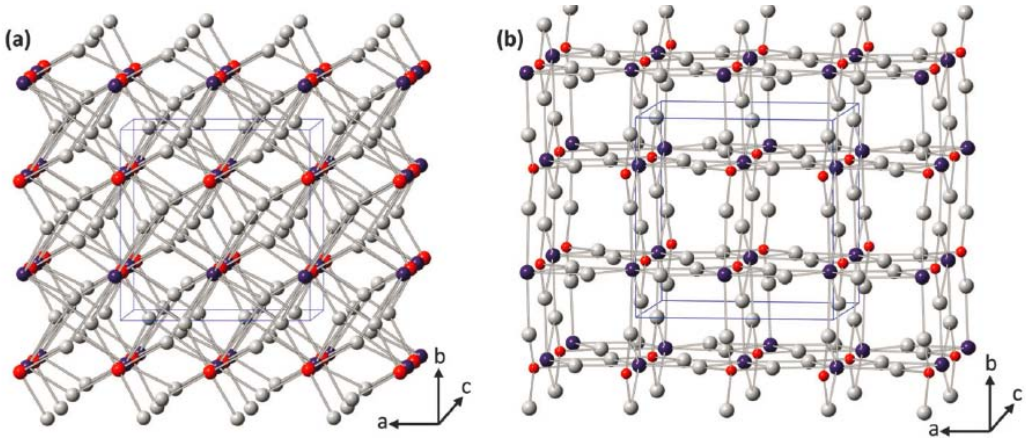

Figure:1.7: Crystal structure model of a) scheelite and b) zircon-type $BiVO_4$ (38)

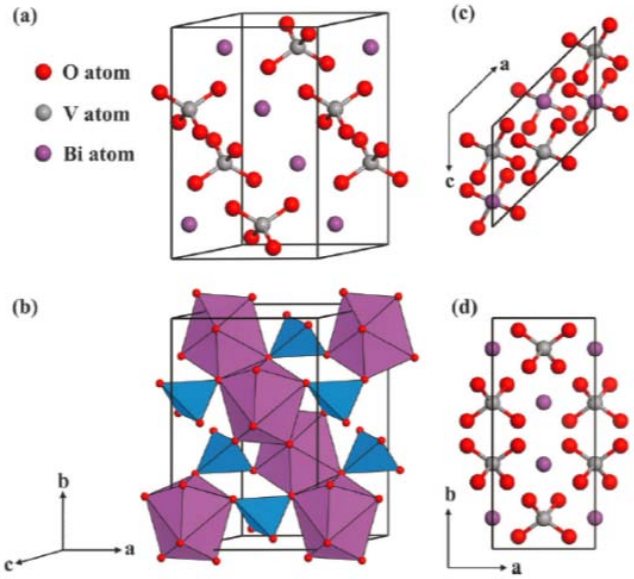

Figure:1.8: a) Monoclinic clinobisvanite $BiVO_4$; b) polyhedron representation; c) top view and d) side view (40)

As mentioned before, monoclinic crystal form exhibits the best photocatalytic properties, as initially demonstrated experimentally by.(39) An explanation for this is that in the monoclinic scheelite, the local environments of *V* and *Bi* ions are more significantly distorted,(40) as reflected in the unbalanced *Bi-O* and *V-O* bond lengths (Table.1.1 and in contrast to the tetragonal and zircon-type formswhich are more symmetric. It is described that this structural distortion can enhance the lone-pair impact of the *Bi 6s* states, while the VO_4 tetrahedron distortion induces an internal electric field, both beneficial for the electron-hole separation process and giving its anisotropic optical properties.(40)

Table: 1.1 Crystallographic parameters of monoclinic $BiVO_4$ by model and experimental results and comparison of bond lengths with tetragonal and zircon-type phases

Estimation method	a/Å	b/Å	c/Å	β (°)	Bi-O/Å	V-O/Å
Monoclinic phase						
DFT calculationa	7.224	11.522	5.108	135.003	2.416 x 2 2.418 x 2 2.446 x 2 2.449 x 2	1.730 x2 1.731 x 2
Powder neutron diffraction	7.247	11.697	5.090	134.226	2.354 x 2 2.372 x 2 2.516 x 2 2.628 x 2	1.69 x 2 1.77 x 2
Tetragonal phase						
Powder neutron diffraction					2.453 x 4 2.499 x 4	1.720 x 4
Zircon-type phase						
Powder neutron diffraction					2.414 x 4 2.549 x 4	1.703 x 4

a Ref. (40)
b Ref. (42)

Temperature plays an important role in the phase transition between the three characteristic $BiVO_4$ crystal forms (i.e. monoclinic, zircon-type and tetragonal scheelite. An irreversible transition from zircon-type to monoclinic occurs at around 400-500 ^oC, while phase transition between monoclinic and tetragonal occurs reversibly at about 265 ^oC.(39) In addition, the evolution from tetragonal to monoclinic phase was reported at room temperature after 48*h* of stirring of *Bi:V 1:1* precursors in aqueous solution.(39) This evolved monoclinic form yielded the largest O_2 evolution (478 $\mu mol.h^{-1}$) after further calcination at 400 °*C*, whereas for a tetragonal form calcined at 500 °*C* (where thermal transition happens) the O_2 evolution was one order of magnitude lower. Finally, although in general calcination increased the photocatalytic activity of the powders, when performed above 600 °*C* the O_2 production was significantly reduced most likely due to appearance of crystal defects.(39)

1.5.2. Electronic structure

In the field of metal-oxide photocatalysts different attempts have been performed in order to improve electric and optical properties that allow absorption of visible-light photons. The introduction of Bi^{3+}cations in $BiVO_4$ is such an example of the denominated "valance band-controlled metal oxides" strategy in which the *Bi 6s2* states contribute to rise the very positive VB of O2P oxides, promoting the desired band gap reduction.(37, 38, 41, 43-p4)

The electronic structure of $BiVO_4$ has been studied through DFT calculations by different authors.(40, 41) Walsh, et al. (2009) found that hybridization between *Bi 6s* and *O 2p* states at the top of the VB is indeed responsible for the smaller band gap of monoclinic $BiVO_4$, while the CB is composed mainly of *V 3d* states with *O 2p* and *Bi 6p* contributions.(41) In a recent work, Zhao et al. (2011) performed a more detailed analysis including all the *k*-points to describe $BiVO_4$ band structure. They found a minimum indirect band gap of 2.174 *eV*, while other direct band gaps exist at slightly larger energies.(40) Fig. 1.8 depicts the total and local ion-projected electronic density of states of monoclinic $BiVO_4$. Here it can be seen that the top of the VB is mainly composed by two non-bonding states, *Bi 6s* and *O 2pπ* states, respectively. This is a particular characteristic of *m-*$BiVO_4$, since as experimental results proved, in the tetragonal phase only UV absorption due to *V-O* transition is observed

Changes in the mass of electrons (e^-) in the conduction band and mass of protons (h^+) in the valence band which constitute to have effective mass under excited states, have significant influence on the charge mobility which in turn effect the charge separation in a semiconductor material. Zhao, et al (2011) also found that the effective mass of photogenerated electrons on the bottom of CB is ca. $0.9\ m_0$, while for holes on the top of VB is ca. $0.7\ m_0$ (electron rest mass). This highly reduced effective masses of photogenerated carriers is supposed to enhance the separation and transport of electron-hole pairs within a given life-time, therefore improving the overall photocatalytic activity.(40) Walsh, et al(2009) estimated effective masses on the order of $0.3\ m_0$ for both holes and electrons.(41)

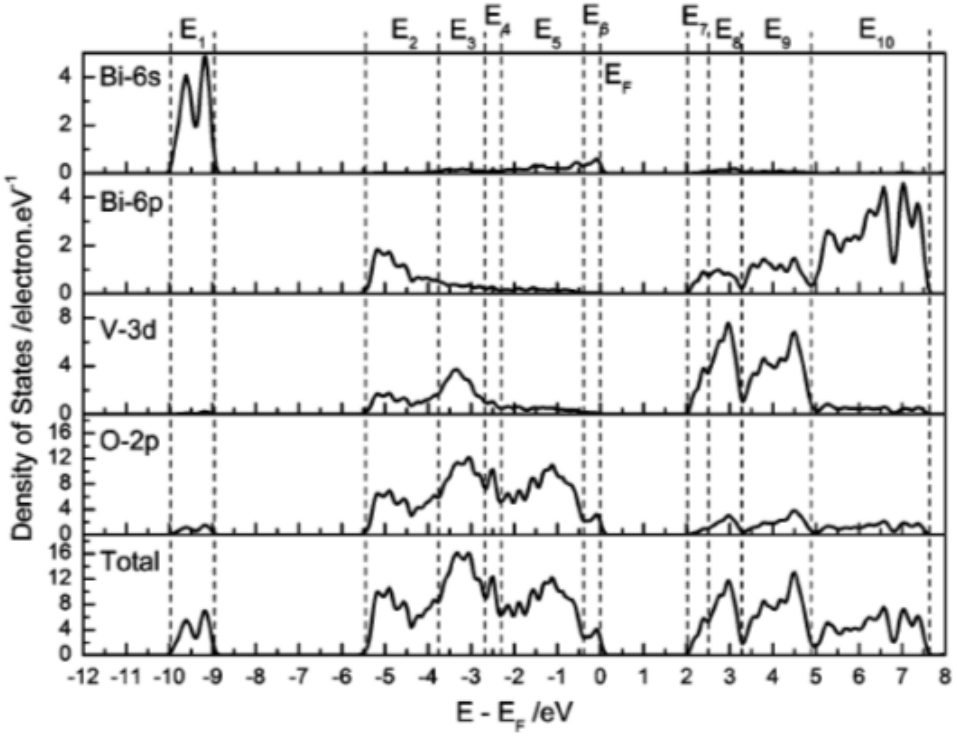

Figure: 1.8: Total and local partial density of states of monoclinic $BiVO_4$ (40)

1.5.3. Optical Properties

As mentioned earlier, monoclinic $BiVO_4$ has been regarded as one of the most active visible-light photocatalysts for water oxidation, therefore being of great interest in the field of solar fuels. According to the electronic properties studied above the hybridization of the *Bi 6s* and *O 2p* orbitals achieved by introducing the *Bi* cation into the metal-oxide structure results in rising of the top of VB reducing the band gap of monoclinic $BiVO_4$. In early works by Kudo, et al (1999) *s-m* $BiVO_4$ powders prepared at room temperature by mixing of parental reactants followed by calcination were investigated. They obtained band gap of 2.4 *eV*, as compared to 2.9 *eV* found for tetragonal phase observed in the same study.(39) In fig.1.10 the effect of calcination temperature on $BiVO_4$ samples is shown; a remarkable increase of absorption in the visible-spectrum range is observed, corresponding to a decrease in the band gap value.(39)

For semiconductor catalysts, the Kubelka-Munk function is a well-known estimation method to determine their optical band gap. This Kubleka-Munk function *(F(R))* utilizes the reflectance *(R)* value of a sample in order to approximate the optical absorbance of a semiconductor. After this manipulation a Tauc Plot can be constructed with $(F(R) \cdot h\nu))^n$ vs *hv*; where *h* stands for Planck's constant and *v* for frequency of vibration. For a direct band semiconductor, the Tauc region, just above the optical absorbance edge, shows a linear trend with $n = ½$, as it has been reported for *s-m*$BiVO_4$.(44), (45), (46) The extrapolation of this line to the *hv* axis gives the semiconductor band gap, as seen in fig. 1.9 for a $BiVO_4$ thin film sample at different annealing temperatures. The band gap value gradually decreases as annealing temperature increases from 2.53 to 2.47 *eV*.(44)

Using DFT calculations, Zhao, et al. (2011) found that in the monoclinic phase of $BiVO_4$ there is a significant optical anisotropy near the absorption edges, resulting from the above mentioned special electronic structure and distorted crystal structure. This optical anisotropy is demonstrated by the differing absorption coefficient found along different spatial axis, which for *a* and*c* exhibit a peak at 440 *nm*, whereas for *b* is located at about 330 *nm*. Moreover, along *a*- and *c*- axis the same bonds are present, while along *b*-axis the different dipoles formed forbid the electron transition from top VB to bottom CB. This is one of the reasons why the morphology-control strategy to expose larger areas of the (100) and (001) crystal facets is one of the common approaches undertaken to increase the photocatalytic activity of $BiVO_4$.(7)

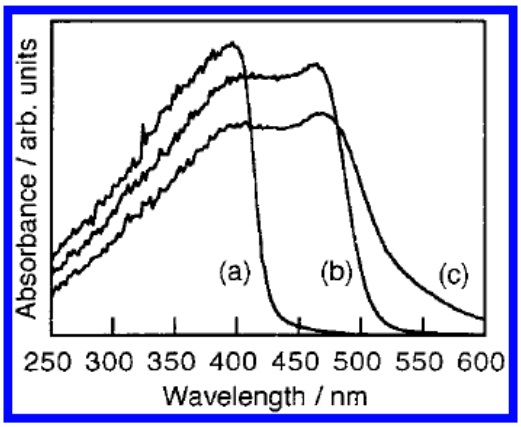

Figure: 1.9 Diffuse reflectance spectra of $BiVO_4$ originally tetragonal and calcined at different temperatures: a) 330, b) 770 and c) 1170 *K*(39)

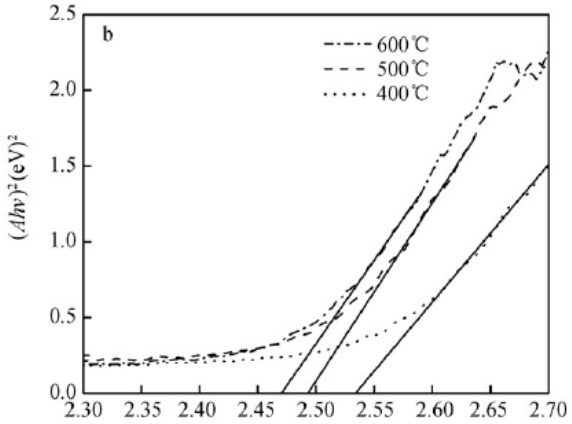

Figure: 1.10 Calculated band gap extrapolation according to UV-VIS absorption spectra for $BiVO_4$ thin film prepared by dip coating technique (43)

Recently, Xi & Ye (2010) synthetized *m*-$BiVO_4$nanoplates with exposed {001} facets, as confirmed from FESEM image and (004) diffraction peak increase in XRD pattern, yielding an improved photocatalytic O_2 evolution.(47) Although they do not give insights of the reasons behind this increase, they point out that a higher hydrophilic capacity and larger surface energy of this plane could be related to the increase in activity. Moreover, they discard the increase of surface area as a direct reason for the higher activity, since needles synthetized under similar conditions and with higher surface area resulted in worse activities as compared to the nanoplates.

1.6. Objectives and structure of thesis

The objectives of the present work are given as prescribed in the Fig. 1.11The whole figure describes the strategy to be followed to complete two projects in our group. Out of the complete description in the fig. my thesis includes first two processes, comprising of morphology control of the $BiVO_4$, doping with Molybdenum and Tungsten and thin film fabrication using dip coating as well as spin coating procedures.

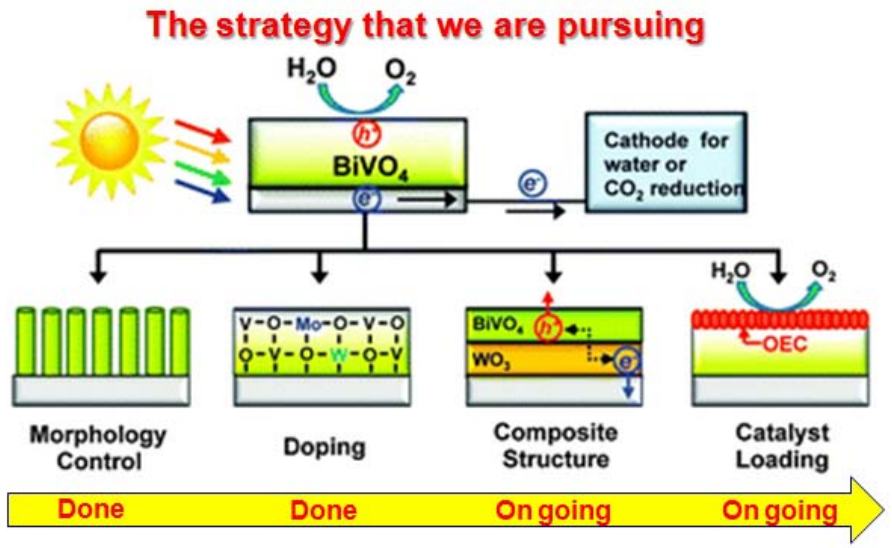

Figure: 1.11 The detailed description of the chapters is stated below with a small overview.

Heterogeneously dispersed semiconductor surfaces provide both a fixed environment to influence the chemical reactivity of a wide range of adsorbates and a means to initiate light-induced redox reactivity in these weakly associated molecules. Upon photoexcitation of several Semiconductors non-homogeneously suspended in either aqueous or nonaqueous solutions or in gaseous mixtures, simultaneous oxidation and reduction reactions occur. This conversion often accomplishes either a specific, selective oxidation or a complete oxidative degradation of an organic substrate present. Molecular oxygen is often assumed to serve as the oxidizing agent although details about the mode of its involvement have not been unambiguously demonstrated except in a few gas/solid reactions. The incident light that initiates this sequence is in a wavelength region (the visible or low-energy range of the ultraviolet regions of the spectrum) absorbed by the semiconductor rather than by the substrate of interest. These reactions therefore involve photosensitization, i.e., an indirect photoactivation of the heterogeneously dispersed particulate absorber rather than the direct formation of an excited state of the substrate. Furthermore, the suspended semiconductor particle that acts asthe photocatalyst is often stable to the photolysis conditions (particularly when a metal oxide is employed) and a large number of oxidative conversions per active site on the catalyst can be attained without significant degradation of the semiconductor's redox catalytic capacity. For these reasons, such semiconductor-mediated redox reactions are often grouped under the rubric of heterogeneous photocatalysis.

The Present PhD Thesis involves one or more articles that are either published, submitted or on their way of manuscript preparation. These all chapters are placed in context to the understandings and advancements involved in the PhD period. The whole thesis involves insights about synthesis and characteristics of $BiVO_4$ in the form of powder as well as thin films. It also describes their influence in the efficiency of the material.

In chapter 3 the reader had introduced the important parameters of the material in powder form which are important for $BiVO_4$ when considered about the water oxidation. These parameters were considered to be the primary aspects of the material $BiVO_4$ considering water oxidation. This chapter uses a simple method of synthesis conditions with cost effective materials. Further it has been concluded that the band gap, crystalline size and *V-O* bond

length are some of the primary parameters that were considered to be important with respect to water oxidation. The insights from anneling temperature with crystalline size were observed and it over all influence over the activity is deduced.

Chapter 4 and 5 deals with the secondary parameter of $BiVO_4$, which had also some influence over the activity. This is evaluated by altering the synthesis conditions in terms of the initial precursor solution. Here the *pH* of the precursor solution is varied keeping the rest of the conditions uniform. It had been observed that the *pH* had an influence over the crystalline faces of the $BiVO_4$. In this chapter the focus was towards the two peaks of XRD which corresponds to the crystal facets labeled as (011) and (040) of the system of $BiVO_4$. The *pH* of the system has an influence on (040) peak of XRD. The*pH* of the precursor solution increases, the (040) peak of the crystal system increases. In chapter 4it has been discussed the influence of the (040) with the water oxidation activity of the $BiVO_4$. Here it has been showed to have a positive influence of (040) over the water oxidation activity of the system. In chapter 5, the same system of $BiVO_4$influence over the volatile organic compound decomposition was evaluated. The details about the degradation of ethylene was explained and it is in favor to the (040) crystal plane.

Chapter 6 discusses about the doping properties of the $BiVO_4$. Here in we verified the importance of the doping characteristics of the $BiVO_4$ with enhanced (040) crystal planes. The doping of the system is carried with Tungsten and Molybdenum.In this chapter it has been elucidated the physical properties and the optical properties of $BiVO_4$undoped and doped with $W^{6+1}wt$,$W^{6+5}wt$, $Mo^{6+1}wt$ and $Mo^{6+5}wt$ into the V^{5+} sites presents in the $BiVO_4$ lattice. Then a photocatalytic O_2 evolution study was performed and correlated with the physical and optical changes. In order to have a more practical system, the fabrication of a $BiVO_4$ photoanode is a practical alternative for the design and construction of the photocatalytic devices. The second part of this work in this chapter refers to the study of $BiVO_4$ electrodes, using the $BiVO_4$ powder prepared by hydrothermal synthesis (HTS), conventional slurry (CS) method for its fabrication and a method called doctor blade for the final deposition of the slurry in the electrode.

In chapter 7 the description of in-situ synthesis of electrode system is studied on a FTO electrode.The deposition of Bismuth Vanadate thin films onto FTO glass electrodes using a simple dip coating procedure is reported herein. The importance of the thickness of the films is highlighted. Details regarding the influence of the thickness on the photo-electrochemical performance for the water splitting reaction have been explained through electrochemical impedance spectroscopy. It has been found that the thickness of the electrode should be around (160 *nm*) in order to obtain a maximum photo-current density of about 0.57 $mA.cm^{-2}$at 1.23 *V* vs. RHE under sunlight illumination.

As of now in this thesis work I improved the current produced without the process of doping to a considerably efficient value which can be improved by further modification and which is in the progress. The present system can be helpful to exploit the sunlight and produce a current of 0.6 $mA.cm^{-2}$in 0.1*M* Na_2SO_4 solution with an applied bias of 1.23 *V* which is considered as an acceptable potential that can be applied for the process of hydrogen production on the counter electrode in a photo-electrochemical cell.

1.7.References

1. N. Armaroli and V. Balzani, The Future of Energy Supply: Challenges and Opportunities, Angew. Chem. Int. Ed., Volume 46, Issue 1-2, pages 52–66, December 18, 2006

2. R. van de Krol, Y. Q. Liang and J. Schoonman, Solar hydrogen production with nanostructured metal oxides, J. Mater. Chem., 2008, 18, 2311-2320

3. N. S. Lewis and D. G. Nocera, Powering the planet: chemical challenges in solar energy utilization., Proc. Natl. Acad. Sci., U. S. A., 2006, 103, 15729-15735

4. D. A. J. Rand, R. M. Dell and R. Dell, Hydrogen Energy: Challenges and prospects, Royal Society of Chemistry, Cambridge, UK, 2008.

5. N. Parmentier and J. C. Nenot, Radiation damage aspects of the Chernobyl accident, Atmospheric Environment, 1967, 23, 4, 771-775.

6. M. Pagliaro, A. G. Konstandopoulos, R. Ciriminna and G. Palmisano, Solar hydrogen: fuel of the near future, Energy Environ. Sci., 2010, 3, 3, 279-287

7. IPCC, Climate Change 2007: Synthesis Report. Geneva, Switzerland, 2007.

8. D. L. Greene, J. L. Hopson, and J. Li, “Have we run out of oil yet? Oil peaking analysis from an optimist’s perspective,” Energy Policy, vol. 34, no. 5, pp. 515–531, Mar. 2006.

9. Q. Y. Meng and R. W. Bentley, “Global oil peaking: Responding to the case for ‘abundant supplies of oil’,” Energy, vol. 33, no. 8, pp. 1179–1184, Aug. 2008.

10. S. C. Bhattacharyya, Energy economics: concepts, issues, markets and governance. Springer London Dordrecht Heidelberg New York: Springer-Verlag London Limited, 2011.

11. OECD/IEA, World Energy Outlook 2011. Cedex, France: IEA Publications, 2011.

12. H. Waisman, J. Rozenberg, O. Sassi, and J.-C. Hourcade, “Peak Oil profiles through the lens of a general equilibrium assessment,” Energy Policy, 2012, 48, 744-753.

13. W. C. Turkenburg, D. J. Arent, R. Bertani, A. Faaij, M. Hand, W. Krewitt, E. D. Larson, J. Lund, M. Mehos, T. Merrigan, C. Mitchell, J. R. Moreira, W. Sinke, V. Sonntag-O’Brien, B. Thresher, W. van Sark, E. Usher, and E. Usher, “Chapter 11 - Renewable Energy,” in Global Energy Assessment - Toward a Sustainable Future, Cambridge University Press, Cambridge, UK and New York, NY, USA and the International Institute for Applied Systems Analysis, Laxenburg, Austria, 2012, 761–900.

14. M. Fischedick, R. Schaeffer, A. Adedoyin, M. Akai, T. Bruckner, L. Clarke, V. Krey, I. Savolainen, S. Teske, D. Ürge-Vorsatz, and R. Wright, “Mitigation Potential and Costs,” in IPCC Special Report on Renewable Energy Sources and Climate change Mitigation, O. Edenhofer, R. Pichs-Madruga, Y. Sokona, K. Seyboth, P. Matschoss, S. Kadner, T. Zwickel, P. Eickemeier, G. Hansen, S. Schlömer, and C. von Stechow, Eds. Cambridge, United Kingdom and New York, NY, USA: Cambridge University Press, 2011.

15. Y. Z. Chen, H. Y. Xu, Y. Z. Wang and G. X. Xiong, Hydrogen production from the steam reforming of liquid hydrocarbons in membrane reactor, Catal. Today, 2006, 118, 136-143.

16. T. Bak, J. Nowotny, M. Rekas and C. C. Sorrell, Photo-electrochemical hydrogen generation from water using solar energy. Materials-related aspects, Int. J. Hydrogen Energy, 2002, 27, 991-1022.

17. P. Simpson and A. E. Lutz, Exergy analysis of hydrogen production via steam methane reforming, Int. J. Hydrogen Energy, 2007, 32, 4811-4820.

18. European Commission, Concentrating solar power: From research to implementation, 2007, 1-39.

19. Melis, M. Seibert and M. L. Ghirardi, Hydrogen fuel production by transgenic microalgae, Adv. Exp. Med. Biol., 2007, 616, 110-121.

20. S. K. Deb, Opportunities and challenges in science and technology of WO3 for electrochromic and related applications, Sol. Energ. Mat. Sol. Cells, 2008, 92, 245-258.

21. M. S. Dresselhaus and I. L. Thomas, Alternative energy technologies, Nature, 2001, 414, 332-337.

22. B. Sorensen, Hydrogen and fuel cells, Academic Press, Oxford, UK, 2005.

23. Fujishima, X. T. Zhang and D. A. Tryk, TiO2 photocatalysis and related surface phenomena, Surf. Sci. Rep., 2008, 63, 515-582.

24. D. Alexander, P. J. Kulesza, L. Rutkowska, R. Solarska and J. Augustynski, Metal oxide photoanodes for solar hydrogen production, J. Mater. Chem., 2008, 18, 2298-2303.

25. Fujishima and K. Honda, Electrochemical Photolysis of Water at a Semiconductor Electrode, Nature, 1972, 238, 37-38.

26. F. E. Osterloh, Inorganic materials as catalysts for photochemical splitting of water, Chem. Mater., 2008, 20, 35-54.

27. M. R. Hoffmann, S. T. Martin, W. Y. Choi and D. W. Bahnemann, Environmental Applications of Semiconductor Photocatalysis, Chem. Rev., 1995, 95, 69-96.

28. C. Trapalis, P. Keivanidis, G. Kordas, M. Zaharescu, M. Crisan, A. Szatvanyi and M. Gartner, TiO2(Fe3+) nanostructured thin films with antibacterial properties, 12th International Conference on Thin Films, Elsevier Science, Bratislava, Slovakia, 2002.

29. R. Molinari, L. Palmisano, E. Drioli and M. Schiavello, Studies on various reactor configurations for coupling photocatalysis and membrane processes in water purification, J. Membrane Sci., 2002, 206, 399-415.

30. T. Arai, Y. Konishi, Y. Iwasaki, H. Sugihara and K. Sayama, High-Throughput Screening Using Porous Photoelectrode for the Development of Visible-Light-Responsive Semiconductors, J. Comb. Chem., 2007, 9, 574-581.

31. Fujishima and X. T. Zhang, Titanium dioxide photocatalysis: present situation and future approaches, C. R. Chim., 2006, 9, 750-760.

32. T. L. Thompson and J. T. Yates, Surface science studies of the photoactivation of TiO2 new photochemical processes, Chem. Rev., 2006, 106, 4428-4453.

33. M. Gratzel, Review article Photoelectrochemical cells, Nature, 2001, 414, 338-344.

34. NREL, Reference Solar Spectral Irradiance: Air Mass 1.5,

35. Chatterjee and S. Dasgupta, Visible light induced photocatalytic degradation of organic pollutants, J. Photochem. Photobiol. C-Photochem. Rev., 2005, 6, 186-205.

36. L. Linsebigler, G. Q. Lu and J. T. Yates, Photocatalysis on TiOn Surfaces: Principles, Mechanisms, and Selected Results, Chem. Rev., 1995, 95, 735- 758.

37. K. Maeda, "Photocatalytic water splitting using semiconductor particles: History and recent developments," J. Photochem. Photobiol. C-Photochem. Rev., 2011, 12, 4, 237-268.

38. Y. Park, K. J. McDonald, and K.-S. Choi, "Progress in bismuth vanadate photoanodes for use in solar water oxidation," Chem. Soc. Rev., 2013, 42, 6, 2321-2337.

39. Kudo, K. Omori, and H. Kato, "A novel aqueous process for preparation of crystal form-controlled and highly crystalline BiVO4 powder from layered vanadates at room temperature and its photocatalytic and photophysical properties," J. Am. Chem. Soc.,1999, 121, 49, 11459-11467.

40. Z. Zhao, Z. Li, and Z. Zou, "Electronic structure and optical properties of monoclinic clinobisvanite BiVO4," Phys. Chem. Chem. Phys., vol. 13, no. 10, pp. 4746–4753, 2011.

41. Walsh, Y. Yan, M. N. Huda, M. M. Al-Jassim, and S.-H. Wei, "Band Edge Electronic Structure of BiVO4: Elucidating the Role of the Bi s and V d Orbitals," Chem. Mater., 2009, 21, 3, 547-551.

42. Sleight, H. Chen, A. Ferretti, and D. Cox, "Crystal-growth and structure of BIVO4," Mater. Res. Bull., 1979, 14, 12, 1571-1581.

43. J. Yu and A. Kudo, "Effects of structural variation on the photocatalytic performance of hydrothermally synthesized BiVO4," Adv. Funct. Mater., 2006, 16, 16, 2163-2169.

44. Zhou, J. Qu, X. Zhao, and H. Liu, "Fabrication and photoelectrocatalytic properties of nanocrystalline monoclinic BiVO4 thin-film electrode," J. Environ. Sci.-China, 2011, 23, 1, 151-159.

45. Shimadzu, "Measurement of Band Gap in compound Semiconductors - Band Gap Determination from Diffuse Reflectance Spectra," Shimadzu Corporation, No. A428.

46. "UV-vis Spectrometry," ASCG. [Online]. Available: http://www.msm.cam.ac.uk/ascg/characterisation/uvvis.php. [Accessed: 27-Feb-2013].

47. G. Xi and J. Ye, "Synthesis of bismuth vanadate nanoplates with exposed {001} facets and enhanced visible-light photocatalytic properties," Chem. Commun., 2010, 46, 11, 1893-1895.

2. Chapter 2. Characterization Techniques

2.1. UV-Visible Spectroscopy

Diffuse reflectance spectroscopy is a technique to estimate the absorption properties of materials. For semiconductors, the absorption coefficient and band gap values can be estimated using DFR spectroscopy measurements. UV-Vis diffuse reflectance spectra were obtained on a UV-Vis Varian's Cary 5000 spectrophotometer using a quartz cell suitable for powders measurements. The band gap energies(*Eg*) for the different samples were calculated by plotting the values of $(ahv)^n$ vs the photon energy (*hv*), where a is the absorption coefficient, *h* is the Plank constant and *v* the frequency of vibration. The value of *n* in the relation depends on the type of transitions involved, $n = 2$ for a direct transition and $n = ½$ for an indirect transition.(1) The relation between the absorption coefficient and the reflectance of the sample is calculated from the Kubelka – Munk function.(2)

$$F(R) = \frac{(1-R)^n}{2R} = \frac{\alpha}{S} \qquad Eq \rightarrow 2.1$$

Where *F(R)* for the Kubelka-Munk function, *R* is the absolute reflectance, α for the absorption coefficient and *S* for the scattering coefficient. The band gap values were estimated from a plot of $[f(R) \_ hv]^n$ vs *hv*.

2.2. X-Ray Diffraction Analysis

X-Ray diffraction (XRD) is a technique for estimating the crystal structure of a sample. XRD can be used to estimate the crystal structure of both single crystals and powder samples. A typical diffraction pattern contains a plot of the measured intensity against the diffraction angle (Bragg angle). In the case of powder samples, XRD analysis can provide information on the purity of the powder sample, and also identify the crystal structure of an unknown material.(3)

X-ray diffraction (XRD) patterns were obtained using an X'Pert Phillips diffractometer equipped with an X-ray source of *Cu Kα* radiation ($\lambda = 0{:}15418nm$) at $40kV$ and $30mA$. The patterns were recorded in the range of 5-60° at a step size of 0.02°. Crystallite sizes and lattice strain parameters for $BiVO_4$ catalysts were estimated from the line broadening of (1 2 1) X-ray diffraction peaks by using the XPert HighScore Plus software. The average particle size, estimated from the XRD peaks using the Scherrer equation.(4)

$$D = \frac{K\lambda}{\beta \cos\theta} \qquad Eq \rightarrow 2.2$$

Where *k* is the shape factor (0.9), λ is the wavelength ($0.15418nm$), β is the peak width at half-maximum height (FWHM) in radians of a selected diffraction peak and θ is the diffraction angle.

2.3. Scanning Electron Microscopy

Electron microscopes were developed in the 1930s to overcome the limitations of optical microscopy and provide increased magnification and resolution, far superior to optical

systems. The first commercialized SEM was built by Cambridge Instruments. For detailed history of the SEM's development, see Goldstein.(5) SEM is a powerful tool for examining and interpreting microstructures of materials, and is widely used in the field of material science. The principle of SEM is based on the interaction of an incident electron beam and the solid specimen.(6) Electron bombardment can produce a wide variety of emissions from the specimen, including backscattered electrons, secondary electrons, Auger electrons, X-rays, visible photons and so on.

Secondary electron imaging and X-ray analysis were the primary functions used for SEM sample characterisation in this study.

The spatial resolution of the SEM is strongly dependent on diameter (spot size) of the electron probe beam at the specimen surface. In a SEM system, the diameter of the incident electron beam is demagnified using two or more electron lenses before it reaches the sample surface. At the same time, the effective diameter of the electron source is a key factor in determining the resolution of the SEM. There are two basic types of electron guns in current use: thermionic electron gun and field emission electron gun. The diameters of the electron beam originating from these gun types are about 20-50 μm and 10 nm, respectively. Thus, field emission SEM (FESEM) is the electron source of choice for high-resolution SEM images.

The morphology of the $BiVO_4$ samples was investigated by scanning electron microscopy (SEM) using a SEM FEI Quanta Inspect 20.

2.4. Raman Analysis

Raman spectroscopy is a spectroscopic technique used in condensed matter physics and chemistry to study vibrational, rotational, and other low-frequency modes in a system. It relies on inelastic scattering, or Raman scattering, of monochromatic light, usually from a laser in the visible, near infrared, or near ultraviolet range.(7)

The Raman effect arises from inelastic scattering of photons by a solid, liquid, or gas. This effect is observed as a shift in the frequency of the scattered light relative to the excitation frequency. These energy transitions arise from molecular vibrations. Because these vibrations involve identifiable functional groups, when the energies of these transitions are plotted as a spectrum, they can be used to identify the molecule. The Raman effect was predicted by Smekal in 1923,(8) and later observed experimentally by Raman and Krishnan in 1928.(9)

Raman spectroscopy is commonly used in chemistry, since vibrational information is very specific for the chemical bonds in molecules. The main advantages of Raman spectroscopy are its high information content, lack of sample preparation, compatibility with aqueous systems, and non-destructive nature.

Raman spectra were obtained by means of a Renishaw inVia Reflex (Renishaw PLC, United Kingdom) micro-Raman spectrophotometer equipped with a cooled charge-coupled device (CCD) camera. Samples were excited with an *Ar-Kr* laser source (648 *nm*), providing a photon flux lower than 60 W/cm^2. The spectral resolution and integration time were 3 cm^{-1} and 30 *s*, respectively. All the Raman spectra excited with the same wavelength directly compared in the following sections were recorded under similar conditions.

2.5. X-ray Photoelecton Spectroscopy

X-ray photoelectron spectroscopy (XPS) is a commonly used surface sensitive chemical analysis technique that operates under ultra-high-vacuum. When soft Xrays irradiate a sample surface, electrons will be ejected from valence and core levels of both surface and near surface atoms.(10) The kinetic energies of ejected photoelectrons are not only characteristic of the atoms from which they are emitted, but can also provide information on the chemical states of those atoms.

It was found that during irradiation, electrons are only emitted from surface atoms when the energy of the X-rays is greater than a critical energy known as the surface work function, which is the energy required to excite an electron from its valence orbital to the continuum. For electrons emitted from lower lying orbitals, the binding energy of the electron also has to be overcome, reducing the kinetic energy of the emitted electron further.(11)

Therefore, the kinetic energy of an ejected electron will be equal to the energy of the incident X-rays minus the work function, minus the binding energy of the electron. In XPS, the kinetic energy of ejected photoelectrons is measured by an analyser. The recorded kinetic energy is translated into a binding energy for the specific atomic orbital of an electron. Since each element has a unique set of energy levels, each element also has a unique set of binding energies for electrons present in these levels.

The XPS technique analyses only the outer 1-10 *nm* of a sample because emitted photoelectrons lose kinetic energy as they travel through the sample. Only photoelectrons generated in the outermost layers of the sample have a short enough escape path to reach the detector.

The XPS spectra were recorded using a PHI 5000 Versa Probe, with a scanning ESCA microscope fitted with an Al monochromatic X-ray source (1486.6 *eV*, 25.6 *W*), a beam diameter of 100 μm, a neutralizer at 1.4 *eV* and 20 *mA*, and a FAT analyzer mode. All the binding energies were referenced to the *C1s* peak at 284.6 *eV* of the surface carbon. The individual components were obtained by curve fitting.

2.6. Photocatalytic and Photoelectrochemical Characterizations

2.6.1. Photocatalytic Oxygen Evolution

The photocatalytic O_2 evolution of the samples was carry out using a solution of silver nitrate $AgNO_3$ (50*mM*; 11*ml*) used as electron acceptor and 10*mg* of sample, both of them dispersed in the reactor at room temperature. The photocatalytic studies were performed using a 39*mL* Pyrex photoreactor. The reactor used consist in a tube with three output, one of them used to insert the oxygen sensor (Clark electrode), other used to feed a constant flow of nitrogen, used like carrier of O_2 and in this way leave the reactor free of O_2, this condition is necessary to start the O_2 evolution test. Finally the third output serves like an output to the gas in the outgassing phase. The internal diameter of the reactor is 22*mm* and the diameters of the three outputs are 20*mm* the central one, and 15*mm*for the lateral outputs, also the reactor have a window of 20*mm* diameter on one side of the reactor. The fig.2.1show a sketch of the reactor used for the O_2 evolution test. In the other hand, the pressure in reactor headspace, the temperature, the nitrogen flow rate, the *pH* and the oxygen concentration in the liquid phase were constantly monitored, and data was collected by using software developed in LabVIEW® platform.

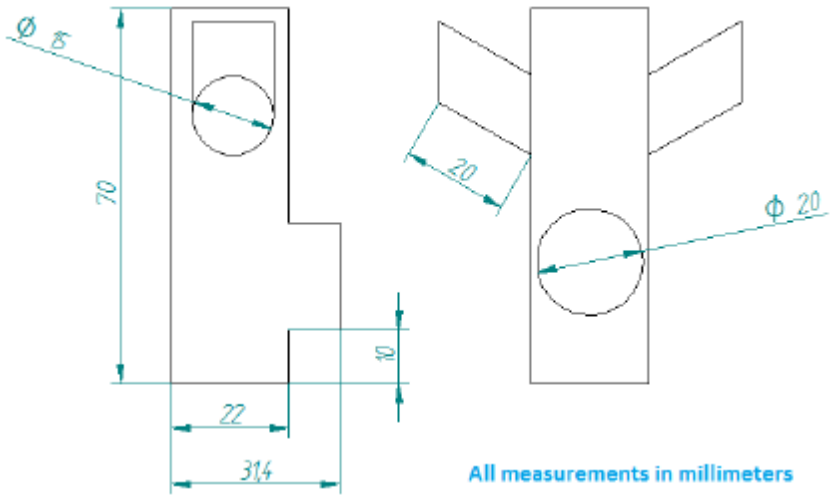

Fig: 2.1. Sketch of the Pyrex reactor used for the O2 evolution test (all measurements in millimeters).

The illumination of the reactor was provided by a plasma lamp (Solaronix model LIFI STA-40), simulating the solar light with an irradiance incident light of 100$mW\ cm^{-2}$ using a photoradiometer Delta Ohm model HD2101:1 to measure and fix the correct value. The illumination was provided during one hour and the oxygen volume fraction P_{O2}, analyzer (expressed in *ppm*) was determined by a Clark electrode and collected using the software above mentioned.

2.6.2. Linear Scan Voltametry (LSV)

Linear sweep voltammetry is a voltammetric method where the current at a working electrode is measured while the potential between the working electrode and a reference electrode is swept linearly in time. Oxidation or reduction of species is registered as a peak or trough in the current signal at the potential at which the species begins to be oxidized or reduced.

The experimental setup for linear sweep voltammetry utilizes a potentiostat and a three-electrode setup to deliver a potential to a solution and monitor its change in current. The three-electrode setup consists of a working electrode, an auxiliary electrode, and a reference electrode. The potentiostat delivers the potentials through the three-electrode setup. A potential, *E,* is delivered through the working electrode. The slope of the potential vs. time graph is called the scan rate and can range from *mV/s* to 1,000,000 *V/s*.(12) At higher scan rates the current is found to increase which improves the signal to noise ratio. Therefore higher scan rates lead to better signal to noise ratios. The working electrode is where the oxidation/reduction reactions occur. The equation below gives an example of an oxidation occurring at the surface of the working electrode. *ES* is the standard reduction potential of *A*. As *E* approaches *ES* the current on the surface increases and when *E=ES* then the concentration of $[A] = [A^-]$ at the surface.(13) As the molecules on the surface of the working electrode are oxidized/reduced they move away from the surface and new molecules come into contact with the surface of the working electrode. This flow of molecules to and from the working electrode causes the current.

$$A + e^- = A^-, E_s = 0.00V$$

Oxidation of molecule *A* at the surface of the working electrode.

The auxiliary and reference electrode work in unison to balance out the charge added or removed by the working electrode. The auxiliary electrode balances the working electrode, but in order to know how much potential it has to add or remove it relies on the reference electrode. The reference electrode has a known reduction potential. The auxiliary electrode tries to keep the reference electrode at a certain reduction potential and to do this it has to balance the working electrode.(14)

2.6.3. Chrono-amperometry

With the chronoamperometry, the current is measured versus time as a response to a (sequence of) potential pulse. The recorded current can be analyzed and its nature can be identified from the variations with time. For example: at short times the capacitive current is dominant ($\propto e@\ tRC$; with *R*= solution resistance and *C*=capacitance) while at longer time scales, the diffusion limited faradaic current might prevail ($\propto t@\ 12$). Here in we employed chronoamperometry in order to find out the stability of the electrode for different lengths of times.

2.6.4. Electrochemical Impedance Spectroscopy (EIS)

Impedance spectroscopy is considered versatile powerful technique to study of the electrical properties of many materials and their interfaces with electronically conducting electrodes.(15) Impedance is a generalised form of resistance, which takes into account the contributions from resistors, capacitors and inductors. As the ohmic resistance is the DC circuit resistance, impedance can be considered as the AC circuit resistance, which describes the amplitudes of the voltage and current and it describes also the relative phases. Impedance can also be defined as the frequency domain ratio of voltage and current.(15) Resistance is defined in Ohm's law (eq. 2.3) and similarly impedance is defined in eq. 2.3.

Ohm's law states: $R = \frac{E}{I}$

Impedence Z: $Z = \frac{\Delta E}{\Delta I}$ *Eq→2.3*

Here, ΔE and ΔI are the peak amplitude of an alternating voltage and resultantalternating current, respectively. However, impedance is a vector quantity: it containsboth a magnitude $(\Delta E/\Delta I)$ and a direction. In this case a phase separation between the potential and current can be defined.

In many cases, impedance depends on the applied frequency. That is for every applied frequency there is a certain value of impedance amplitude $|Z|$ and phase shift θ. Drawing the relationship between the real and imaginary components of impedance in the complex plane (or Nyquist plot) provides a diagnostic tool. By connecting the different magnitude points of impedance, as a function of applied frequency, diagnostic elements such as a semicircle for activation controlled processes are observed. These elements can be rationalized with mathematical models describing the relationship between real part of impedance (I_m or $Z``$) and the imaginary part of impedance (R_e or $Z`$).

Electrochemical Impedance Spectroscopy (EIS) measurements were conducted in the 100 *mHz* to 1*MHz* frequency range, with an amplitude of 25 *mV*, under different applied DC potentials in the -0.3 *V* to 0.9 *V* vs. *Ag/AgCl* range, with 0.3 *V* steps. The EIS data were modeled using Z-SimpWin (EChemSoftware).

2.6.5. Incident-Photon-to-Current-Efficiency (IPEC)

"The IPCE value corresponds to the photocurrent density produced in the external circuit under monochromatic illumination of the cell divided by the photon flux that strikes the cell".(7)It is obtained by equation 2.4:

$$IPEC(\lambda) = \frac{1240 J_{ph}}{\lambda I} \qquad Eq \rightarrow 2.4$$

J_{ph} is the short-circuit photocurrent density generated by the monochromatic light, λ and I are the wavelength and intensity of the monochromatic light.

The IPCE can also be expressed as the product of the light harvesting efficiency (LHE), the quantum yield of hole injection (Φ_{inj}), and the efficiency of collecting the holes at the FTO substrate (η_{coll}).

$$IPEC(\lambda) = LHE(\lambda)\phi_{inj}\,\eta_{coll} \qquad Eq \rightarrow 2.5$$

The absorbed photon-to-current conversion efficiency (APCE) can be estimated from the ratio of IPCE and LHE. It is a better measure of the intrinsic light conversion efficiency.

$$APCE(\lambda) = IPEC(\lambda)/LHE(\lambda) \qquad Eq \rightarrow 2.6$$

2.7.References

1. Pankove, J. L. Optical Processes in Semiconductors; Prentice Hall: Englewood, Cliffs, New Jersey, 1971.
2. Finlayson, A. P.; Tsaneva, V. N.; Lyons, L.; Clark, M.; Glowacki, B. A.,Phys. Status Solidi A, 2006, 203, 327-335.
3. Cullity, B. D. Elements of X-Ray Diffraction; Addison-Wesley: Reading, MA, 1967.
4. J. Langford and A. Wilson, "Scherrer After 60 Years - Survey And Some New Results In Determi- nation," *J. Appl. Crystallogr.*,1978, 11, 102-113.
5. Goldstein. J. I, Newbury. D. E, Echlin. P, Scanning Electron Microscopy and X-ray Microanalysis, 2nd ed, Plenum Press, New York and London, 1992.
6. Grundy P J, Jones G A, Electron microscopy in the study of materials, Edward Arnold Publishers Limited, 1976
7. http://en.wikipedia.org/wiki/Raman_spectroscopy
8. Smekal A, Die Naturwissenschaften, 1923, 43, 873.
9. Raman C V, Krishnan K S, Nature, 1928, 121, 501.

10. Moudler J F, Stickle W F, Sobol P E, Bomben K D, Chastain J (editor), Handbook of X-ray photoelectron spectroscopy, 2nd Edition, ISBN: 0962702625, Perkin Elmer Corporation, Minnesota, 1992.

11. Wagner C D, Riggs W M, Davis L E, Mulder J F, Muilenburg G E (Editor), Handbook of X-ray photoelectron spectroscopy, 1st Edition, ISBN: 0962702621, Perkin Elmer Corporation, Minnesota, 1979.

12. http://www.files.chem.vt.edu/chem-ed/echem/linsweep.html

13. http://mail.chiangmai.ac.th/~scijjkmn/voltammetry.htm

14. F. A. Settle, Handbook of Instrumental Techniques for Analytical Chemistry, Prentice-Hall, Inc., 1997.

15. Alexander, C.; Sadiku, M., Fundamentals of Electric Circuits, 3, revised ed., McGraw-Hill, New York, 2006, 387-389

16. Grätzel, M.,Recent Advances in Sensitized Mesoscopic Solar Cells, Acc. Chem. Res. 2009, 42, 1788–1798.

3. Chapter 3. Evaluation of the Parameters Affecting the Visible-Light-Induced Photocatalytic Activity of Monoclinic $BiVO_4$ for Water Oxidation

3.1. Introduction

Since solar energy is the most abundant energy source, it has been widely exploited for thermal and electrical power generation.(1,2) However, because of the greater convenience of chemical energy storage, such as H_2, compared to electricity, solar fuels have been considered as one of the most promising technological concepts, because of their potential higher efficiency and environmental suitability.(3−5)

In this context, the photocatalytic water splitting into H_2 and O_2 is a topic of current interest.(5,6) Furthermore, the development of a catalyst that can utilize the entire electro-magnetic spectrum is preferable in order to enhance the overall water splitting efficiency of photocatalysts.(7) Several water oxidation photocatalysts have been developed and assessed over the last few decades,(7−10) and it has been reported that $BiVO_4$ is one of the most active O_2 evolution photocatalysts,(7,11) because of its relatively low band gap of ∼2.4 *eV* for the monoclinic phase,(12) which enables a more efficient use of visible light, and due to the adequate position of the conduction and valence bands compared to the potential of water oxidation.(11) In addition, $BiVO_4$ is a nontoxic and relatively abundant material.(11,13)

It has been reported that, of the three occurring phases of $BiVO_4$-*i.e.*, scheelite-tetragonal *(s-t)*, zircon-tetragonal *(z-t)*, and scheelite-monoclinic *(s-m)*-the latter is highly active for O_2 evolution under visible-light irradiation, because of its particular crystal and electronic structure.(12,14) However, there is still a lack of knowledge concerning the physical properties of $BiVO_4$ that lead to high photocatalytic activity, as well as of the formation processes correlated to this phenomenon. Several synthesis methods have been utilized to prepare $BiVO_4$ powders, above all solid-state, aqueous-based, and hydro-thermal methods.(11,15−18) A simple solution-based preparation method, under acidic conditions, which involves the calcinations of the obtained $BiVO_4$ precipitates at different temperatures,has been applied here. An in-depth analysis of some of the important physical parameters of as-obtained products has made it possible to make a coherent correlation with the different photocatalytic O_2 evolution activities. The information gained from this analysis contributes to the better under-standing of the main parameters affecting the activity and will ultimately lead to the optimized synthesis of more-efficientphotocatalytic materials.

3.2. Experimental details

3.2.1. Preperation of Photocatalyst

Samples of $BiVO_4$ powders were synthesized by dissolving 5 *mmol* of bismuth nitrate pentahydrate, $Bi(NO_3)_3{\cdot}5H_2O$ (Sigma−Aldrich) in 100 *mL* of 1 *M* HNO_3 until a clear solution was observed (ca. 30 *min*); 5 *mmol* of ammonium metavanadate, NH_4VO_3 (Sigma−Aldrich) was then added to the mixture, which was stirred overnight. The precipitate was collected by

means of centrifugation, washed three times in distilled water and once in ethanol and then dried at 80 °*C* overnight. Finally, the samples were calcined in air at different temperatures (350, 450, 550, 700, and 800 °*C*, respectively) for 3 *h*.

3.2.2. Characterization

Samples were characterized by X-ray diffraction (XRD) using an X'Pert Phillips diffractometer equipped with *Cu Kα* radiation (λ = 1.5418 *Å*) at 40 *kV* and 30 *mA*. All the patterns were recorded in the range of 5°–60° at a step size of 0.02 °. Ultraviolet–visible (UV-vis) diffuse reflectance spectra were recorded on a UV -vis Varian Cary 5000 spectrophotometer, using a quartz cell suitable for powder measurements. The morphology of the samples was investigated by field-emission scanning electron microscopy (FE-SEM) taken with a high-resolution FE-SEM instrument (LEO 1525). Raman spectra were obtained by means of a Renishaw in Via Reflex (Renishaw PLC, United Kingdom) micro-Raman spectrophotometer equipped with a cooled charge-coupled device (CCD) camera. Samples were excited with an *Ar–Kr* laser source (648 *nm*), providing a photon flux lower than 60 W/cm^2. The spectral resolution and integration time were 3 cm^{-1} and 30 *s*, respectively. All the Raman spectra excited with the same wavelength directly compared in the following sections were recorded under similar conditions.

3.2.3. Photcatalytic Activity Test

Photocatalytic O_2 evolution of the samples was carried out from a silver nitrate ($AgNO_3$) solution (50 *mM*, 110 *mL*), which was used as an electron acceptor. In a typical test, *ca*. 100 *mg* of overnight-outgassed $BiVO_4$ powders were dispersed in the $AgNO_3$ solution in a 200 cm^3 Pyrex reactor cell equipped with an external cooling jacket to maintain a constant temperature. Argon gas was used as a carrier fluxed in the reactor cell under dark conditions in order to evacuate the air inside, and a constant flow of 12 $mL min^{-1}$ was kept during the test. The reactor cell was side-illuminated with a simulated solar light by using a plasma lamp (Solaronix, model LIFI STA-40), whereas the irradiance of incident light was measured to be 100 $mW cm^{-2}$ using a photoradiometer (Delta Ohm, model HD2101.1). Illumination was maintained for 1 *h* and the amount of evolved O_2 was determined in the out-flowing gas using a gas chromatograph (Varian, Model 490-μGC; Molsieve 5*A* column, 10 *m*, micro-TCD detector) until no traces of O_2 were measured, and the cumulative O_2 evolution over 1 *h* of illumination was estimated by the integration of the GC measurements over time.

3.3. Results and Discussion

3.3.1. Characterization of $BiVO_4$ Material

The XRD patterns of the $BiVO_4$ samples calcined at different temperatures are shown in Fig: 3.1; all these samples exhibit the scheelite-monoclinic *(s-m)* phase, as their diffraction peaks are in good agreement with the standard Joint Committee on Powder Diffraction Standards (JCPDS) Card No. 14-0688 (space group *I2/a*, a = 5.195 *Å*, b = 11.701 *Å*, c = 5.092 *Å*, β =90.38°). The crystallite sizes of the samples were estimated using the Scherrer formula:(19)

$$D = \frac{K\lambda}{\beta \cos \theta} \qquad Eq \rightarrow 3.1$$

where$D$ is the approximate crystallite size, λ is the wavelength of the X-ray radiation (0.15418 *nm*); K is the shape factor (0.9); β is the peak width at half-maximum height, corrected for instrumental broadening; 2θ = 30.6°. Moreover, all the samples show the characteristic peak splitting diffractions at 2θ = 18.5°, 35°, and 46°.(20) Although a monoclinic phase was observed at each calcination temperature, the splitting of these characteristic peaks became more pronounced as the calcinations temperature increased, and this is most likely a sign of the increasing degree of crystallinity of the *(s-m)* phase in the $BiVO_4$ samples.(20,21) Moreover, this trend was also confirmed by the further increased calcination temperature of 800 °*C* (see Fig.3.1, Table 3.1). However, higher temperature would not be appropriate, because of the approaching melting point of $BiVO_4$ and also the economic point of view. No crystallinity was observed at lower temperature (100 °*C*) as the sample remained amorphous without any activity.

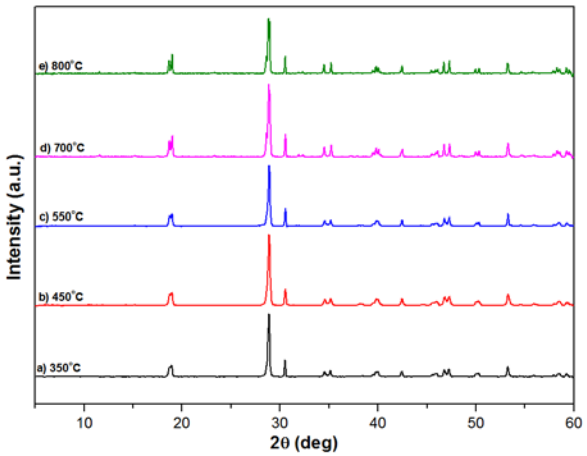

Figure:3.1. XRD patterns of the $BiVO_4$ samples synthesized at different calcination temperatures (a) 350, (b) 450, (c) 550, (d) 700, and (e) 800 °*C*.

The FE-SEM images of the $BiVO_4$ powders are shown in Fig.3.2. Significant differences can be observed between the different samples. The samples calcined at 350 and 450 °*C* (Fig.3.2a and 3.2b) show crystals with well-defined surfaces and a low degree of agglomeration. The powder samples calcined at 550, 700, and 800 °*C* (panels *c-e*) show a clear variation in morphology and in the degree of agglomeration of the particles, probably due to increased sintering at the higher calcination temperatures.

Table 3.1. Physical Properties and O_2 Evolution Activities of $BiVO_4$ Samples Synthesized at Different Calcination Temperatures

sample		BET surface area [m^2/g]	crystallite size [nm]	band gap [eV]	stretching Raman shift V–O^I [cm^{-1}]	bond length V–O^I [Å]	cumulative O_2 evolution [μmol g^{-1} catalyst]
(a)	350 °C	0.11	79	2.49	825.30	1.6964	2.6
(b)	450 °C	0.10	68	2.48	825.95	1.6960	5.6
(c)	550 °C	0.09	80	2.41	826.62	1.6956	17.9
(d)	700 °C	0.07	95	2.39	827.59	1.6950	57.6
(e)	800 °C	0.06	109	2.38	828.86	1.6936	60.9

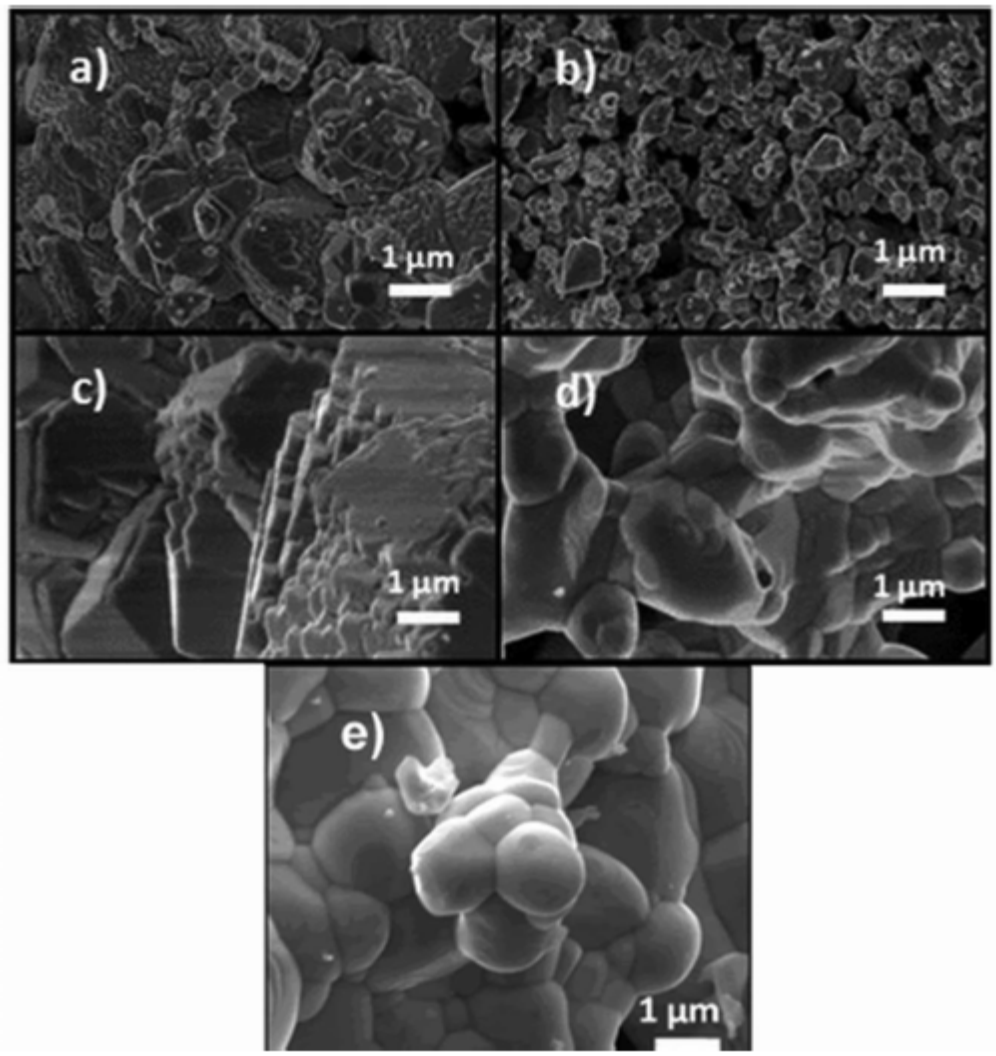

Figure:3.2. Field-emission scanning electron microscopy (FE-SEM) images of *$BiVO_4$* samples synthesized at different calcination temperatures: (a) 350, (b) 450, (c) 550, (d) 700, and (e) 800 °*C*.

Diffuse reflectance spectroscopy (DRS) has been used to calculate the electronic states of the semiconductor materials. The DRS analyses of the *$BiVO_4$* samples, calcined at different temperatures, are shown in Fig.3.3. All the samples show absorption in the visible region of the electromagnetic spectrum, thus offering information on the monoclinic nature of the *$BiVO_4$* samples.(12) Changes in the absorption edges can be observed for the four *$BiVO_4$* samples. A red shift was observed for the samples as the calcination temperature was increased. The band gaps were calculated using the Tauc plot and resulted to be 2.49, 2.48, 2.41, 2.39, and 2.38 *eV* for the samples calcined at 350, 450, 550, 700, and 800 °*C*, respectively.

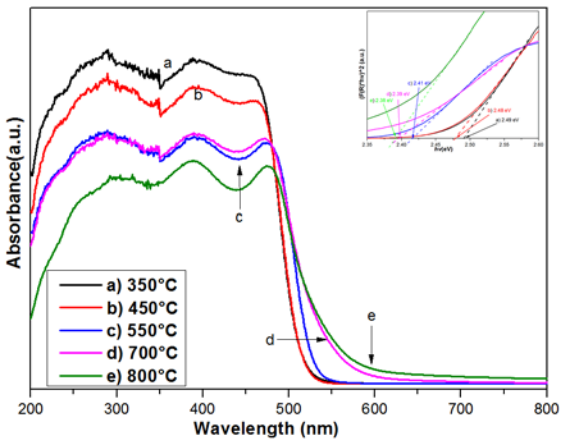

Figure:3.3. Ultraviolet-visible (UV−vis) diffuse reflectance spectra of $BiVO_4$ powders synthesized at different calcination temperatures: (a) 350, (b) 450, (c) 550, (d) 700, and (e) 800 °*C*. Inset shows Tauc plots, revealing the effect of calcination temperature on the band-gap energy shift.

The Raman spectra of the $BiVO_4$ powders were excited using a red (648 *nm*) laser; the corresponding spectra are shown in Fig.3.4. Raman spectroscopy can provide structural information and is also a sensitive method for the investigation of the crystallization, local structure, and electronic properties of materials. Raman bands of ∼210, 324, 366, 640, 710, and 826 cm^{-1} were observed for all the samples. These are the typical vibrational bands of $BiVO_4$.(18,20,22) The structural information of $BiVO_4$ is obtained from the band centered at 210 cm^{-1}. The asymmetric and symmetric formations of the VO_4 tetrahedron are given by the bands centered at 324 and 366 cm^{-1}, respectively.

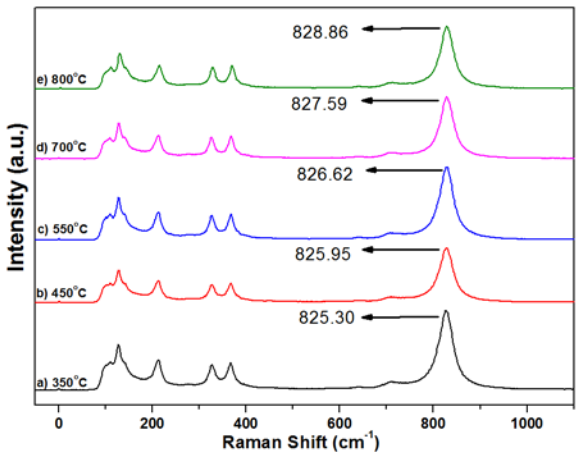

Figure:3.4. Raman spectra of the $BiVO_4$ samples synthesized at different calcination temperatures: (a) 350, (b) 450, (c) 550, (d) 700, and (e) 800 °*C* excited by means of a red-line laser (648 *nm*).

The Raman band at 640 cm^{-1} can be assigned to the asymmetric stretching vibration of the shorter *V*−*O* bond. The stretching modes of the two vibrational modes of the *V*−*O* bonds

are determined by the bands centered at 710 and 826 cm^{-1}. These two bands provide valuable information on the structural variations in the powder samples calcined at different temperatures. A positive shift in the vibrational mode of $V-O$, which varies from 825.30 cm^{-1} to 828.86 cm^{-1}, has been observed. The shift follows a linear trend with the calcination temperature, that is, 825.30, 825.95, 826.62, 827.59, and 828.86 cm^{-1} for 350, 450, 550, 700, and 800 °C, respectively (see Table 1). This shift could be correlated to the variations in bond length of the $V-O$, whichcan be calculated by means of eq 3.2. The Raman stretching frequencies and the respective metal−oxygen bond lengths have an inverse relationship. This means that a higher stretching frequency corresponds to a lower metal−oxygen bond length.

$$\nu(cm^{-1}) = 21349\ exp\left(-1.9176R(\text{Å})\right) \qquad Eq \rightarrow 3.2$$

If the following expression for the bond length(23,24) is utilized, where ν is the stretching Raman frequency for $V-O$, it can be seen that the bond length varies over a range of 1.6964−1.6950 $Å$ for the 350−800 °C samples, respectively.

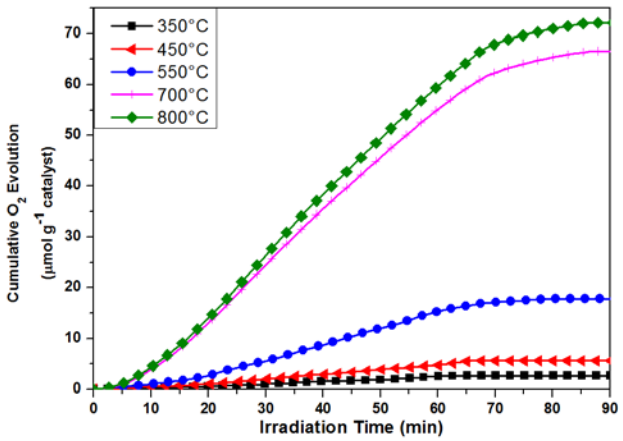

Figure:3.5. Photocatalytic activity of O_2 evolution on $BiVO_4$ calcined at different temperatures.

The synthesized $BiVO_4$ samples were all investigated to determine their photocatalytic O_2 evolution activity ($AgNO_3$ was used as a sacrficial reagent). The cumulative O_2 evolution of the four samples synthesized at different calcination temperatures is shown in Fig.3.5. It can be observed that the photocatalytic activity increases as the calcination temperature increases. The total amount of O_2 evolved after 1 h of illumination under simulated solar irradiation for the samples calcined at 350, 450, 550, 700, and 800 °C was 2.6, 5.6, 17.9, 57.6, and 60.9 $\mu mol\ g.catalyst^{-1}$,respectively.

3.3.2. Photocatalytic Water Oxidation

It has been noted here that certain parameters, such as the crystallite sizes that can be acquired from X-ray diffraction (XRD) and the band gap that is obtained from UV-vis spectroscopy, are very important for the water oxidation reaction. The crystal sizes werecalculated according to eq 3.1. As the calcination temperature increases, there is an

increase in the crystallite size of the powder samples. As shown in Table 3.1, because of aggregationat higher temperature, an opposite trend has been observed in the relation of calcination temperature with BET specfic surface area. However, because of the liquid–solid reaction phase, surface area has no specific role here to affect the activity. Moreover, there is a good correlation between crystalline size, band gap, *V–O* bond length, and O_2 evolution, as can be seen in Table 3.1 and Fig.3.6. Although all the samples showed the same monoclinic phase, differences that describe small variations in the structural parameters of the powder samples were observed among the intensities and half-widths of the peaks. This can be elucidated from the UV-vis spectra and Raman analysis. The differences in the intensities and peak position of the bands in the Raman spectra clearly demonstrate the variations in the local crystal structure of the powder samples, as the frequencies related to the VO_4 tetrahedron and *V–O* bonds are directly related to the interactive forces between the Bi^{3+} and V^{5+} cations. It can be noticed, from the relative intensities of the Raman spectra, that VO_4^{3-} tetrahedrons with different VO_4 space symmetries were formed. It can also be noticed that variations in one of the *V–O* bond lengths can be explained on the basis of the packing of the structure.

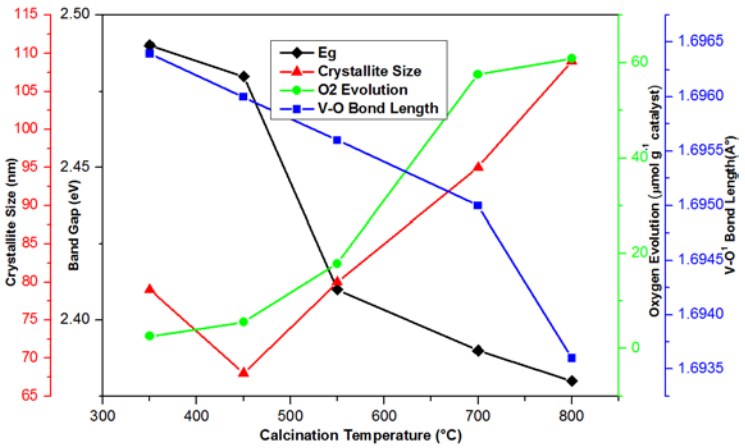

Figure:3.6. Correlation among characteristic parameters of $BiVO_4$ with O_2 evolution.

The stronger the packing, the shorter the *V-O* bond length and the higher the photocatalytic activity. This can be directly correlated to the lone pair distortion around the *Bi* cation, since it has a negative effect on the *V-O* bond length. Therefore, there is more distortion in lone pairs in samples calcined at 700 and 800 *°C* than in the samples calcined at 350 *°C*. The band structure in (*s-m*) $BiVO_4$ is formed by the *Bi 6s*, *O 2p*, and *V 3d* atomic orbitals; the valence band is formed by means of the hybridization of *Bi 6s* and *O 2p* atomic orbitals, while the conduction band is formed by *V 3d* atomic orbitals.(25) A distinct variation has been observed in the electronic structure of the samples when distortion of the $VO4^{3-}$ tetrahedron occurs. This distortion is due to the lone pair electron of Bi^{3+} in the local structure of the $BiVO_4$. A change in the extent of the overlapping of *Bi 6s* and *O 2p* orbitals occurs with the distortion of the VO_4^{3-} tetrahedron. This overlapping is directly proportional to the degree of distortion, which, in turn, helps the mobility of the photogenerated holes.18 Thus, on the basis of XRD, Raman, and UV-vis spectroscopy, it can be stated that an increase in crystallinity of the samples leads to an increase in the delocalization of the electron and hole

pairs and greater overlapping between the *Bi 6s* and *O 2p* orbitals, which increases the O_2 evolution activity of $BiVO_4$.

3.4. Conclusions

In this study, the importance of crystal-size and band gap on photochemical water oxidation has been confirmed. The importance of using the Raman analysis to understand the variations in a crystal structure has also been explained in detail. Thus, if the crystal size and the band gap are taken into consideration, it would be possible to improve the activity of the $BiVO_4$ photocatalyst.

3.5. References

1. Braham, R. J.; Harris, A. T., Review of major design and scale-up considerations for solar photocatalytic reactors.,*Ind. Eng. Chem. Res.,* 2009, 48, 8890−8905.

2. Moriarty, P.; Honnery, D., What is the global potential for renewable energy?,*Renew. Sust. Energy Rev.,* 2012, 16, 244−252.

3. Turner, J.; Sverdrup, G.; Mann, M. K.; Maness, P.-C.; Kroposki, B.; Ghirardi, M.; Evans, R. J.; Blake, D., Renewable hydrogen production.,*Int. J. Energy Res.,* 2008, 32, 379−407.

4. Ampelli, C.; Centi, G.; Passalacqua, R.; Perathoner, S. Synthesis of solar fuels by a novel photoelectrocatalytic approach.,*Energy Environ. Sci.,* 2010, 3, 292−301.

5. Barber, J., Photosynthetic energy conversion: Natural and artificial,*Chem. Soc. Rev.,* 2009, 38, 185−196.

6. Lewis, N. S.; Nocera, D. G., Powering the planet: Chemical challenges in solar energy utilization,*Proc. Natl. Acad. Sci. U.S.A.,* 2006, 103, 15729−15735.

7. Abe, R., Recent progress on photocatalytic and photoelectrochemical water splitting under visible light irradiation.,*J. Photochem. Photobiol. C. Photochem. Rev.,* 2010, 11, 179−209.

8. Kudo, A.; Miseki, Y., Heterogeneous photocatalyst materials for water splitting,*Chem. Soc. Rev.,* 2009, 38, 253−278.

9. Fujishima, A.; Honda, K., Electrochemical photolysis of water at a semiconductor electrode, Nature 1972, 238, 37−38.

10. Bensaid, S.; Centi, G.; Garrone, E.; Perathoner, S.; Saracco, G., Towards artificial leaves for solar hydrogen and fuels from carbon dioxide,*ChemSusChem,* 2012, 5, 500−521.

11. Park, Y.; McDonald, K. J.; Choi, K. S., Progress in bismuth vanadate photoanodes for use in solar water oxidation,*Chem. Soc. Rev.,* 2013, 42, 2321−37.

12. Kudo, A.; Omori, K.; Kato, H., A novel aqueous process for preparation of crystal form-controlled and highly crystalline $BiVO_4$ powder from layered vanadates at room

temperature and itsphotocatalytic and photophysical properties,*J. Am. Chem. Soc.*, 1999,121, 11459−11467.

13. Gotić, M.; Musić, S.; Ivanda, M.; Šoufek, M.; Popović, S.,Synthesis and characterisation of bismuth(III) vanadate,*J. Mol. Struct.*,2005, 744−747, 535−540.

14. Zhao, Z.; Li, Z.; Zou, Z., Electronic structure and opticalproperties of monoclinic clinobisvanite *$BiVO_4$*,*Phys. Chem. Chem.Phys.*, 2011, 13, 4746−53.

15. Wang, D.; Jiang, H.; Zong, X.; Xu, Q.; Ma, Y.; Li, G.; Li, C.,Crystal facet dependence of water oxidation on *$BiVO_4$* sheets undervisible light irradiation,*Chem.Eur. J.*, 2011, 17, 1275−1282.

16. Kudo, A.; Ueda, K.; Kato, H.; Mikami, I., Photocatalytic *O_2*evolution under visible light irradiation on *$BiVO_4$* in aqueous *$AgNO_3$*solution,*Catal. Lett.*, 1998, 53, 229−230.

17. Tokunaga, S.; Kato, H.; Kudo, A., Selective preparation ofmonoclinic and tetragonal *$BiVO_4$* with scheelite structure and theirphotocatalytic properties,*Chem. Mater.*, 2001, 13, 4624−4628.

18. Yu, J.; Kudo, A, Effects of structural variation on thephotocatalytic performance of hydrothermally synthesized *$BiVO_4$*,*Adv. Funct. Mater.*, 2006, 16, 2163−2169.

19. Langford, J. I.; Wilson, A. J. C., Scherrer after sixty years: Asurvey and some new results in the determination of crystallite size,*J.Appl. Crystallogr.*, 1978, 11, 102−113.

20. Kho, Y. K.; Teoh, W. Y.; Iwase, A.; Mädler, L.; Kudo, A.; Amal,R., Flame preparation of visible-light-responsive *$BiVO_4$* oxygenevolution photocatalysts with subsequent activation via aqueousroute,*ACS Appl. Mater. Interfaces*, 2011, 3, 1997−2004.

21. Ke, D.; Peng, T.; Ma, L.; Cai, P.; Jiang, P., Photocatalytic watersplitting for *O_2* production under visible-light irradiation on *$BiVO_4$*nanoparticles in different sacrificial reagent solutions,*Appl. Catal., A*,2008, 350, 111−117.

22. Galembeck, A.; Alves, O. L.,*$BiVO_4$* thin film preparation bymetalorganic decomposition.,*Thin Solid Films*, 2000, 365, 90−93.

23. Brown, I. D.; Wu, K. K., Empirical parameters for calculatingcation-oxygen bond valences.,*Acta Crystallogr., Sect. B: Struct. Sci.*, 1976,32, 1957−1959.

24. Hardcastle, F. D.; Wachs, I. E., Determination of vanadium-oxygen bond distances and bond orders by Raman spectroscopy.,*J. Phys. Chem.*, 1991, 95, 5031−5041.

25. Walsh, A.; Yan, Y.; Huda, M. N.; Al-Jassim, M. M.; Wei, S.-H., Band edge electronic structure of *$BiVO_4$*: Elucidating the role of the *Bi s* and *V d* orbitals,*Chem. Mater.*, 2009, 21 547−551.

4. Chapter 4. Elucidation of Important Parameters of $BiVO_4$ Responsible for Photo-catalytic O_2 Evolution and Insights about the Rate of the Catalytic Process

4.1. Introduction

In the current environmental situation, the increasing anthropogenic CO_2 emissions, the depletion of finite resources and the different socio-economic difficulties suggest the need for low impact societies; in particular, the development of cleaner and more efficient energy systems plays a crucial role in sustainable development (1–3).Among the different energy sources that are currently available,solar energy emerges as one of the best options, due to its widespreadavailability and renewable nature (1,4); however, the storageof this energy, in a suitable form, is problematic due to theintermittency of the source and the difficulty of storing electricalenergy. H_2, or solar fuels in general, have therefore been regardedas one of the most promising technological concepts for the storageof chemical energy, due to its higher efficiency and environmentalfriendliness (5–7).

In this context, the photocatalytic splitting of water into H_2 andO_2 is currently a topic of increasing interest (3,7). In order to realizethis splitting, the main problem is to accomplish the water oxidationhalf-reaction ($2H_2O \rightarrow O2 + 4H^+ + 4e^-$), which is considered asa limiting step since it involves an endergonic reaction that comprisesthe simultaneous transfer of 4 electrons (2,8). Furthermore,the development of a catalyst which can utilize a large section ofthe electromagnetic radiation from the sun that reaches the earthis desirable, in order to enhance overall water splitting efficiency ofphotocatalysts.(9)

Several photocatalysts have been developed and assessed overthe last decades (2,9–11) to carry out the oxidation of water, andit has been found that $BiVO_4$ is one of the most active O_2 evolutionphotocatalysts (9,12), due to (i) its relatively low band gap, being ofaround 2.4 eV for the monoclinic phase (13) and (ii) the adequateposition of the conduction and valance bands compared to the potentialof water oxidation (12).

The characteristics of $BiVO_4$ have been widely studied, in termsof its crystal, electronic and optical properties (13–15). Moreover,it has been identified that among the three possible crystal structures,i.e. zircon–tetragonal (*z–t*), scheelite–tetragonal (*s–t*) andscheelite–monoclinic (*s–m*), only the latter is particularly activeunder visible light, due to the particular overlapping that isachieved in the *Bi6s* and *O2p* orbitals and to the Bi^{3+} lone-pair contributionto raising the energy level to the top of the conductionband (CB), with a resulting decrease in the semiconductor bandgap, and an enhancement of the mobility of the photogeneratedholes (12,13,15,16). On the other hand, it has been described thatthere are facet-dependent characteristics in $BiVO_4$ that lead to ahigher activity for water oxidation, with the (010) facet being regardedas the most active facet, due to different surface-relatedproperties.(8,17) However, this property has only been verifiedexperimentally in very few works (8), and the mechanisms involvedin this phenomena have not yet been studied thoroughly.

The water oxidation half-reaction of O_2 formation catalyzed by$BiVO_4$ is often studied under an $AgNO_3$ solution as a sacrificialagent, due to its high efficacy as an electron scavenger (2,18),although it produces a rapid deactivation of the photocatalyticmaterial after

irradiation.(8,18) In order to circumvent this drawback,a previously reported bubbling reaction system (19,20) and arecently developed mathematical model (21) has been applied inthis work to determine the oxygen production rate more accurately,which also allows one to have a better understanding ofthe deactivation mechanisms that take place in the different samplessynthesized here.

4.2.Experimental

4.2.1. Synthesis of $BiVO_4$ Powers

Bismuth nitrate pentahydrate ($Bi(NO_3)_3\_5H_2O$, analytical grade) and ammonium metavanadate (NH_4VO_3, analytical grade) from Sigma Aldrich were used as received, without any further purification. All the other chemicals used in the experiments werealso of an analytical grade, while deionized water was used for the preparation of the solutions. In a typical preparation process, 3.7 mmol of $Bi(NO_3)_35H_2O$, 3.7 *mmol* of NH_4VO_3 and 12 *mmol* of ammonium carbonate were dissolved in 75 *mL* of 1 *M* HNO_3 and stirred for about 30 *min* at room temperature until a clear solution was obtained. The *pH* of the mixture was adjusted with *NaOH* according to the reaction condition. A series of samples was prepared with different *pH* (0, 2, 4, 6, 8 and 10). The mixture was then sealed in a 100 *mL* Teflon-lined stainless auto-clave and allowed to heat for 12 *h* at 180 °*C* under autogenous pressure in an oven. The precipitate was filtered, washed three times with distilled water and then with ethanol, and dried at room temperature. Finally, the samples were annealed at 450 °*C* for 2 *h*.

4.2.2. Characterization of $BiVO_4$ Powders

The $BiVO_4$ samples were characterized through X-ray diffraction (XRD) using an X'Pert Phillips diffractometer equipped with *Cu Kα* radiation (k = 1.5418 *Å*) at 40 *kV* and 30 *mA*. All the patterns were recorded in the 5–60° range, at a step size of 0.02°. The crystallite sizes of the samples were estimated using the Scherrer formula [22]:

$$D = \frac{K\lambda}{\beta \cos \theta} \qquad Eq \rightarrow 4.1$$

where*D* is the average crystallite size (*nm*), *k* is the wavelength of the X-ray radiation (0.15418 nm); *K* is the shape factor (0.9); *b* is the peak width at half-maximum height, corrected for instrumental broadening; and 2*h* = 30.6°. The UV–Vis diffuse reflectance spectra were recorded on a UV–Vis Varian Cary 5000 spectrophotometer using a suitable quartz cell for powder measurements. The morphology of the samples was investigated by means of scanning electron microscopy (SEM) using a SEM FEI Quanta Inspect 20, which is equipped with EDS probe, employed to have an insight on the sample bulk element composition. X-ray photo-electron-spectroscopy (XPS) was used to characterize the surface composition of some selected $BiVO_4$ samples. The XPS analyses were carried out with a VG Escalab 200-C X-ray photo-electron-spectrometer and a nonmonochromatic *Mg–K* source. A pass energy of 20 *eV*, a resolution of 1.1 *eV*, and a step of 0.2 *eV* were used for high-resolution spectra. The effects of sample charging by referring the spectral line shift to the C1*s* binding energy value of 284.6 *eV* were eliminated.

4.2.3. Photocatalytic Oxygen Evolution

The photocatalytic O_2 evolution tests of the samples were carried out in a bubbling reactor system (19–21), using a silver nitrate $AgNO_3$ solution (50 *mM*; 110 *mL*) as the electron acceptor. In a typical test, ca. 100 *mg* of outgassed $BiVO_4$ powder was dispersed in the $AgNO_3$ solution in a 200 cm^3 Pyrex reactor cell equipped with an external cooling jacket that maintain a constant temperature. The reactor has an internal diameter of 50 *mm* and a 25 *mm* diameter quartz window on one side. Argon gas was used as a carrier and fluxed into the liquid phase through a stainless steel tube with an outside diameter (O.D.) of 1/1600 , under dark conditions, in order to evacuate the air inside. A constant gas flow rate (Q) of 12 $mL\ min^{-1}$ was maintained during the test and the outlet gases were recovered through a stainless steel tube with an 1/800 O.D., while the temperature and pressure were measured by means of a *K*-type thermocouple and a pressure transducer connected to the reactor through a 1/8'' O.D. pipe. The sweeping gas inlet flow rate was controlled by means of a Bronkhorst_mass flow controller. The pressure was controlled through the use of a Swagelok back pressure regulator. The pressure in the reactor headspace, the temperature, the argon flow rate, the *pH* and the oxygen concentration in the liquid phase were constantly monitored, and the data were collected by using a software developed in the LabVIEW®platform. The reactor cell was side-illuminated with AM1.5G simulated solar light, using a plasma lamp (Solaronix model LIFI STA-40).

The irradiance of incident light was measured to be 100 $mW\ cm^{-2}$ using a photo-radiometer Delta Ohm model HD2101.1. The illumination was maintained for one hour and the oxygen volume fraction p_{O2};analyzer (expressed in *ppm*) was determined in the outflowing gas using a gas chromatograph (Varian 490-lGC, Molsieve 5A column 10 m, micro-TCD detector), until no traces of O_2 were detected. Simultaneously, the concentration of O_2 in the liquid phase was measured with a Clark-type sensor (Mettler Toledo, InPro 6050/120) and recorded. The oxygen flow rate at the GC analyzer ϕ_{O2exp}) was calculated as:

$$\Phi_{O_2} = p_{O_2,analyzer} \cdot \frac{Q}{RT} \qquad Eq \rightarrow 4.2$$

where*R* and *T* are the ideal gas constant and the temperature of the liquid, respectively. The cumulative O_2 evolution over 1 *h* of illumination was estimated by integrating (ϕ_{O2exp})(i) versus time, in which "*i*" is each sampling point.

4.2.4. Modeling of the O_2 Evolution Reaction Rate

In order to further understand the O_2 evolution activity of $BiVO_4$, the rate of oxygen production (R_{O2}) was estimated according to the model proposed by Hernández et al. (21), in which R_{O2} is defined as the rate of appearance of oxygen in the liquid phase and is determined by solving the corresponding mass balances in the liquid, gaseous bubble and gas phases of the bubbling reactor system. The experimentally measured quantities of O_2 in the gas ($\phi_{O2\ exp}$) and liquid ($C_{O2\ exp}$) phases are used to perform an iterative point-to-point fitting of the simulated O_2 quantities ϕ_{O2sim} and C_{O2sim}) which leads to the simultaneous determination of R_{O2} and k_La parameter, the latter describing the fluid dynamics and mass transfer of O_2 from the liquid to the gas phase.

4.3.Results and Discussion

4.3.1. Characterization of Hydrothermally Synthesized *BiVO$_4$* Powders

BiVO$_4$ powder samples were prepared by means of hydrothermal synthesis (HTS), and a series of crystallographic patterns was observed as the pH of the synthesis mixture was changed (Fig. 4.1). All these samples exhibited a monoclinic scheelite phase, as their diffraction peaks were in good agreement with the standard Joint Committee on Powder Diffraction Standards (JCPDS) card No. 14-0688 (space group: *I2/a*, *a* = 5.195, *b* = 11.701, *c* = 5.092, *b* = 90.38_). Moreover, all the samples showed the characteristic peak splitting diffractions at *2θ* = 18.5, 35 and 46°(23). No traces of scheelite–tetragonal or zircon–tetragonal phases were observed in these diffraction patterns, which points out the high selectivity of the chosen synthesis method towards the visible-light active monoclinic phase of *BiVO$_4$*(12,13,15). It was also noticed that no undesired tetragonal phase formed in any of the synthesized samples, even though it hadpreviously been found that monoclinic *BiVO$_4$* evolved from an originally tetragonal phase when mild acidic conditions prevailed (24) or due to low temperatures or hydrothermal synthesis periods (25,26).

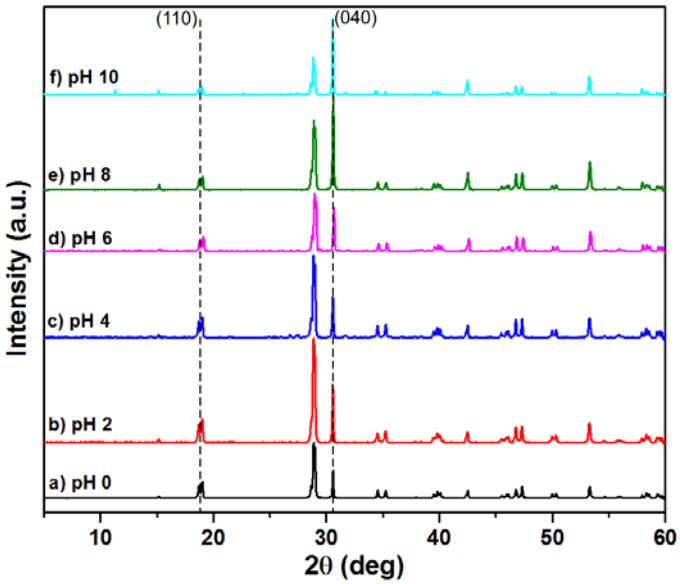

Figure: 4.1. XRD patterns of the *BiVO$_4$* samples synthesized under hydrothermal conditions for different *pH* values (0 to 10).

The XPS spectrum of a representative catalyst, namely the one prepared at a *pH* of 8 and thermally treated for 12 *h*, is shown in Fig. 4.2: as for all the samples prepared at different *pH*s, the characteristic *Bi4f5* and *Bi4f7* peaks, *V2p1* and *V2p3* peaks, and also the binding energies of the different elements, can be attributed to the typical monoclinic scheelite *BiVO$_4$*(27). In addition, the observed *O1s* peak at 529.8 *eV* could be ascribed to the lattice oxygen in crystalline *BiVO$_4$*(27). EDS analysis were also performed on all the samples and gave *Bi:V:O* element ratios of 1:1.37:4.26, which are again consistent with the stoichiometric ratios in *BiVO$_4$*.

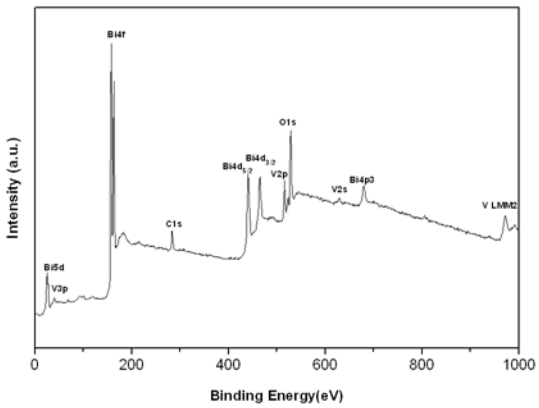

Figure: 4.2. Representative XPS analysis of the *BiVO₄*materials synthesized under hydrothermal conditions: survey spectra obtained for the sample prepared at *pH* 8.

UV–Vis diffuse reflectance spectra (DRS) analysis was used to calculate the electronic states of the *BiVO₄* samples. The DRS of the HTS *BiVO₄* samples are shown in Fig. 4.3. As a crystalline semiconductor, the optical absorption near the band edge follows the$\alpha h\nu = A(h\nu - E_g)^{n/2}$ formula, where α, ν, E_g and A are the absorptioncoefficient, the light frequency, the band gap and a constant,respectively. The variable ‘‘*n*’’ depends on the transition propertiesof the semiconductor, i.e. direct transition (n = 1) or indirecttransition (n = 4). The value of n for *BiVO₄* is equal to 1 (28). Thus,the band gap energy of the *BiVO₄* synthesized powders can be estimatedfrom a plot $(\alpha h\nu)^2$ versus photon energy ($h\nu$), from the interceptof the tangent with the X-axis, as shown in the inset in Fig. 3,appearing to be in the range 2.46–2.54 *eV*, with the lowest valuefound for the *pH* 0 sample and the highest for the pH 6 sample.

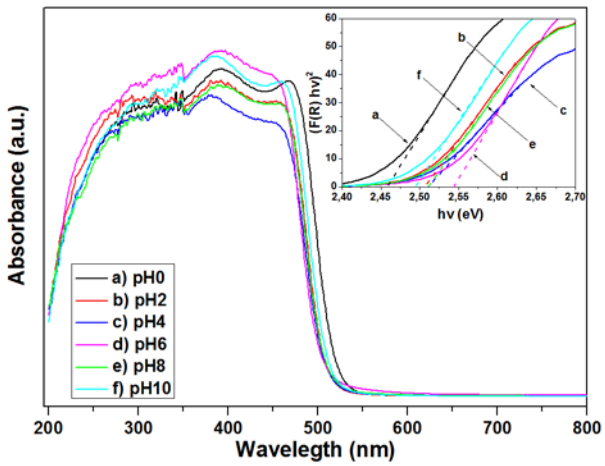

Figure:4.3. UV-Vis diffuse reflectance spectra (DRS) of the *BiVO₄* powders synthesized under hydrothermal conditions at different *pH* values (0 to 10) and the corresponding Tauc plots for the different samples (inset).

4.3.2. Morphology and Formation Process of HTS *BiVO₄* Powders

SEM images were performed in order to verify the morphology changes of the HTS *BiVO₄* powder samples. The *pH 0* sample (Fig. 4.4a) presented very large (1–2μm) and well-crystallized grains, in which the facets were smooth and easily discernible from each other. Subsequently, the *pH2* to *pH6* samples (Fig. 4.4b–d) showed a ‘‘rod-like’’ morphology, with

increasing branching as the *pH* increased, accompanied by an apparent decrease in grain size; e.g. *pH 2* rod-like particles were present at about 200 *nm* of thickness, and they were presumably agglomerated in a unidirectional fashion to form a rod of about 4 *μm*. Finally, the *pH 8* and *pH 10* samples (Fig. 4.4e–f) evolved into highly ramified ‘‘leaf-like’’ structures with an apparent increase in length and flatness of the ‘‘leaves’’ as *pH 10* was reached. Moreover, a decreasing number of single particles was observed in the SEM images as *pH 10* was reached, while, at the same time, this leaf structure seemed to have formed a higher hierarchy level of organization, which could lead one to suppose that a very high *pH* is needed to reach this highly complex morphology and hierarchical structure.

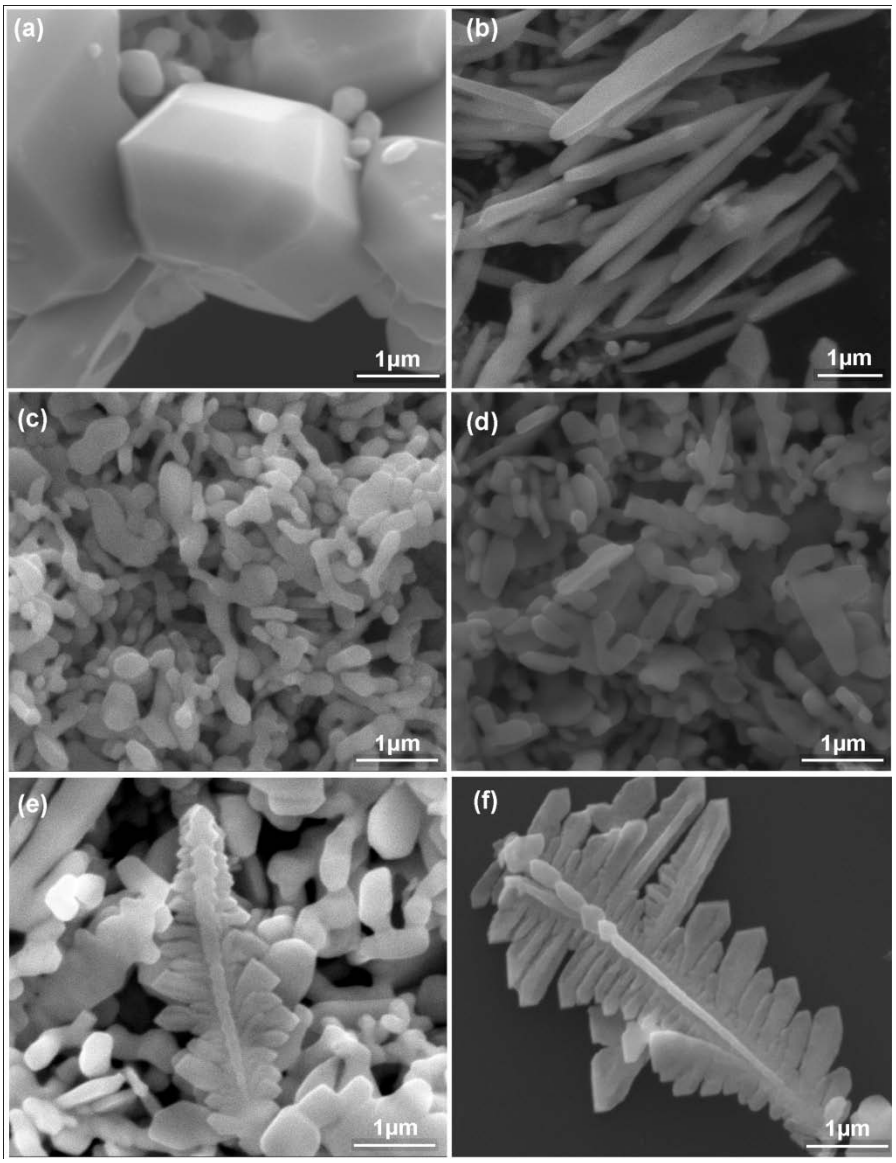

Figue:4.4. SEM images of the $BiVO_4$ samples synthesized under hydrothermal conditions at different *pH* values: a) *pH*0; b) *pH*2; c) *pH*4; d) *pH*6; e) *pH*8; and f) *pH*10.

On the other hand, as observed in the previously introduced XRD patterns of the HTS samples (Fig. 4.1) it is known that the pH increase in these samples coincides with the gradual increase in the (040) diffraction peak (2θ = 30.5°). Previous studies on the hydrothermal synthesis of semiconductor metal oxides, including $BiVO_4$, have pointed out that a similar trend of morphology variations as the *pH* of the synthesis mix was altered, although not very

consistent results were obtained: for instance, the appearance of a tetragonal phase was sometimes observed (29), or only a discrete range of *pH* values was assessed (16). Furthermore, other studies have utilized directing agents, such as $TiCl_3$(8), which might not be suitable from a practical point of view. Therefore, in this study an approach was adopted in which the HTS conditions were finely tuned in such a way that the $BiVO_4$ structure was optimized from a structure and performance point of view, while maintaining an environmentally sound synthesis approach. The synthesis method applied here involves the addition of ammonium carbonate and *pH* modification. This amendment to the hydrothermal reaction conditions led to a particular morphology, as previously mentioned. The nucleation and growth mechanism of monoclinic $BiVO_4$ has been described elsewhere under similar conditions (26,29–32). Therefore, in our experiments, $BiVO_4$ formation can be explained by the degree of solubility of the precursor components, which is regulated by the hydrolysis of bismuth nitrate and its further reaction with vanadate ion to form $BiVO_4$, as described in the following equations (26):

$$Bi(NO_3)_3 + H_2O \leftrightarrow 2HNO_3 + BiONO_3$$
$$BiONO_3 + VO_3^- \leftrightarrow BiVO_4 + NO_3^- \qquad Eq \rightarrow 4.3$$

The hydrolysis of ammonium carbonate and the *pH* increase accelerate the bismuth nitrate hydrolysis and lead to both an extensive precipitation of slightly water-soluble $BiONO_3$ particles and an oversaturation of the synthesis solution, which serves as crystal nucleation centers. This has also been observed, for example, for TiO_2 nanocrystalline powders prepared in hydrothermal conditions, when ammonium carbonate was used as the preparation additive (33), or when $BiVO_4$ was prepared at different *pH* values in a microwave hydrothermal procedure (31). The sudden decrease in crystallite size between the *pH 0* and *pH 2–pH 6* samples is as well a clear consequence of this chemical process, as discussed below. The *pH 2* to *pH 6* samples remained as rods or semi-branched structures after the growth process continued under the imposed hydrothermal conditions. As the *pH* increased further, it would appear that the rods and branches evolved further and a dendritic-type of growth resulted in the formation of ‘‘leaf-like’’ structures with a higher order of hierarchical aggregation (Fig. 4.4e–f), possibly due to the Ostwald ripening mechanism after dissolution and recrystallization of the $BiVO_4$, as has already been described for other $BiVO_4$ aggregation morphologies (30,32). The crystallization process of the *pH 0* sample is evidently different from the rest of the samples, as can be seen from the SEM image (Fig. 4.4a). Unlike the rods and leaves observed in the samples synthesized at *pH 2–10*, the former one presented a polygonal shape, similar to a decahedron, with flat planes and well-defined corners. This type of growth has already been described for $BiVO_4$ under strong acidic conditions, in which the slow precipitation-nucleation process leads to a highly crystalline formation and very large grains, as discussed elsewhere (31). As mentioned above, the HTS conditions applied here led to a gradual increase in the (040) diffraction peak, as can be observed in the XRD profiles of Fig. 4.1. Similarly, Xi and Ye (34) reported the synthesis of so-called ‘‘nanoplates’’ with a highly exposed (001) facet, which was achieved through hydrothermal synthesis in a solubility and nucleation-controlled $BiCl_3$–*BiOCl* system at an optimized *pH* of 6.15. Wang et al. (8), on the other hand, claimed an increase in the (040) facets in hydrothermally synthesized $BiVO_4$ samples due to the introduction of a ‘‘directing agent’’ (i.e. $TiCl_3$) during the synthesis process. In both cases a significant increase of O_2 evolution activity was found, which was

attributed to the increased exposure of one or the other facet. According to DFT calculations of $BiVO_4$ surfaces, (010) has the less surface energy than (110) or (111), and preferential growth can therefore be anticipated in the (010) direction. However, as observed in the XRD profiles, a higher exposure of the (040) facet indicates that increasing the reaction *pH* halts the growth in this direction, and that the relative peak intensity ratio of (040) increases as the *pH* rises (Fig. 4.1). In the present work, a combination of nucleation and growth mechanisms has been observed, which led to the formation of highly organized crystalline structures with a certain preferential exposure of the (040) facet by means of an optimized synthesis procedure under hydrothermal conditions at *pH 10*.

4.3.3. Photocatalytic O_2 Evolution of Hydrothermally Synthesized Samples

The hydrothermally synthesized $BiVO_4$ samples were all investigated to determine their photocatalytic O_2 evolution activity. The cumulative O_2 evolution of 100 *mg* of powder catalyst over 1 *h* of simulated solar light irradiation (AM1.5G) at $100 mWcm^{-2}$ is shown in Fig. 4.5. Although the *pH 0* sample produced the highest amount of oxygen (82.8 $\mu mol\ h^{-1}\ g^{-1}$ catalyst), the total O_2 evolution significantly dropped when the *pH* was increased to 2 (27.5 $\mu mol\ h^{-1}\ g^{-1}\ catalyst$) and kept decreasing (to only 11.5 $\mu mol\ h^{-1}\ g^{-1}$ catalyst) as the *pH* reached 6. A later increase in the O_2 evolution to 25.4 and 38.8 $\mu mol\ h^{-1}\ g^{-1}$ catalyst was observed for the *pH* 8 and *pH* 10 samples, respectively.

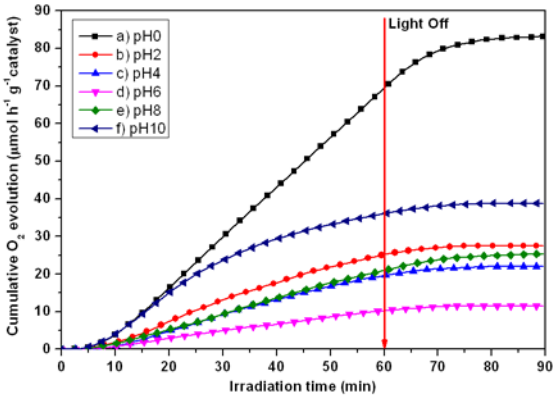

Figure:4.5Photocatalytic O_2 evolution from 50 *mM* $AgNO_3$ solution (110 *mL*) under simulated solar irradiation (AM1.5G, 100 $mWcm^{-2}$) over the $BiVO_4$ powder catalyst (100 *mg*) synthesized in hydrothermal conditions at different *pH* values: a) *pH*0; b) *pH*2; c) *pH*4; d) *pH*6; e) *pH*8; and f) *pH*10.

4.3.4. Determination of the O_2 Production Rate of Hydrothermally Synthesized Samples

In order to gain a more in-depth and accurate understanding of the O_2 evolution mechanisms that took place in the HTS $BiVO_4$ samples, the O_2 production rate, R_{O2} was determined as a function of the irradiation time. It is well known that $BiVO_4/AgNO_3$ systems suffer from a gradual decay in photoactivity over time due to an intrinsic interaction that occurs between the $BiVO_4$ surface and the reacting Ag^+ centers. The $BiVO_4$ surface is progressively covered with photodeposited *Ag* clusters (35), which were observed through SEM imagery on the tested materials: for instance, Fig. 6 clearly shows the *Ag* clusters

deposited on the surface of the *pH 8* catalyst after the photocatalyticreaction. It is believed that reduced *Ag* clusters might occupy reacting active sites on $BiVO_4$ or even act as a light shield against incident irradiation, and therefore decrease the overall photo-efficiency of the catalyst over time (18). Similarly, Bao et al. (36) found that increasing amounts of *Pt* loading above 15 *wt.%* in a CdS nanocatalyst significantly decreased the H_2 evolution under visible light irradiation due to a light shielding effect. Bearing this in mind, a novel approach has been undertaken to determine the actual reaction rate of O_2 evolution of the $BiVO_4$ samples.

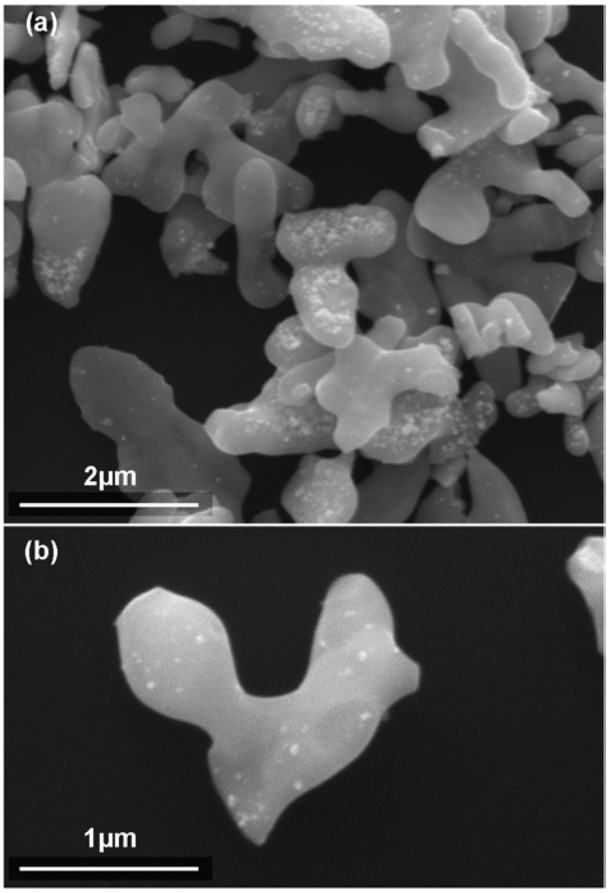

Figure:4.6. Representative SEM analysis of the $BiVO_4$ samples after the photocatalytic O_2 evolution tests: (*a,b*) images corresponding to the HTS sample prepared at *pH* 8.

Some authors have utilized the maximum ‘‘instantaneous’’ rate of O_2 evolution within the first hour of illumination (i.e. before the catalyst deactivates) as an approximation of the O_2 evolution rate (8). However, this is still not the ‘‘true’’ reaction rate and it is considered to be underestimated since the O_2 concentration that the GC measures is buffered by the mass-transport constraints in the liquid and gas phases. As mentioned in Section 2, the O_2 production rate (R_{O2}) was estimated according to the model proposed by Hernandez et al. (21). It should be clarified that R_{O2} is the rate of appearance of oxygen in the liquid phase, which lumps in its value the contributions of the reaction rate at the catalyst surface and the mass transfer of O_2 from the catalyst surface to the bulk of the liquid. The peak of the R_{O2} curve was taken as the maximum rate of O_2 production and reported on a mass basis ($R_{O2;Max}$, in $\mu mol\ h^{-1}\ g^{-1}$ catalyst) in order to be able to compare the results of cumulative O_2 evolution (in $\mu mol\ g^{-1}$ catalyst) for 1 *h* of irradiation as depicted, for example, in Figs. 4.7a and 4.7b for the *pH* 0 and *pH* 10 samples. Fig. 4.8 summarizes the results obtained from the tests on all the HTS samples.

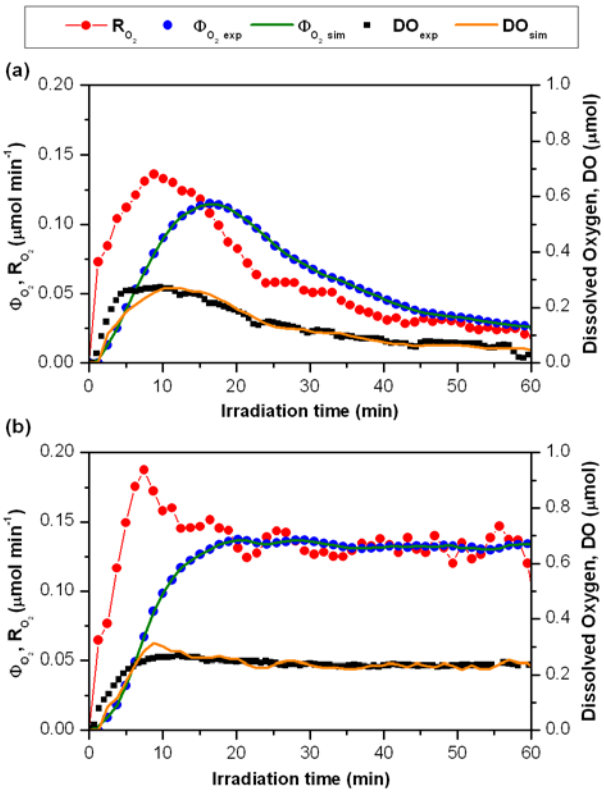

Figure:4.7. Time course of O_2 evolution and estimation of the O_2 production rate (R_{O2}) for the $BiVO_4$ samples synthesized under hydrothermal conditions at *pH* 10 (a) and *pH* 0 (b). Experimental (exp) and simulated (sim) data, according to the bubbling reactor mathematical model (21), of both outlet oxygen flow rate (U_{O2}) and oxygen dissolved in the liquid phase (DO).

It can be observed that the estimated $R_{O2;Max}$values follow the same trend as the cumulative O_2 evolution, for all the samples analyzed. In addition, as expected, $R_{O2;Max}$is always well above the cumulative value and $\phi_{O2\ exp}$is always in-between the cumulative and the production rate curves. Surprisingly, while the $R_{O2;Max}$ for the *pH* 0 sample (Fig. 4.8) is only 26% higher than its corresponding cumulative value after 1 *h*, the $R_{O2;Max}$for *pH* 10 was 131% its cumulative value. These results demonstrate that the typical procedure used in the literature employing batch reactors, which considers the integral values of the evolved (cumulative) oxygen to estimate the rate of O_2 production (8,16,18,34), could be misleading. Such procedure involves a higher uncertainty with respect to the use of an approximated $\phi_{O2\ exp}$ maximum value, and even a higher one compared to the real $R_{O2;Max}$ calculated by using the bubbling reactor and the mathematical model here employed. Even though *pH* 0 outperforms the *pH* 10 sample by far in absolute terms, (about 30% higher), it has here been elucidated that a larger degree of some kind of deactivation takes place on its surface, due to the characteristics exhibited by the latter (i.e. morphology, size and orientation). This deactivation can also be rapidly inferred from the shape of $R_{O2;Max}$ and $\phi_{O2\ exp}$. A sharp increase was observed for *pH* 10 (Fig. 4.7a) in the first minutes of irradiation and then a continuous decrease occurred until the end of irradiation (60 *min*). This deactivation is more likely the result of the light-shielding effect produced by *Ag* deposition on the $BiVO_4$ surface, which has not been observed in the curves referred to *pH* 0 (Fig. 4.7b), whose activity remained almost constant till the end of the test. In a recent work by Li et al. (35) it has been evidenced that $BiVO_4$ presents a facet-selective photo-deposition feature between the (010) and (110) facets,

in which metals are selectively reduced in the former, and oxidized in the latter. The *pH* 10 sample had a much greater exposure of the (040) facet than *pH* 0, as can be seen from the XRD patterns (Fig. 4.1). Therefore it seems probable that most of the reaction sites in the *pH* 10 sample got rapidly covered by *Ag*, and this led to a sharp decrease in the reaction rate overtime, and consequently of the lower cumulative O_2evolution with respect to the samples with less (040) exposure. The results referred to the cumulative O_2 production after 1 *h* of irradiation, and the maximum rate of O_2 production $R_{O2;Max}$, can be also expressed as Turnover Number (TON) and maximum Turnover Frequency (TOF) of this reaction, respectively, which follow the same trend of the previous ones (see Table 4.1). These are here defined as suggested by Kudo and Miseki in (2), and adapted to our case as:

TON = Moles of O_2 formed/Moles of $BiVO_4$ photocatalyst employed.

TOF = Molar rate of O_2 formation/Moles of $BiVO_4$ photocatalyst employed.

It is worth mentioning that this definition leads to values that are lower than TON and TOF referred to the number of active sites on the surface of the photo-catalyst, the latter being of difficult estimation in this specific case.

Table: 4.1 Turnover Number (TON) and maximum Turnover Frequency (TOF) obtained with the HTS $BiVO_4$ samples for the O_2 evolution reaction.

Sample	TON (−)	TOF (h^{-1})
pH 0	2.69E−02	3.40E−02
pH 2	8.10E−03	1.74E−02
pH 4	6.15E−03	1.29E−02
pH 6	3.24E−03	6.92E−03
pH 8	6.80E−03	1.14E−02
pH 10	1.13E−02	2.64E−02

4.3.5. Correlation of the Physical Parameters of HTS $BiVO_4$ to the O_2 Evolution Activity

The crystallite size of the samples was estimated as per the well-known Scherrer formula (22), as previously described. A good agreement was observed between the variation in the crystal size and the maximum O_2 production rate (see Fig. 4.9); as a matter of fact, the largest crystals (167 *nm*) corresponded to the most active of the samples (*pH* 0), whereas the smallest (92 *nm*) was found for the sample with the lowest activity (*pH* 6). The optical properties of the synthesized samples were discussed in Section 2.1, and a summary of the band gap energies (E_g) is shown in Fig. 9. The differences observed between the largest and smallest E_g elucidate the changes in energy states of $BiVO_4$, and are once more in agreement with the lowest and highest O_2 production rates, respectively.

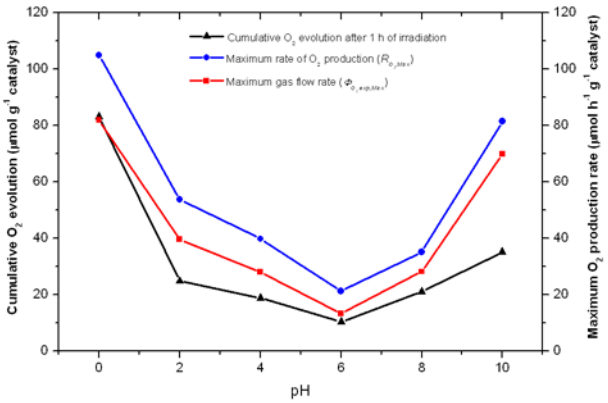

Figure:4.8. Comparison of the maximum O_2 evolution rates for the HTS $BiVO_4$ samples. The cumulative O_2 evolution, after 1 h of irradiation, comprises the total amount of O_2 evolved after 1 *h* of simulated solar light irradiation. $R_{O2;Max}$ was estimated by using the bubbling reactor mathematical model (21), and $U_{O2\ exp\ ;Max}$ was measured experimentally with the GC system.

Finally, the relative intensities between the (040) and (110) facets were estimated as per the corresponding XRD peak intensity ratios of these two facets. The results shown in Fig. 4.9 reveal that no relevant differences occur in the ratio for the samples between *pH* 0 and *pH* 6, below ca. 4, whereas the ratio increases sharply for the samples at *pH* 8 and 10, to 9.4 and 13.2, respectively.

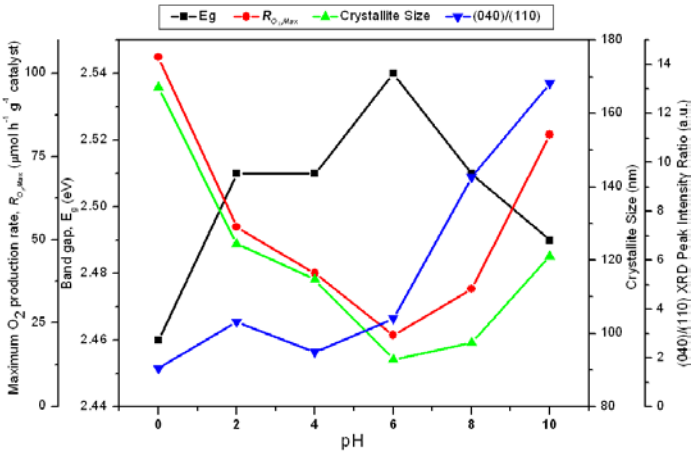

Figure: 4.9. Correlation between the physical parameters and the maximum O_2 production rate ($R_{O2\ ;Max}$) of the $BiVO_4$ samples synthesized under hydrothermal conditions at different *pH* values (0–10).

Considering the analysis performed here, the following explanationscan be drawn. The most important parameter controllingthe O_2 evolution activity is believed to be the crystallite size ofthe samples, since there is a proportional correlation betweenthe mean particles size and catalyst activity. Kho et al. (23) noticedthat flame-synthesized $BiVO_4$ crystallite sizes increased from 47 to71 *nm* as a result of an increased flame temperature resulted in animprovement of the O_2 evolution activity due to an enhanced crystallinityprompted by particle sintering. Likewise, Yu and Kudo (16)found that smaller crystallite sizes in hydrothermal *BiVO4* powdersgenerally corresponded to lower O_2 evolution rates. The

crystalliteshrinkage was in this case attributed to the *pH* increase, and furtherassociated with the loss of the symmetry constraint, or looserstructure due to a diminished distortion of the $BiVO_4$ polyhedrons.Further less distortion would have reduced the *Bi* lone-pair distortioncontribution to the *Bi6s* and *O2p* orbitals and the delocalizationof the electrons and holes, ultimately suppressing the O_2evolution activity.

As described above, the O_2 evolution activity is inversely correlatedto the band gap and directly related to the crystalline size ofthe powder samples. This mutual correlation could be due to twopossible phenomena. The first is directly linked to the aforementionedpotential loss of symmetry constraint in the smaller crystallites,which leads to a smaller contribution of the *Bi6s* overlappingwith *O2p* due to the lone-pair distortion and ultimately to wideningof the transition band gap (13,15,16,20,37). The second couldbe connected to the quantum-size phenomena, in which nanosizedsemiconductor particles exhibit a remarkable change in theirabsorption spectra due to their reduction in size, in comparisonto the bulk materials (38). Kho et al. (23) attributed this quantizationeffect to the higher than normal $BiVO_4$ band gap in the flamesynthesizedparticles of <100 *nm*. However a smaller crystallitesize was not clearly correlated to a higher band gap, as could havebeen expected. Nevertheless, due to the relatively large particlesizes estimated in the present work (>90 *nm*), no significant quantumeffect could be expected, thus the effect local structural variations(and concomitant electron–hole delocalization) is the onlyexplanation for the increase in band gap with a decrease in crystallitesize.The fact that the *pH* 0 sample yields the largest crystal size andlowest band gap, would seem to explain why high O_2 evolutionactivity was observed. This could also explain why the *pH* 6 sampleperformed poorly, as it had the smallest crystallite size and thelargest band gap. However, it would seem that the increase in crystalsize of the last samples (*pH* 8 and 10) cannot fully explain thereactivation of the O_2 evolution, particularly at *pH* 10. Bearing thisin mind, a third parameter was introduced, that corresponds to thepreferential growth orientation of the samples, and which is characterizedby the peak intensity ratio (040)/(110): as alreadyexplained, this ratio increases for the *pH* 8 and *pH* 10 samples. Inaddition, there is a pronounced increase of the O_2 production rate which might be ascribed to the greater exposure of the (040) facets in *pH10*. Although several authors stated that exposing the (040) facet of $BiVO_4$ improves the O_2 evolution activity to a great extent (8), it has here been found that this is a parameter of secondary importance, preceded by the crystallite size and band gap, in the optimization of photocatalytic water oxidation reaction.

4.4.Conclusions

The introduction of ammonium carbonate, a cost effective and non-toxic reagent, has been shown to influence preferential crystal growth of the $BiVO_4$ photocatalyst, along its (040) facet at high *pH*. However, it has been observed, from XRD, UV–Vis and photocatalytic activity tests, that the crystalline size as well as band gap are the main key features to establish its application for photocatalytic oxygen evolution, and that the preferential orientation of the $BiVO_4$ crystal along the (040) facet is a feature of secondary importance in being responsible for this activity. The real reaction rate, that was estimated from a mathematical model taking into account the mass transfer phenomena in the reaction system, perfectly fits the correlations that we obtained from the experimental results. The present work offers an insight into how the photocatalytic activity of $BiVO_4$ can be improved, and how the catalytic activity can be

further enhanced by giving preference to specific parameters, such as the charge transport limitations and the addition of dopants, to fasten the catalytic activity of $BiVO_4$.

4.5.Refeerences

1. OECD/IEA, World Energy Outlook 2011, IEA Publications, Cedex, France, 2011.

2. A. Kudo, Y. Miseki, Heterogeneous photocatalyst materials for water splitting, *Chem. Soc. Rev.*,2009, 38, 253–278.

3. N.S. Lewis, D.G. Nocera, Powering the planet: chemical challenges in solar energy utilization, *Proc. Natl. Acad. Sci. U.S.A.*,2006, 103, 15729–15735.

4. P. Moriarty, D. Honnery, What is the global potential for renewable energy?,*Renew Sustain. Energy Rev.*, 2012, 16, 244–252.

5. J. Turner, G. Sverdrup, M.K. Mann, P.-C. Maness, B. Kroposki, M. Ghirardi, R.J. Evans, D. Blake, Renewable hydrogen production, *Int. J. Energy Res.*,2008, 32, 379–407.

6. C. Ampelli, G. Centi, R. Passalacqua, S. Perathoner, Synthesis of solar fuels by a novel photoelectrocatalytic approach, *Energy Environ. Sci.*, 2010, 3, 292–301.

7. J. Barber, Photosynthetic energy conversion: natural and artificial, *Chem. Soc. Rev.*, 2009, 38, 185–196.

8. D. Wang, H. Jiang, X. Zong, Q. Xu, Y. Ma, G. Li, C. Li, Crystal facet dependence of water oxidation on $BiVO_4$ sheets under visible light irradiation, *Chem. Eur. J.*,2011, 17, 1275–1282.

9. R. Abe, Recent progress on photocatalytic and photoelectrochemical water splitting under visible light irradiation, *J. Photochem. Photobiol. C Photochem. Rev.*2010, 11, 179–209.

10. A. Fujishima, K. Honda, Electrochemical photolysis of water at a semiconductor electrode, *Nature*, 1972, 238, 37–38.

11. S. Bensaid, G. Centi, E. Garrone, S. Perathoner, G. Saracco, Towards artificial leaves for solar hydrogen and fuels from carbon dioxide, *ChemSusChem*,2012, 5,500–521.

12. Y. Park, K.J. McDonald, K.-S. Choi, Progress in bismuth vanadate photoanodesfor use in solar water oxidation, *Chem. Soc. Rev.*, 2013, 42, 2321–2337.

13. A. Kudo, K. Omori, H. Kato, A novel aqueous process for preparation of crystalform-controlled and highly crystalline $BiVO_4$ powder from layered vanadatesat room temperature and its photocatalytic and photophysical properties, *J.Am. Chem. Soc.*,1999, 121, 11459–11467.

14. A. Sleigth, H. Chen, A. Ferretti, D. Cox, Crystal growth and structure of $BiVO_4$,*Mater. Res. Bull.*,1979, 14, 1571–1581.

15. A. Walsh, Y. Yan, M.N. Huda, M.M. Al-Jassim, S.-H. Wei, Band edge electronicstructure of $BiVO_4$: elucidating the role of the *Bi s* and *V d* orbitals, *Chem.Mater.*, 2009, 21, 547–551.

16. J. Yu, A. Kudo, Effects of structural variation on the photocatalytic performanceof hydrothermally synthesized *$BiVO_4$*, *Adv. Funct. Mater.*,2006, 16, 2163–2169.

17. J. Yang, D. Wang, X. Zhou, C. Li, A theoretical study on the mechanism ofphotocatalytic oxygen evolution on *$BiVO_4$* in aqueous solution, *Chem. Eur. J.*,2013, 19, 1320–1326.

18. D. Ke, T. Peng, L. Ma, P. Cai, P. Jiang, Photocatalytic water splitting for *O_2*production under visible-light irradiation on *$BiVO_4$* nanoparticles in differentsacrificial reagent solutions, *Appl. Catal. Gen.*, 2008, 350, 111–117.

19. M. Armandi, S. Hernandez, S. Vankova, S. Zanarini, B. Bonelli, E. Garrone,Visible-light driven oxidation of water as catalyzed by *Co-APO-5* in thepresence of Ru sensitizer, ACS *Catal.*,2013, 3, 1272–1278.

20. S.M. Thalluri, C. Martinez Suarez, M. Hussain, S. Hernandez, A. Virga, G.Saracco, N. Russo, Evaluation of the parameters affecting the visible-lightinducedphotocatalytic activity of monoclinic *$BiVO_4$* for water oxidation, *Ind.Eng. Chem. Res.*, 2013, 52, 17414–17418.

21. S. Hernández, S. Bensaid, M. Armandi, A. Sacco, A. Chiodoni, B. Bonelli, E.Garrone, C.F. Pirri, G. Saracco, A new method for studying activity and reactionkinetics of photocatalytic water oxidation systems using a bubbling reactor,*Chem. Eng. J.*,2014, 238, 17–26.

22. J. Langford, A. Wilson, Scherrer after sixty years: a survey and some newresults in the determination of crystallite size, *J. Appl. Crystallogr.*,1978, 11,102–113.

23. Y.K. Kho, W.Y. Teoh, A. Iwase, L. Maedler, A. Kudo, R. Amarl, Flame preparation of visible-light-responsive *$BiVO_4$* oxygen evolution photocatalysts with subsequent activation via aqueous route, *ACS Appl. Mater. Interface*, 2011, 3, 1997–2004.

24. S. Tokunaga, H. Kato, A. Kudo, Selective preparation of monoclinic and tetragonal *$BiVO_4$* with scheelite structure and their photocatalytic properties, *Chem. Mater.*, 2001, 13, 4624–4628.

25. S. Obregon, A. Caballero, G. Colon, Hydrothermal synthesis of *$BiVO_4$*: structural and morphological influence on the photocatalytic activity, *Appl. Catal. B Environ.,* 2012, 17, 59–66.

26. L. Zhou, W. Wang, L. Zhang, H. Xu, W. Zhu, Single-crystalline *$BiVO_4$* microtubes with square cross-sections: microstructure, growth mechanism, and photocatalytic property, *J. Phys. Chem. C*,2007, 111, 13659–13664.

27. Y. Sun, C. Wu, R. Long, Y. Cui, S. Zhang, Y. Xie, Synthetic loose-packed monoclinic *$BiVO_4$* nanoellipsoids with novel multiresponses to visible light, trace gas and temperature, *Electron. Supple. Inf. Chem. Commun.*, 2009, 4542–4544.

28. B. Zhou, J. Qu, X. Zhao, H. Liu, Fabrication and photoelectrocatalytic properties of nanocrystalline monoclinic *$BiVO_4$* thin-film electrode, *J. Environ. Sci. China*, 2011, 23, 151–159.

29. A. Zhang, J. Zhang, N. Cui, X. Tie, Y. An, L. Li, Effects of pH on hydrothermal synthesis and characterization of visible-light-driven $BiVO_4$ photocatalyst, *J. Mol. Catal. Chem.*, 2009, 304, 28–32.

30. L. Zhou, W. Wang, H. Xu, Controllable synthesis of three-dimensional well defined$BiVO_4$ mesocrystals via a facile additive-free aqueous strategy, *Cryst. Growth Des.*, 2008, 8, 728–733.

31. G. Tan, L. Zhang, H. Ren, S. Wei, J. Huang, A. Xia, Effects of *pH* on the hierarchical structures and photocatalytic performance of $BiVO_4$ powders prepared via the microwave hydrothermal method, *ACS Appl. Mater. Interface*,2013, 5, 5186–5193.

32. H. Jiang, H. Dai, X. Meng, L. Zhang, J. Deng, Y. Liu, C.T. Au, Hydrothermal fabrication and visible-light-driven photocatalytic properties of bismuth vanadate with multiple morphologies and/or porous structures for methyl orange degradation, *J. Environ. Sci. China*,2012, 24, 449–457.

33. F. Wang, J. Xu, S. Lin, W. Cao, Effects of NH^{4+} and Cl^{-} on the preparation of nanocrystalline TiO_2 by hydrothermal method, *Res. Chem. Intermed.*,2013, 39, 1645–1654.

34. G. Xi, J. Ye, Synthesis of bismuth vanadate nanoplates with exposed {001} facets and enhanced visible-light photocatalytic properties, *Chem. Commun.*,2010, 46, 1893–1895.

35. R. Li, F. Zhang, D. Wang, J. Yang, M. Li, J. Zhu, X. Zhou, H. Han, C. Li, Spatial separation of photogenerated electrons and holes among {010} and {110} crystal facets of $BiVO_4$, *Nat. Commun.*,2013, 4.

36. N. Bao, L. Shen, T. Takata, K. Domen, Self-templated synthesis of nanoporous *CdS* nanostructures for highly efficient photocatalytic hydrogen production under visible light, *Chem. Mater.*,2008, 20, 110–117.

37. Z. Zhao, Z. Li, Z. Zou, Structure and energetics of low-index stoichiometric monoclinic clinobisvanite $BiVO_4$ surfaces, *RSC Adv.*,2011, 1, 874–883.

38. H. Zhang, G. Chen, D.W. Bahnemann, Photoelectrocatalytic materials for environmental applications, *J. Mater. Chem.*, 2009, 19, 5089–5121.

5. Chapter 5. Green-Synthesized $BiVO_4$ Oriented along {040} Facets for Visible-Light-Driven Ethylene Degradation

5.1. Introduction

There is considerable interest in the application of semiconductors in the field of photocatalysis following the first report describing the use of TiO_2 for water splitting under UV light.(1−8) This semiconductor can be used not only for water splitting,(9,10) to produce oxygen and hydrogen, but also for the detoxification of polluted water and air.(1) Two of the most important advantages of TiO_2 are its nontoxicity and its low cost. Its major disadvantage is its large band gap (around 3.2 *eV*). Thus, excitation of electrons into its conduction band from the valence band requires UV light, which is a very limited fraction of the solar radiation that reaches the surface of the Earth. Considerable efforts have been made to develop photocatalysts that can use visible light and give activities as good as TiO_2 under UV irradiation. For instance, alkali and alkaline tantalates(11) and $In_{1-x}Ni_xTaO_4$(12) are catalytically active under visible light irradiation. In this paper, we present a strategy to synthesize a visible-light-absorbing photocatalyst, $BiVO_4$, with a band gap of around 2.4 *eV*, which is active for the degradation of ethylene, taken as a reference organic pollutant.

The activity of this photocatalyst is influenced by the concentration of the reactive species over its surface and, inturn, by the morphology and type of the exposed crystalsurfaces. Research in the field of $BiVO_4$ catalysis has grownconsistently in view of different applications for this semiconductor.(5,9) The synthesis of $BiVO_4$, with specific morphologyof the reactive facets, is challenging, and researchers haveattempted to correlate photocatalytic activity to its differentcrystal facets. Indeed, it has been observed that an increase inthe {040} crystal facet has a significant influence on thephotocatalytic activity of $BiVO_4$.(13−15) Some reports havedescribed the preferential growth of the $BiVO_4$ crystal alongthe {040} direction, when a promoting agent, such as $TiCl_3$,(13)is used. It has also been reported that the inclusion ofethanolamine(16) and $NaHCO_3$(17) in the reaction mixture has ledto an increase in the extent of {040} facets. Considerable efforts have been made to obtain the same results without a "green" promoting agent.(18) A successful method is reported here for the synthesis of $BiVO_4$, with preferentially exposed reactive {040} facets, obtained by varying the *pH* of the precursor solution and by of a sustainable structure-directing agent (ammonium carbonate). This photocatalyst shows very good performance toward the oxidation of ethylene, taken as an example of a volatile organic pollutant. Particularly, as detailed and explained later, 6 times higher photocatalytic activities have been measured compared to the best TiO_2 photocatalyst ever produced by our group(6,7) and even 10 times higher than the reference Degussa P25 titania.

5.2. Materials and Methods

Bismuth nitrate pentahydrate [$Bi(NO_3)_3{\cdot}5H_2O$, analytical grade] and ammonium metavanadate (NH_4VO_3, analytical grade) from Sigma Aldrich were used as received, without further purification. All the other chemicals used in the experiments were also analytical grade, while deionized water was used for the preparation of solutions. As in a typical preparation process, 1.81 *g* of $Bi(NO_3)_3{\cdot}5H_2O$, 0.435 g of NH_4VO_3, and 1.16 *g* of ammonium

carbonate were dissolved in 75 *mL* of 1 *M* HNO_3 and stirred for about 30 *min* at room temperature until a clear solution was obtained. The *pH* of the mixture was adjusted with *NaOH* according to the desired reaction condition. A series of samples were prepared with different *pH*s (0, 1, 3, 6, and 8) by varying the amount of *NaOH* in the solution. The mixture was then sealed in a 100 *mL* Teflon-lined stainless autoclave and allowed to heat for 12 *h* at 180 °*C* under autogenous pressure in an oven. The precipitate was filtered, washed three times with distilled water and then with ethanol, and dried at room temperature. Finally, the samples were annealed at 450 °*C* for 2 *h*. The crystalline phases were identified by means of X-ray diffraction (XRD), using an X' Pert Phillips diffractometer, with *Cu Kα* radiation, under the following conditions: 2θ = 5°−60°, 2θ step size = 0.02 at 40 *kV* and 30 *mA*. The UV−vis diffuse reflectance spectra were recorded by a Varian model Cary 500 spectrophotometer with a suitable quartz cell for measuring powders. The Brunauer−Emmett−Teller (BET) specific surface area was measured by means of N_2 sorption at 77 *K* on a Micromeritics Tristar II (surface area and porosity) instrument. The XPS spectra were recorded using a PHI 5000 Versa Probe, with a scanning ESCA microscope fitted with an Al monochromatic X-ray source (1486.6 *eV*, 25.6 *W*), a beam diameter of 100 μm, a neutralizer at 1.4 *eV* and 20 *mA*, and a FAT analyzer mode. All the binding energies were referenced to the *C1s* peak at 284.6 *eV* of the surface carbon. The individual components were obtained by curve fitting. The ethylene photocatalytic degradation was performed in a Pyrex glass reactor. The setup shown in Fig.5.1 includes a Pyrex glass reactor, connectors, mass flow controllers (MFC, Bronkhorst High-Tech), a Scholly Fiberoptic Flexilux 650 Kaltlichtquelle 150 *W* (which is a cold light-emitting visible lamp), gas cylinders (1000 *ppm* ethylene, air), and a gas chromatograph (GC, Varian CP-3800) equipped with a capillary column (CP7381, fused silica) and a flame ionization detector (FID), which was used for the analysis of the gas product.

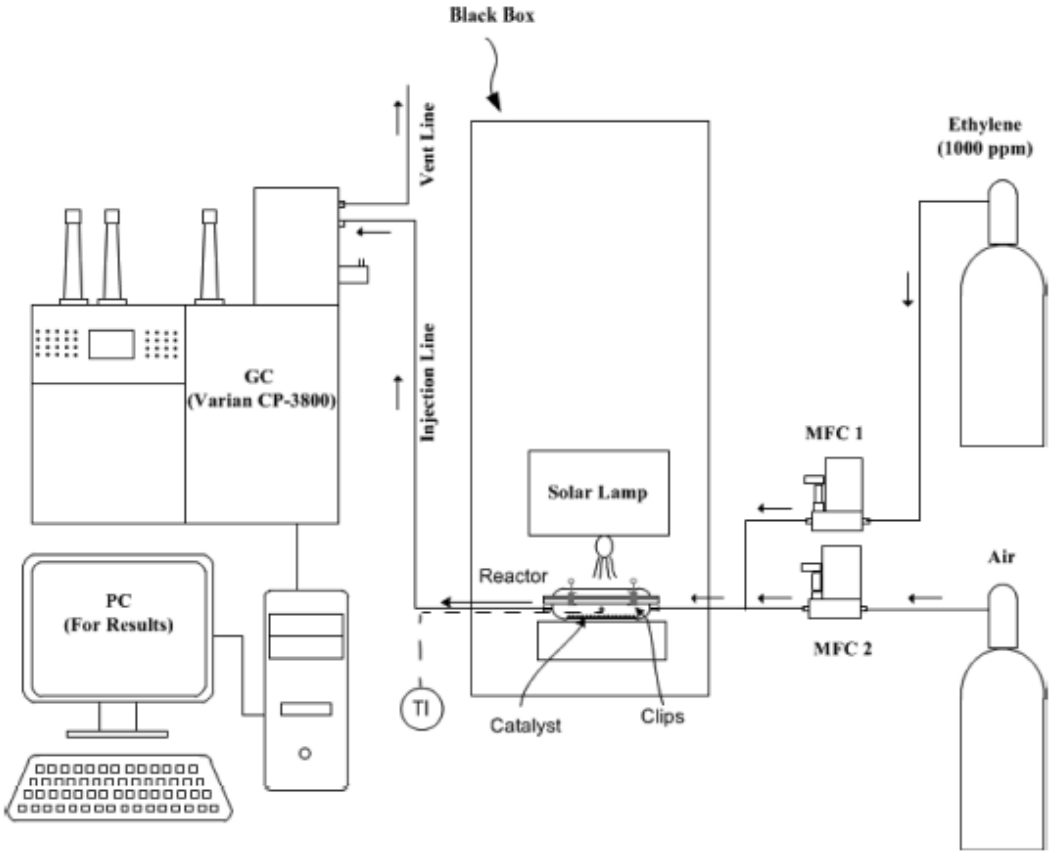

Figure:5.1. Visible-light-driven ethylene photodegradation experimental setup.

A photocatalytic reaction was performed in the reactor, which contained 0.5 *g* of photocatalyst, and 1000 *ppm* of ethylene gas was diluted with air to achieve 100 *ppm*, which was introduced into the reactor at 50 *mL/min* to have an adsorption−desorption balance and to saturate the catalysts with the gas mixture. When equilibrium was reached, the visible light was turned on and the reaction products were analyzed by means of the GC. Blank tests (i.e., visible light without the photocatalyst and a reaction in the dark with the photocatalyst) were also conducted to ensure that the product was actually due to the photocatalytic reaction.

5.3. Results and Discussion

Structural characteristics can be deduced from the comparative XRD patterns. The monoclinic nature of $BiVO_4$ can be confirmed by observing the peak splitting that occurs at 18.5 and 35 of the 2θ values (shown in Fig.5.2a.). No change in the XRD sample patterns, which all belong to the monoclinic family of $BiVO_4$ (X' Pert standard card no. 14-0688, space group *I2/a*, a = 5.195 Å, b = 11.701 Å, c = 5.092 Å, β = 90.38°), was observed at different *pH* values of the suspension mixture. However, the main difference in the observed patterns pertains to the intensity of the {ī21} and {040} peaks. The higher the *pH* during the synthesis, the more intense the {040} peak, compared to the {ī21} peak (see Fig.5.2a), which entails an increase in the fraction of exposed {040} surface. The relative ratio of the {011} or {ī21} to the {040} facets can be correlated to the activity of the sample. Considering the importance of the oxidation {011} and reduction {040} facets,(17) in comparison to the {ī21} plane of the structure, some important clues can be drawn from the pattern with respect to the activity. A change in the *pH* has already been shown to influence the preferential growth of crystallites,(13,18) which is also known to vary with the addition of other structural changing agents. On the basis of our results we conclude that an increase in the *pH* favors the expression of {040} crystal facet only when ammonium carbonate is present.

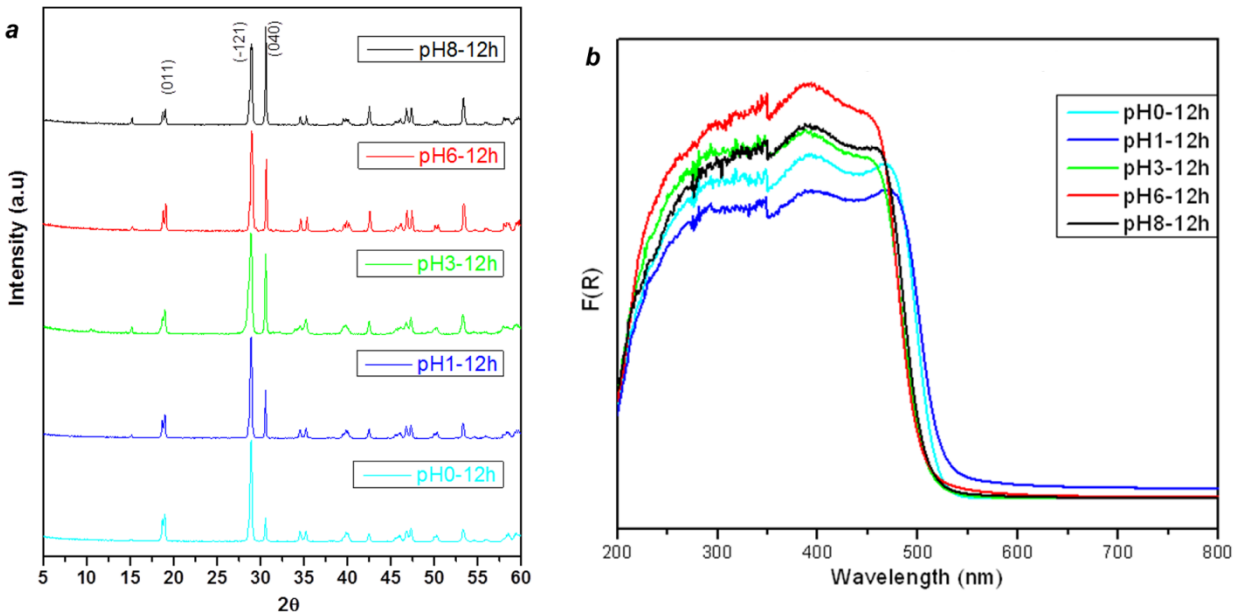

Figure: 5.2 XRD peak variation and the absorbance of as prepared sample at different *pH*.(a) Comparative XRD profile of the samples synthesized at different *pH*. (b) UV-Vis spectra of the samples at different *pH*s.

The band gap of $BiVO_4$, which has been synthesized by varying the *pH* and keeping the other reagents constant, is shown in Fig.5.2*b*. The absorption edge of all the samples lies well within the visible region. However, a small *pH* effect was observed. The average absorption edge of the samples ranges between 510 and 530 *nm*, which corresponds to a band gap of 2.34-2.43 *eV* and is the characteristic band gap of monoclinic $BiVO_4$.(19,20) The variation in the spectra offers information on the variations in the electronic structures of the samples.(19) BET analysis (Table 5.1) showed that all the $BiVO_4$ materials have specifically lower range of surface areas, which are in the gradually increasing trend with the increase of *pH*.

Table 5.1 BET surface areas and band gap energies of the $BiVO_4$ materials synthesized.

pH	BET surface areas (m2/g)	Band gap energies (eV)
0	0.07	2.37
1	0.32	2.34
3	0.55	2.43
6	0.81	2.42
8	1.05	2.43

The morphology of the samples obtained at different *pH* conditions is described in Fig.5.3a-e and varied considerably as the *pH* of the medium was increased. The morphology started as a perfect grain (Fig.5.3a,b) and gradually started to exhibit deformations (Fig.5.3c-e) with an increase in the *pH*, which is linked to the higher exposure of the {040} surface. The morphology of the samples synthesized at *pH* 0 and 1 showed decagonal shapes. The samples at *pH* 3 showed granular agglomerates with nonuniform shapes, whereas the samples at *pH* 6 and 8 showed leaflike structures, which, after calcination, were broken into small, irregular, flakelike structures that showed no change in the XRD pattern. Moreover, $BiVO_4$ synthesized under extremely acidic (*pH* 1) or basic (*pH* 10) conditions should be avoided, as it attributes the weak crystallinity.(21) Therefore, $BiVO_4$ under $pH>8$ was not synthesized and *pH* 8 was considered to be the appropriate optimized *pH*.

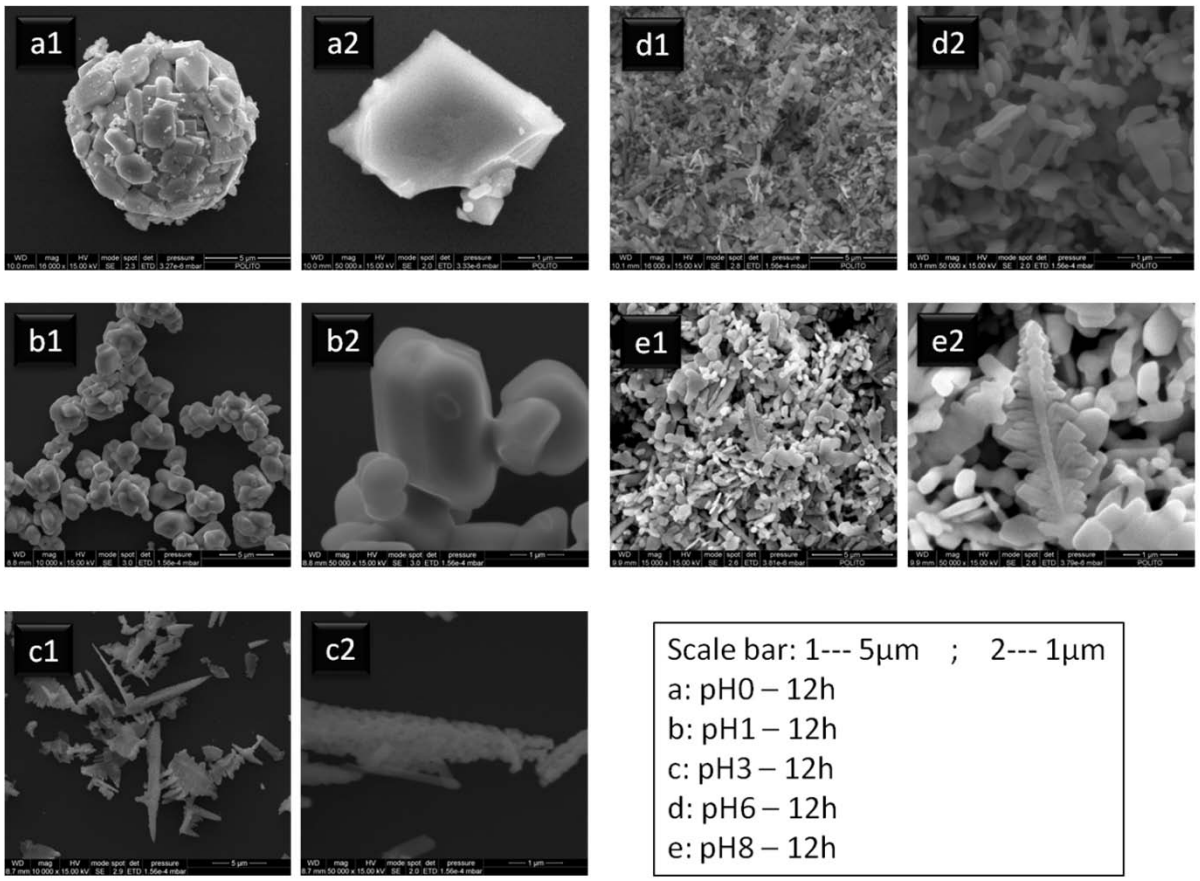

Figure:5.3 Morphological variations of the samples synthesized at different *pH*.SEM analysis of the samples *(a-e)* synthesized at *pH* 0, 1, 3, 6 and 8, respectively. The scale bar refers to 5μm in case 1 and to 1μm in case 2 views.

EDX analysis (Fig.5.4a) confirmed that the materials synthesized were pure $BiVO_4$ without any impurity. It was further confirmed by the XPS analysis, as shown in Figure 4b. XPS analysis was also performed in order to check the surface oxidation state of the samples. Samples synthesized at *pH* 0 and 8 in particular were considered in order to establish the differences in the surface species that were responsible for the photocatalytic activity. The results of the XPS analysis are reported in (Fig.5.5a−f) and show details regarding the $V2p_{3/2}$, *O1s(V−O)*, *OH*, and *Bi4f* species. The *C1s* peak at 284.6 *eV* was used for calibration purposes. The asymmetric signal could be devolved into two peaks (Fig.5.5a,b), indicative of the presence of two $V2p_{3/2}$ states. These have been denoted as V^{4+} and V^{5+} and are seen at 515.26, 516.46 *eV* in the *pH* 0 sample and at 515.26, 516.37 *eV*, in the *pH* 8 sample.22 The percentage of V^{4+} in the *pH* 8 sample is higher than that in the *pH* 0 sample.

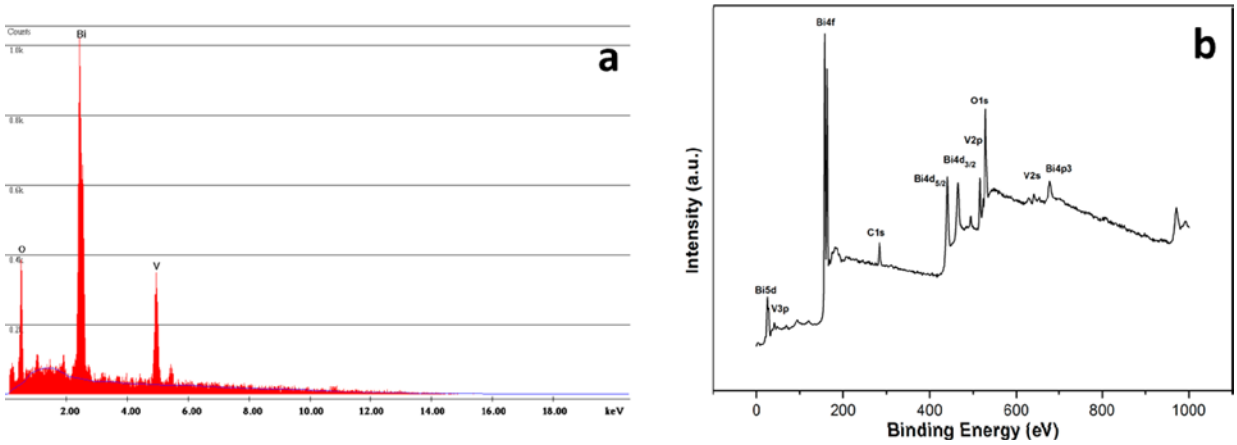

Figure:5.4. EDX and XPS analysis of the optimized $BiVO_4$: (a) EDX and (b) XPS analysis confirmed the elemental composition.

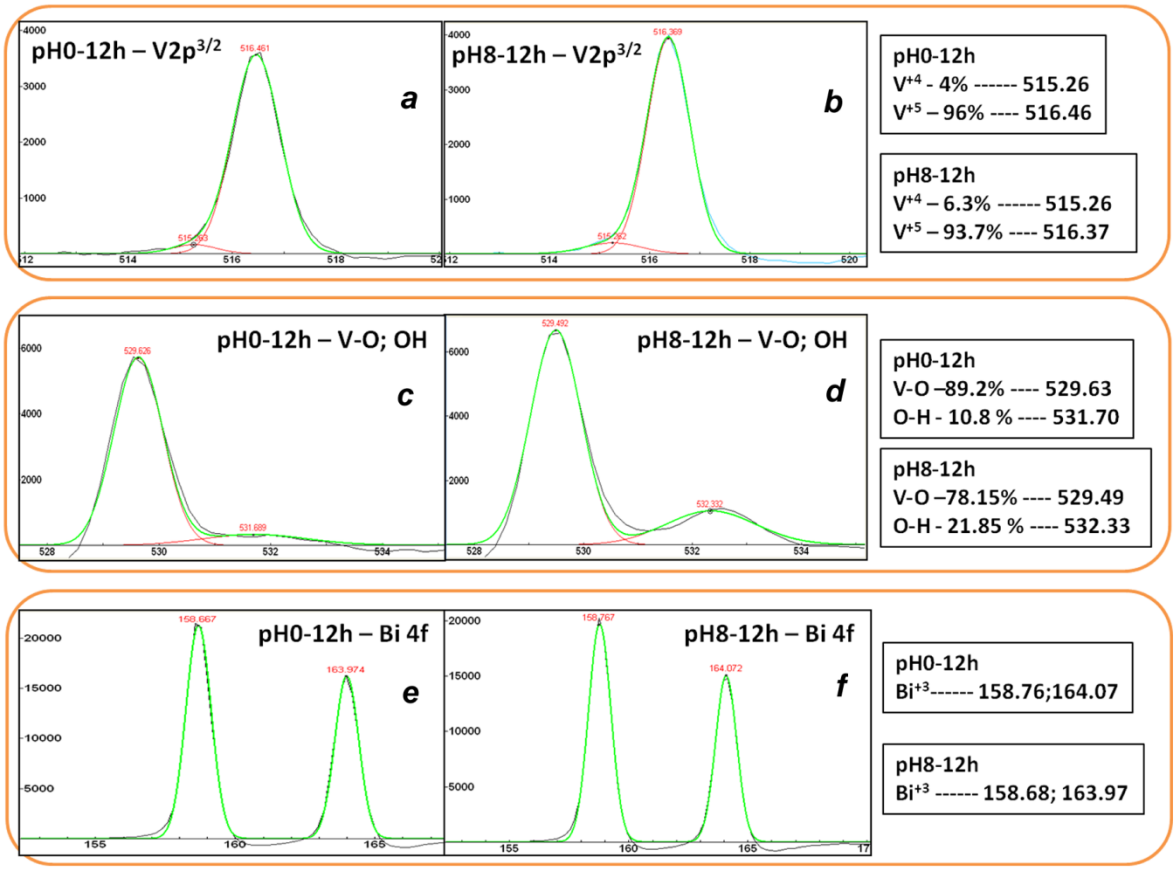

Figure:5.5 Variations of surface states from XPS characterization.De-convoluted XPS spectra of the *V2p3/2* ((a1) and (a2)), *V-O* and *OH* ((b1) and (b2)) and *Bi4f* ((c1) and (c2)) of *pH*0-12 *h* and *pH*8-12 *h*, respectively. The percentage of the individual species and the binding energy values are also shown.

No considerable difference can be observed between the two main asymmetric peaks, $Bi4f_{7/2}$ and $Bi4f_{5/2}$, at 158.76 and 164.7 *eV* in the *pH* 0 sample and at 158.68 and 163.97 *eV* in the *pH* 8 sample20 (Fig.5.5e,f). The very small difference in the binding energy can be attributed to the changes in the electron density of the samples. Thus, a *pH* increase seems to induce a decrease of the electron density over the bismuth present in the samples. The *O1s* asymmetric peak that can be observed in the deconvoluted XPS spectra (Fig.5.5c) indicates

that it was split into a sharp peak at around 529.63 *eV* and a small peak at around 531.70 *eV*. These peaks represent the *V−O* and chemisorbed *O−H* species on the surface of the *pH* 0 sample,(22−24) respectively. The peaks of the *V−O* and *O−H* species for the *pH* 8 sample were observed at 529.49 and 532.33 *eV*, respectively (Fig.5.5d). As the *pH* of the sample increases, a pronounced enhancement in the percentage of the absorbed *O−H* species occurs. This, in turn, makes the adsorption of the reactant (ethylene in the present case, as shown later) more effective as well as that of the precursors for hydroxyl radicals, which are responsible for many photocatalytic oxidations.(6,24) The *pH* of the reaction media during the synthesis has profound effects on the increase in the V^{4+} and the related *O−H* species on the surface of the $BiVO_4$, which in turn is helpful for the photodegradation of ethylene.(7)

Bismuth vanadate applications include potential catalysts for water oxidation(25) and for the degradation of water-soluble organic compounds, such as methyl orange,(16) rodamine B,(26) and methylene blue.(27) However, bismuth vanadate has rarely been studied for the abatement of gaseous phase volatile organic compounds (VOCs)(24,28) in air. VOCs are toxic, and some are considered to be carcinogenic, mutagenic, and/or teratogenic; they are also considered to be some of the most important anthropogenic pollutants generated in urban and industrial areas. Thus, long-term exposure to these VOCs is detrimental to human health (sick building syndrome, SBS).(6) Moreover, VOC emissions can contribute to the formation of urban smog and ozone, stratospheric ozone depletion, and the greenhouse effect. Ethylene is one of the active members of the VOC family, and its oxidative abatement has recently received increasing attention.(6,7) Therefore, there is currently a demand for novel, safe, and clean chemical technologies and processes for VOC abatement. VOC pollutants are traditionally removed through the use of air purifiers that employ sorption materials (e.g., granular activated carbon) to adsorb the VOC molecules.(29) These techniques only transfer the contaminants to another phase instead of destroying them. Hence, additional disposal or handling steps are needed. The photocatalytic oxidation (PCO) of VOCs is a very attractive and promising alternative technology for air purification. TiO_2 is an ideal photocatalyst and has a significant impact on ethylene degradation, but its activity is restricted to UV irradiation.(6,7)

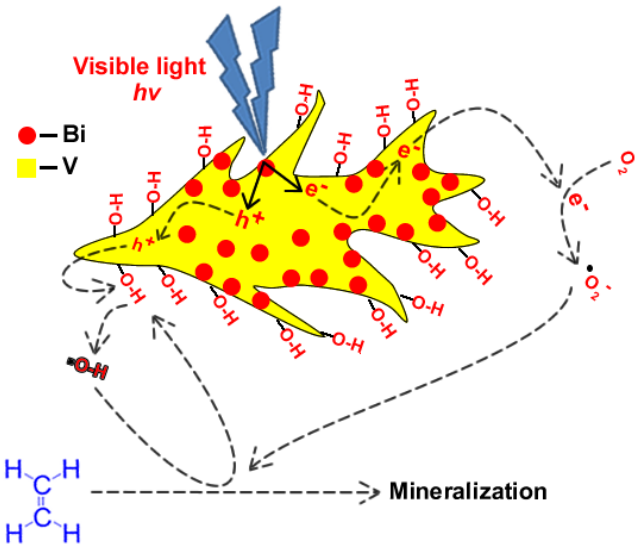

$BiVO_4 + h\nu\ (\text{Visible light}) \rightarrow e^-_{CB} + h^+_{Vb}$ (1)

$h^+_{VB} + OH^-_{(ads)} \rightarrow {}^{\bullet}OH$ (2)

$e^-_{CB} + O_2 \rightarrow {}^{\bullet}O_2^-$ (3)

$\text{Ethylene} + BiVO_4 \rightarrow \text{Ethylene}^*$ (4)

$\text{Ethylene}^* + {}^{\bullet}OH \rightarrow CO_2 + H_2O$ (5)

$\text{Ethylene}^* + {}^{\bullet}O_2^- \rightarrow CO_2 + H_2O$ (6)

Figure: 5.6 Pictographic representation and the possible mechanisms involved in the process.Details of the mechanism involved in the mineralization process of ethylene and the reactions involved are given in equations 5.1-5.6.

Here we have explored the use of visible light for the degradation of ethylene by employing structurally modified $BiVO_4$, which is an efficient, nontoxic, and cost-effective photocatalyst. Visible light excitation of this semiconductor generates energized electrons (e^-) and positively charged holes (h^+) (eq 1 in Fig.5.6). The mechanism involved in the photodegradation of ethylene (Fig.5.6) involves a two-step process. Ethylene is adsorbed on the photocatalyst (eq 4), with the participation of $O-H$ species on the surface. The photogenerated holes then react directly with the $O-H$ species and convert them into $O-H$ radicals (eq 5.2), which play a central role in the degradation of the ethylene (eq 5.5). In addition the photogenerated energized electrons react with O_2 in the incoming air flux, generating $^{\bullet}O^{2-}$ radicals (eq 5.6). The $^{\bullet}O^{2-}$ radicals can react with the moisture available in the influx, thus providing additional $O-H$ radicals.(30) Fig.5.7a shows that, for a constant illumination time, there is a gradual increase in the degradation of ethylene for the samples prepared at higher *pH* values. It has been observed that $BiVO_4$ synthesized at higher *pH* (*pH* 8) also showed comparatively better solar-light-induced ethylene degradation than all other samples reported in this work. As shown by UV-vis spectra (Fig.5.2b) and band gap values (Table 5.1), all $BiVO_4$ materials synthesized have band gap energies in the visible light region (2.34−2.43 *eV*), which have equal effects on the activity. Moreover, BET surface areas (Table 5.1) have an increasing trend with increased *pH* but are in the low range, which might affect the activity but not so significantly. The reaction seems to be structure sensitive and depends strongly on the $BiVO_4$ facets. Therefore, the increased photocatalytic performance is due to its enhanced {040} facets, as was confirmed by the XRD analysis (Fig.5.2a). These {040} facets, as was confirmed by the XPS analysis shown in Fig.5.5, in turn increased the *OH* groups (21.85% with *pH* 8 than 10.8% with *pH* 0) on the surface of $BiVO_4$, which increased ethylene degradation. It has also been explained with the proposed mechanism shown in Fig.5.6. Moreover, the conversion of ethylene reached a plateau due to the maximum activity of the catalyst, which remained constant until the end of the reaction, which showed the stability of the catalyst for this reaction(Fig. 5.7a). It has been further observed that 6 times higher solar-induced photocatalytic activity by the optimized $BiVO_4$ has been measured compared to the best TiO_2 photocatalyst ever produced by our group(6,7) and even 10 times higher than the reference Degussa *P25* titania. Fig.5.7b,c further shows the variations in the activity of the samples and their profiles with preferred peak intensity ratios. Fig 5.7b shows the peak ratios that can be taken into consideration for the analysis, and Fig.5.7c provides information on the individual peak ratios to ethylene conversion, which shows the importance of {040} facets in the activity. The increase of photocatalytic activity of the optimized $BiVO_4$ (*pH* 8) compared to the commercial available Degussa *P25* TiO_2 as well as TiO_2 nanoparticles (TNP) formerly developed at our laboratories(6,7) is striking and a direct consequence of the ability of $BiVO_4$ to exploit a much broader range of radiation wavelengths (Fig.5.2b) than the UV light alone.

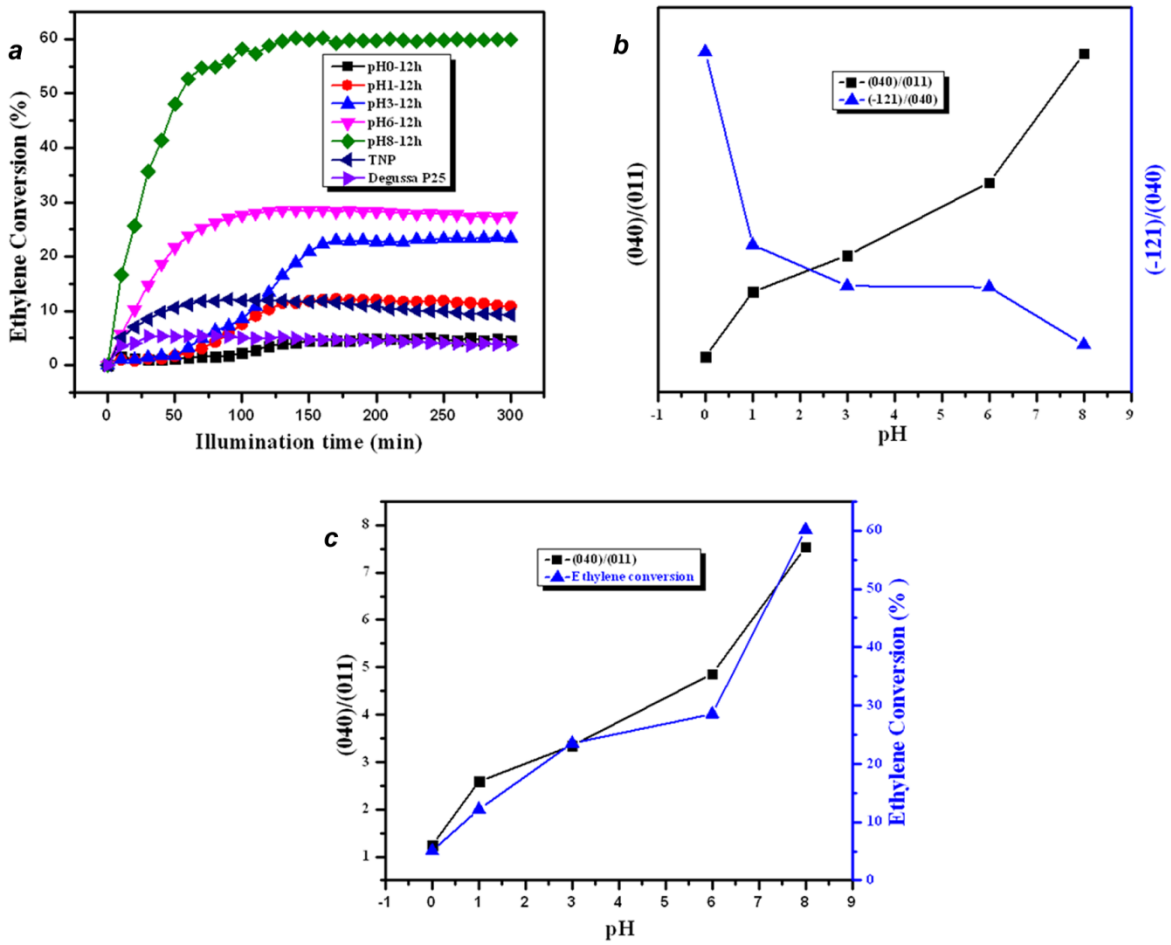

Figure: 5.7.Variations in the activity of the samples and their profiles with preferred peak intensity ratios. (a) Details of ethylene conversion withvisible light illumination time for the different *pH*samples($BiVO_4$) and comparison with TNP and Degussa P25 TiO_2, (b) peak ratios that can be taken into consideration for the analysis, and (c) provides information on the individual peak ratios to ethylene conversion.

5.4.Conclusions

We conclude that the synthesis procedure for $BiVO_4$, reported here at high *pH* in the presence of ammonium carbonate as a structure-directing agent, has a significant influence on increasing the {040} crystallographic facet (result confirmed by means of XRD) and that the increased amount of V^{4+} state (detected by means of XPS) at higher *pH* is responsible for the increase in the $O{-}H$ species on the surface of the catalyst, which boosts ethylene degradation rate by 1 order of magnitude compared to the common TiO_2 photocatalysts.

5.5.References

1. Zhang, H.; Chen, G.; Bahnemann, D. W. Photoelectrocatalytic materials for environmental applications. *J. Mater. Chem.*, 2009, 19, 5089−5121.

2. Kamat, P. V. Photochemistry on nonreactive and reactive (semiconductor) surfaces. *Chem. Rev.*, 1993, 93, 267−300.

3. Yang, H. G.; Sun, C. H.; Qiao, S. Z.; Zou, J.; Liu, G.; Smith, S. C.; Cheng, H. M.; Lu, G. Q. Anatase TiO_2 single crystals with a large percentage of reactive facets. *Nature*, 2008, 453, 638−641.

4. Liu, G.; Yu, J. C.; Lu, G. Q.; Cheng, H.-M. Crystal facet engineering of semiconductor photocatalysts: Motivations, advances and unique properties. *Chem. Commun.*, 2011, 47, 6763−6783.

5. Di Paola, A.; García-Lo´pez, E.; Marcì, G.; Palmisano, L. A survey of photocatalytic materials for environmental remediation. *J. Hazard. Mater.*, 2012, 211−212, 3−29.

6. Hussain, M.; Russo, N.; Saracco, G. Photocatalytic degradation of VOCs by novel otimized TiO_2 nanoparticles. *Chem. Eng. J.*, 2011, 166, 138−149.

7. Hussain, M.; Ceccarelli, R.; Marchisio, D. L.; Fino, D.; Russo, N.; Geobaldo, F. Synthesis, characterization, and photocatalytic application of novel TiO_2 nanoparticles. *Chem. Eng. J.*, 2010, 157, 45−51.

8. Fujishima, A.; Honda, K. Electrochemical photolysis of water at a semiconductor electrode,*Nature*, 1972, 238, 37−38.

9. Cao, S. W.; Yin, Z.; Barber, J.; Boey, F. Y. C.; Loo, S. C. J.; Xue, C. Preparation of Au-$BiVO_4$ heterogeneous nanostructures as highly efficient visible-light photocatalysts. *ACS Appl. Mater. Interfaces*, 2012, 4, 418−423.

10. Xi, L.; Tran, P. D.; Chia, S. Y.; Bassi, P. S.; Mak, W. F.; Mulmudi, H. K.; Batabyal, S. K.; Barber, J.; Loo, J. S. C.; Wong, L. H. Co_3O_4 decorated hematite nanorods as efficient photoanode for solar water oxidation. *J. Phys. Chem. C*, 2012, 116, 13884−13889.

11. Kudo, A. Development of photocatalyst materials for water splitting with the aim at photon energy conversion. *J. Ceram. Soc. Jpn.*, 2001, 109, S81−S88.

12. Zou, Z.; Ye, J.; Sayama, K.; Arakawa, H. Direct splitting of water under visible light irradiation with an oxide semiconductor photocatalyst,*Nature*, 2001, 414, 625−627.

13. Wang, D.; Jiang, H.; Zong, X.; Xu, Q.; Ma, Y.; Li, G.; Li, C. D. Crystal facet dependence of water oxidation on $BiVO_4$ sheets under visible light irradiation,*Chem.Eur. J.*, 2011, 17, 1275−1282.

14. Xi, G.; Ye, J. Synthesis of bismuth vanadate nanoplates with exposed {001} facets and enhanced visible-light photocatalytic properties,*Chem. Commun.*, 2010, 46, 1893−1895.

15. Su, J.; Guo, L.; Yoriya, S.; Grimes, C. A. Aqueous growth of pyramidal-shaped $BiVO_4$ nanowire arrays and structural characterization: Application to photoelectrochemical water splitting,*Cryst. Growth Des.*, 2010, 10, 856−861.

16. Zhang, A.; Zhang, J.; Cui, N.; Tie, X.; An, Y.; Li, L. Effects of *pH* on hydrothermal synthesis and characterization of visible-light-driven $BiVO_4$ photocatalyst, *J. Mol. Catal. A-Chem*, 2009, 304, 28−32.

17. Li, R.; Zhang, F.; Wang, D.; Yang, J.; Li, M.; Zhu, J.; Zhou, X.; Han, H.; Li, C. Spatial separation of photogenerated electrons and holes among {010} and {110} crystal facets of *$BiVO_4$*,*Nat. Commun.*, 2013, 4, 1432.

18. Zhao, Y.; Xie, Y.; Zhu, X.; Yan, S.; Wang, S. Surfactant-free synthesis of hyperbranched monoclinic bismuth vanadate and its applications in photocatalysis, gas sensing, and lithium-ion batteries,*Chem. Eur. J.*, 2008, 14, 1601−1606.

19. Kudo, A.; Omori, K.; Kato, H. A novel aqueous process for preparation of crystal form-controlled and highly crystalline *$BiVO_4$* powder from layered vanadates at room temperature and its photocatalytic and photophysical properties,*J. Am. Chem. Soc.*, 1999, 121, 11459−11467.

20. Yu, J.; Kudo, A. Effects of structural variation on the photocatalytic performance of hydrothermally synthesized *$BiVO_4$*,*Adv. Funct. Mater.*, 2006, 16, 2163−2169.

21. Wan, Y.; Wang, S.; Luo, W.; Zhao, L. Impact of preparative *pH* on the morphology and photocatalytic activity of *$BiVO_4$*,*Int. J. Photoenergy*, 2012, 392865, 1−7.

22. Wang, M.; Liu, Q.; Che, Y.; Zhang, L.; Zhang, D. Characterization and photocatalytic properties of N-doped *$BiVO_4$* synthesized via a sol-gel method,*J. Alloy Compd.*, 2013, 548, 70−76.

23. Long, M.; Cai, W. M.; Cai, J.; Zhou, B. X.; Chai, X. Y.; Wu, Y. H. Efficient photocatalytic degradation of phenol over *Co_3O_4/$BiVO_4$* composite under visible light irradiation,*J. Phys. Chem. B*, 2006, 110, 20211−20216.

24. Huang, C.-M.; Pan, G.-T.; Peng, P.-Y.; Yang, T. C. K. In situ DRIFT study of photocatalytic degradation of gaseous isopropanol over *$BiVO_4$* under indoor illumination,*J. Mol. Catal. A-Chem.*, 2010, 327, 38−44.

25. Park, Y.; McDonald, K. J.; Choi, K. S. Progress in bismuth vanadate photoanodes for use in solar water oxidation,*Chem. Soc. Rev.*, 2013, 42, 2321−2337.

26. Zhang, L.; Chen, D.; Jiao, X. Monoclinic structured *$BiVO_4$* nanosheets: Hydrothermal preparation, formation mechanism, and coloristic and photocatalytic properties,*J. Phys. Chem. B*, 2006, 110, 2668−2673.

27. Jiang, H.-q.; Endo, H.; Natori, H.; Nagai, M.; Kobayashi, K. Fabrication and photoactivities of spherical-shaped *$BiVO_4$* photocatalysts through solution combustion synthesis method,*J. Eur. Ceram. Soc.*, 2008, 28, 2955−2962.

28. Murakami, N.; Takebe, N.; Tsubota, T.; Ohno, T. Improvement of visible light photocatalytic acetaldehyde decomposition of bismuth vanadate/silica nanocomposites by cocatalyst loading,*J. Hazard. Mater.*, 2012, 211, 83−87.

29. Yu, H.; Zhang, K.; Rossi, C. Theoretical study on photocatalytic oxidation of VOCs using nano-TiO_2 photocatalyst,*J. Photochem. Photobiol. A-Chem.*, 2007, 188, 65−73.

30. Nagaveni, K.; Hegde, M. S.; Ravishankar, N.; Subbanna, G. N.; Madras, G. Synthesis and structure of nanocrystalline *TiO_2* with lower band gap showing high photocatalytic activity,*Langmuir*, 2004, 20, 2900−2907.

6. Chapter 6. Doping of $BiVO_4$ Powders Oriented along {040} Facets with Tungston and Molybdenum and Evaluation of their Performance by Photchemical and Photoelctro Chemical Characterizations

6.1. Introduction

Several attempts have been performed in order to obtain optimum crystal structures and morphologies that are capable of enhancing the O_2 evolution activity of $BiVO_4$ powders and photoanodes.(1-5) Obregón *et al.* (2012) prepared *m-*$BiVO_4$ powders with diverse type of morphologies by varying HTS preparation condition, *i.e.* hydrothermal reaction time (2-20*h*) and precipitating agent (NH_4OH and Triehylenamine).(4) Zhao *et al.* (2011) described according to DFT calculations that (100) and (001) facets achieve a higher visible-light absorption as a result of the anisotropy caused by the distortion in *monoclinic* $BiVO_4$ structure. In accordance to this hypothesis, Xi and Ye (2010) synthetized so-called "nanoplates" with highly exposed (004) surface that resulted in a substantial increase of O_2 produced under visible-light illumination utilizing $AgNO_3$ as a an electron scavenger. (1) Similarly, Ressnig *et al.* (2012) produced optimized plate-like particle morphology of *m-*$BiVO_4$ when the HTS conditions were adjusted to *pH*4 and 5*h* at 160 °*C* for 5*h*. This sample yielded a two- and three-fold increase of O_2 evolved compared to *pH*3 and *pH*2 samples. The formation process of these nanoplates was studied by intermediate sampling of the HTS reaction. They found that *z-t* $BiVO_4$ is formed in the first minutes of the synthesis and rapidly disappears as reaction proceeds. Moreover, they inferred that at mild acidic conditions (*pH*>1), when the solubility of tetragonal phase decreases, a quick dissolutionrecrystallization process occurs allowing the formation the plate-like aggregates.(3) No preferential growth of (004) facet was reported in this case.

In a different analysis approach, Wang *et al* (2010) synthesized *m-*$BiVO_4$ powders with increasing (040) facet exposure by a method which combines the addition of a directing agent, *i.e.* $TiCl_3$ and *pH* variation. As a result of (040) diffraction peak increase in XRD patterns they were able to correlate that the increase in the XRD intensity peaks ratio (040)/(010) corresponds to an increase in the O_2 evolution activity. For instance, the oxygen rate in the first hour of illumination increased from about 190 to 300 $\mu mol\ h^{-1}$ when the abovementioned ratio increased from 1 to 12.(5) In a theoretical study about O_2 evolution mechanisms Yang *et al.* (2013) compared these two facet structures finding that there are both advantageous and unfavorable properties of (010) facet over (040) facet. While the later performs worse in photoabsorption, it actually outstands in terms of mobility of charge carriers, water adsorption and lower overall potential-energy surface for O_2evolution.(6)

In order to increase the efficiency of the $BiVO_4$, researches conducted doping in order to improve the charge separation and mobility. Doping, in the field of photocatalysis, is the deliberate introduction of impurity atoms into a semiconductor in order to control the optical and electrical properties of the bulk material.(7) When introducing a transition-metal cation (d_n orbital; $0<n<10$) or an anion for metal-oxides doping, a donor or acceptor level is formed within the forbidden band, respectively;(8) on the other hand, dopants might hinder photocatalytic activity by generating vacancies which act as recombination centers of electrons

and holes due to the formation of a discrete energy level instead of an energy band (7, 8) According to Parmar *et al*. (2012) no discrete energy levels are introduced when *Mo* and *W* are used as dopants of $BiVO_4$.(9) Similarly, Park *et al.* (2011) came to the conclusion by means of DFT calculations that Cr^{5+} (in the same group as *W* and *Mo*) does introduce a localized impurity state within the gap that acts as a recombination center, due to its lower *d*-orbital energy level as compared to the ones of *Cr 3d<Mo 4d~V 3d<W 5d*, trend that is consistent with their own experiments.(10, 11)

Parmar *et al.* (2012) investigated the effect of different metal-cation (*M*) doping elements (*M*=5% atom) on $BiVO_4$. The measured O_2 evolution activity of prepared powders with Ag^+ as electron acceptor reveled that only *Mo* and *W*, among 12 metal species, were able to significantly improve the visible-light water oxidation compared to bare $BiVO_4$. Similarly, photoanodes prepared via MOD/spin-coating (*M*=2% atom.) showed between 5 and 6 times increase of the PEC activity at 1.23 *V* vs RHE. They estimated that the photoanode resistance (RCT), according to the Randles-Ershler circuit model,(12) is several times lower with *W* and *Mo* doping showing a more efficient charge carrier transfer in the photoanode/electrolyte interface. Moreover, the flat band potential calculated from Mottky-Schott (*M-S*) plot *x*-intercept was shifted about 30 mV (vs. *Ag/AgCl*) in the positive direction, which is opposite to the expected effect, as explained above. Finally, the carrier density from *M-S* plot slopes, effectively show about 1.6 and 2 times higher carrier concentrations for *W* and *Mo*-doped $BiVO_4$, respectively. The higher carrier density for *Mo* compared to *W* dopant is in agreement with DFT calculations which show a more significant orbital overlapping and effective hybridization of Mo^{6+} and V^{5+} states, in respect of *W* CB overlapping effect.(9)

In the present paper we successfully synthesized the $BiVO_4$ powders with preferential orientation along the (040) crystal planes and then we employed the same procedure for synthesizing the doped $BiVO_4$ powders with Tungsten and Molybdenum. We studied the properties of the doped $BiVO_4$ powders as such for the photocatalytic oxygen evolution and insights about the rate was given. Then we employed doctorblade procedure for synthesizing the electrodes and the same were employed for electrochemical characterization of the samples.

6.2.Mateials and Methods

6.2.1. Synthesis of $BiVO_4$ Meterial

The $BiVO_4$ powder was synthetized using Bismuth nitratepentahydrate $(Bi(NO_3)_3{\bullet}5H_2O)$, ammonium metavanadate (NH_4VO_3) and ammonium carbonate$((NH_4)2CO_3)$ from Sigma Aldrich. All of them with an analytical grade as well as the otherchemicals used in the experiments. Deionized water was used for the preparation of solutions.The $BiVO_4$ powder was prepared by hydrothermal synthesis (HTS) using 1:16 *g* of ammoniumcarbonate, 1:81g of $Bi(NO_3)_35H_2O$ and 0:439*g* of NH_4VO_3 and dissolving in that orderin 75*mL* of 1$MHNO_3$ and stirred at room temperature until a clear solution was obtained. The*pH* of the mixture was adjusted until 8 using *NaOH* according to the reaction condition. Themixture was then sealed in a 100*mL*Teflon lined stainless auto-clave and subjected to heat foreither 14 *h* at 180 °*C* under autogenous pressure in an oven. The precipitate was centrifuged,filtrated and washed two times with distilled water and one with ethanol, then was dried at roomtemperature, open to the air. Finally, the sample was annealed at 450 °*C* for 2 *h*.

6.2.2. Synthesis of $BiVO_4Mo$-Doped Powders

Were prepared two samples of *Mo*-doped powders by hydrothermal synthesis (HTS), maintaining constant 1:16g of ammonium carbonate and 1:81g of $Bi(NO_3)_3.5H_2O$ and reducing for each sample the quantity of NH_4VO_3 at 0:43362g and 0:4161g and adding 0:00438g and 0:0219g of ammonium molybdate $((NH_4)_2MoO_4)$ respectively to obtain a series of samples at different percentage by weight of the dopant agent (1 and 5wt). The reagents were dissolved in that order in 75mL of 1M HNO_3solution at constant stirring at room temperature until a clear solution was obtained. The pH of the mixture was adjusted until 8 using $NaOH$ according to the reaction condition. The mixture was then sealed in a 100mL Teflonlined stainless auto-clave and subjected to heat for either 14h at 180°C under autogenous pressure in an oven. The precipitate was centrifuged, filtrated and washed two times with distilled water and one with ethanol, then was dried at room temperature. Finally, the sample was annealed at 450 °C for 2 h.

6.2.3. Synthesis of $BiVO_4W$-Doped Powders

Were prepared two samples of *W*-doped powders by hydrothermal synthesis (HTS), maintaining constant 1:16g of ammonium carbonate and 1:81g of $Bi(NO_3)_3.5H_2O$ and reducing for each sample the quantity of NH_4VO_3 at 0:43362g and 0:4161g and adding 0:00438g and 0:0219g of ammonium tungstate$((NH_4)10H_2(W_2O_7)_6)$ respectively to obtain a series of samples at different percentage by weight of the dopant agent (1 and 5wt). The reagents were dissolved in that order in 75mL of 1$MHNO_3$solution at constant stirring at room temperature until a clear solution was obtained. The pH of the mixture was adjusted until 8 with $NaOH$ according to the reaction condition. The mixture was then sealed in a 100mL Teflonlined stainless auto-clave and subjected to heat for either 14 h at 180 °C under autogenous pressure in an oven. The precipitate was centrifuged, filtrated and washed two times with distilled water and one with ethanol, then was dried at room temperature. Finally, the sample was annealed at 450 °C for 2 h.

6.2.4. Synthesis of $BiVO_4$ Electrodes

Finally, the sample was annealed at 450 °C for 2 h. In order to continue with the next step of this research, electrodes were made for photochemical water splitting using conventional slurry (CS) method for the preparation of the films and a technique called doctor blade for the deposition of the slurry in the electrode. Initially were prepared two different slurries one using a proportion catalyst-solution 1:2wt and the other using a proportion 1:4wt catalyst- solution respectively. For the preparation of the slurry with proportion 1:2wt, 89:8ml of acetic acid (H_3COOH), 898:32ml of water and 1827:7ml of ethanol where added to 0:591g of catalyst an put for two hours at ultrasonic agitation promoting the formation of the slurry. Similarly, for the preparation of the slurry with proportion 1:4wt, 91:85ml of acetic acid , 918:5ml of water and 1869ml of ethanol where added to 0:604g of catalyst, then the slurry was leaved for two hours at ultrasonic agitation. After the agitation and using electrodes perfectly cleaned with a piranha solution, the slurries were deposited in the electrodes using the doctor blade technique, which consist in use a glass rod to spread the slurry in the FTO conducting glass (electrode) until form a uniform film. In order to prevent an spreading of the slurry in all the electrode, it was covered first with a plastic mask.

The powder used to make the slurry was the $BiVO_4$ powder prepared by hydrothermal synthesis (HTS), under hydrothermal conditions for 14*h* at *pH* 8. Initially were prepared five electrodes using the doctor blade technique, three of them was prepared with the 1:2*wt* slurry and other two using the 1:4*wt* slurry. The three electrodes prepared with the 1:2*wt* slurry had the following heat treatment; 500°*C* for 2*h*, 500°*C* for 6*h* and 600°*C* for 2*h* respectively. The other two electrodes were annealed one at 500°*C* for 2*h* and 600°*C* for 2*h* respectively. The$BiVO_4$ electrodes prepared with the 1:2*w*t slurry, will hereafter be referred to as A500x2*h*, A500x6*h* and A600x2*h*, where *A* corresponds to the 1:2 catalyst-solution proportion, the values after *A* corresponds to the annealed temperature and the values after x refers to the annealed time. Similarly, for $BiVO_4$ electrodes prepared with the 1:4*wt* slurry, will hereafter be referred to as B500x2*h* and B600x2*h*, where *B*corresponds to the 1:4 catalyst-solution proportion and the other values to the temperature and time of calcination treatment respectively.

The heat treatment studies were made with the purpose of study morphology changes in the samples and thus evaluate how these changes may affect performance in the photo-electrochemical test. Also were made to establish an optimal condition to produce the $BiVO_4$ electrodes and thus in this way apply for the fabrication of doped electrodes using the most active powder previously synthetized and studied.

6.3. Results and Discussion

6.3.1. Characterization of $BiVO_4$ Powder Samples

Characterization of the $BiVO_4$ doped and undoped powders were carried out using various analytical techniques. The characterization techniques used will be presented below with a brief explanation. X-ray diffraction (XRD) patterns were obtained using an X'Pert Phillips diffractometer equipped with an X-ray source of *Cu Kα* radiation (*l* = 0:15418nm) at 40*kV* and 30*mA*. The patterns were recorded in the range of 5-60° at a step size of 0.02°. Crystallite sizes and lattice strain parameters for $BiVO_4$ catalysts were estimated from the line broadening of (121) X-ray diffraction peaks by using the X'Pert HighScore Plus software. The average particle size, estimated from the XRD peaks using the Scherrer equation.(13)

$$D = \frac{K\lambda}{\beta \cos \theta} \qquad Eq \rightarrow 6.1$$

Where *k* is the shape factor (0:9), *l* is the wavelength (0:15418*nm*), *b* is the peak width at half-maximum height (FWHM) in radians of a selected diffraction peak and *q* is the diffraction angle.

UV-Vis diffuse reflectance spectra were obtained on a UV-Vis Varian's Cary 5000 spectrophotometer using a quartz cell suitable for powders measurements. The band gap energies(E_g) for the different samples were calculated by plotting the values of $(\alpha h\nu)^n$ vs the photon energy $(h\nu)$, where α is the absorption coefficient, *h* is the Plank constant and *v* the frequency of vibration. The value of *n* in the relation depends on the type of transitions involved, *n*=2 for a direct transition and *n*=½ for an indirect transition.(14) The relation between the absorption coefficient and the reflectance of the sample is calculated from the Kubelka – Munk function.(15)

$$F(R) = \frac{(1-R)^n}{2R} = \frac{\alpha}{S} \quad Eq\rightarrow \qquad 6.2$$

Where *F(R)* for the Kubelka-Munk function, *R* is the absolute reflectance, α for the absorption coefficient and *S* for the scattering coefficient. The band gap values were estimated from a plot of$[f(R).h\nu]^n$ vs $h\nu$.

The morphology of the $BiVO_4$ samples was investigated by scanning electron microscopy (SEM) using a SEM FEI Quanta Inspect 20.

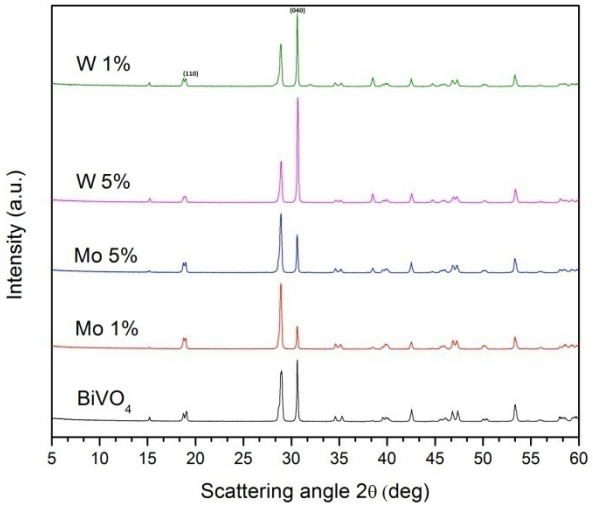

Figure: 6.1. XRD patterns of the $BiVO_4$ and Mo^{6+} doped samples synthesizedunder hydrothermal conditions for 12*h* at *pH* 8.

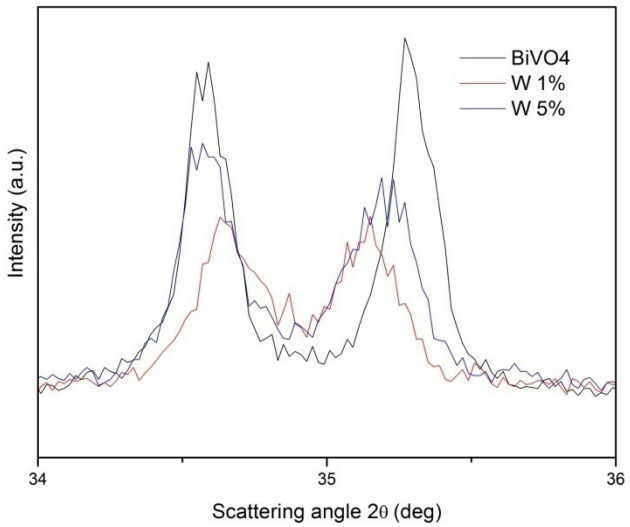

Figure: 6.2. XRD patterns of the $BiVO_4$ and W^{6+} doped samples synthesized under hydrothermal conditions for 12*h* at *pH* 8.

Monoclinic and traces of tetragonal form were of $BiVO_4$ was obtained using hydrothermal synthesis (HTS) method as described in the section above. The fig.6.1 contains the powder XRD patterns forW^{6+} or Mo^{6+}-doped $BiVO_4$ compared with the undoped $BiVO_4$ powder; all of these samples exhibit in most an scheelite monoclinic (*s-m*) phase as their

diffraction peaks are in good agreement with the standard Joint Committee on Powder Diffraction Standards (the JCPDS) card No. 14-0688 (space group: *I2/a*, *a*=5:195, *b*=11:701, *c*=5:092, *b* =90:38°).The fig.6.2 and the fig.6.3 show a shift in both W^{6+} or Mo^{6+}-doped $BiVO_4$ powder samples. This shift represents an enlargement of the *d*-spacing of corresponding crystal planes due to the incorporation of the cations W^{6+} and Mo^{6+}. Because of this incorporation can be hypothesize that W^{6+} or Mo^{6+} impurities were incorporated in the $BiVO_4$ lattice.

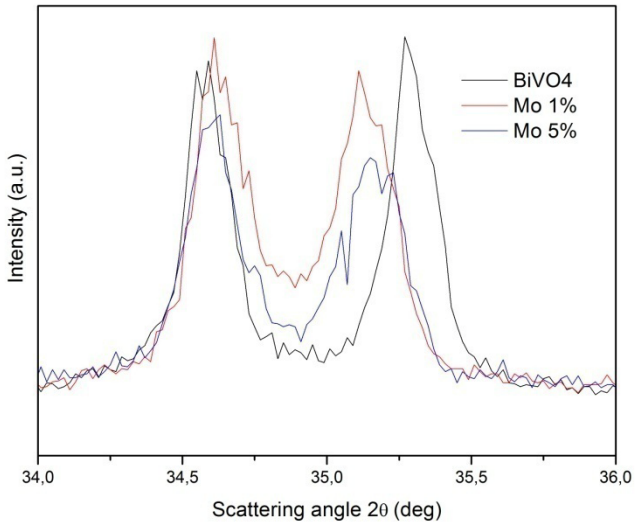

Figure: 6.3. XRD patterns of the $BiVO_4$ and Mo^{6+} doped samples synthesized under hydrothermal conditions for 12*h* at *pH* 8.

In the other hand fig.6.4 and fig.6.5 contains the Tauc plots constructed from the UV visible diffuse reflectance data for the four doping W^{6+}- or Mo^{6+} doping samples as well as for the undoped $BiVO_4$. The band gap energies (E_g) for the various samples were calculated by plotting the values of $(\alpha h\nu)^n$ vs the photon energy $(h\nu)$, (14, 15) where α is the absorption coefficient. The band gap values were estimated from a plot of $[f(R).h\nu]^n$ vs $h\nu$. For a direct band semiconductor, the Tauc region, just above the optical absorbance edge, shows a linear trend with n= ½, as it has been reported for monoclinic $BiVO_4$(16).The extrapolation of this line to the $h\nu$ axis yields the semiconductor band gap.The band gap energies that were found presented a range from 2.56*eV* to 2.58*eV* for the Mo^{6+} doped powders and a range from 2.49*eV* to 2.52*eV* for the W^{6+} doped sample and a minimum value of 2.45*eV* for the undoped $BiVO_4$ sample.The high values of band gap obtained suggest a presence of the tetragonal $BiVO_4$. Some studies suggest that the tetragonal $BiVO_4$ has a much larger band gaps value 2.9*eV*.(17) Even if the samples are in the most monoclinic $BiVO_4$ the band gaps values varies from 2.4 to 2.8*eV*, this variation depends of the mode of synthesis and is supported in the literature data as well.(17, 18, 19)

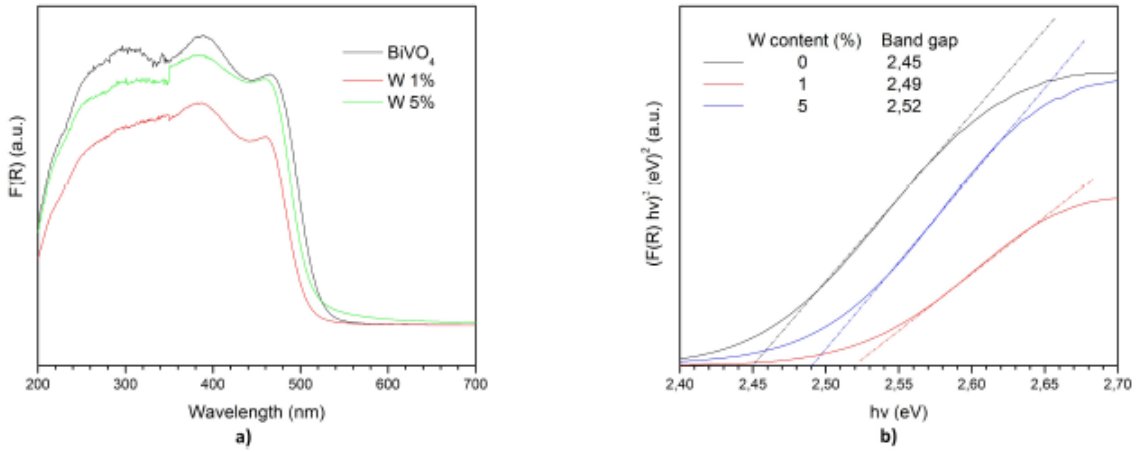

Figure: 6.4. UV–Vis diffuse reflectance spectra ofW^{+6} doped samples and undoped $BiVO_4$ sample synthesized under hydrothermal conditions for 14*h* at *pH* 8 a) and corresponding Tauc plots showing the variation on the band gap energy of the samples b)

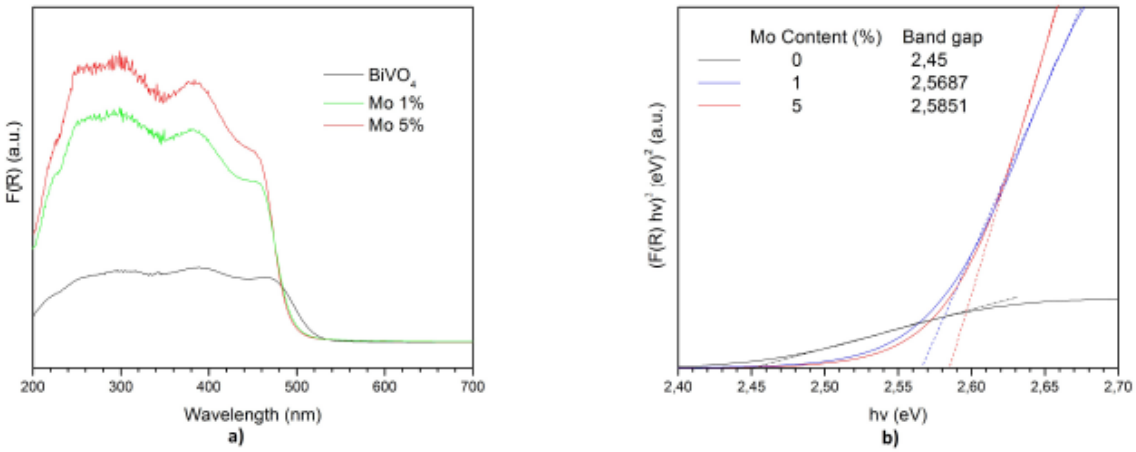

Figure: 6.5. UV–Vis diffuse reflectance spectra of Mo^{6+} doped samples and undoped $BiVO_4$ sample synthesized under hydrothermal conditions for 14*h* at *pH* 8 a) and corresponding Tauc plots showing the variation on the band gap energy of the samples b)

Finally, SEM images for the $BiVO_4$ doped and undoped samples prepared under hydrothermal conditions for 14*h* at *pH* 8 were additionally acquired and compared in Fig.6.6. The $BiVO_4$ sample and the Mo^{6+} doped samples fig.6.6 a, b and c presented crystals with similar morphology like aggregates of elongated crystals suggesting (nano rods) monoclinic phase. In accord with their typical monoclinic

XRD patterns, this well-crystallized grains presented similar crystal sizes (~ 850*Å*) estimated with the Scherrer equation 6.1. On the other hand, theW^{6+}- doped samples presented morphology with a higher hierarchy level of organization like show the fig.6.6 d and e. The *W* 1*wt* sample presented the lower value of crystal size (770*Å*) and the *W* 5*wt* sample the higher (925*Å*), that suggest that the*W* 5*wt* sample evolved into a highly ramified "leaf-like" structure with apparent increase in length and flatness of the "leaves", while the *W* 1*wt* sample remained with a highly ramified 'leave like" but without an increase in its length and preserving the thickness.

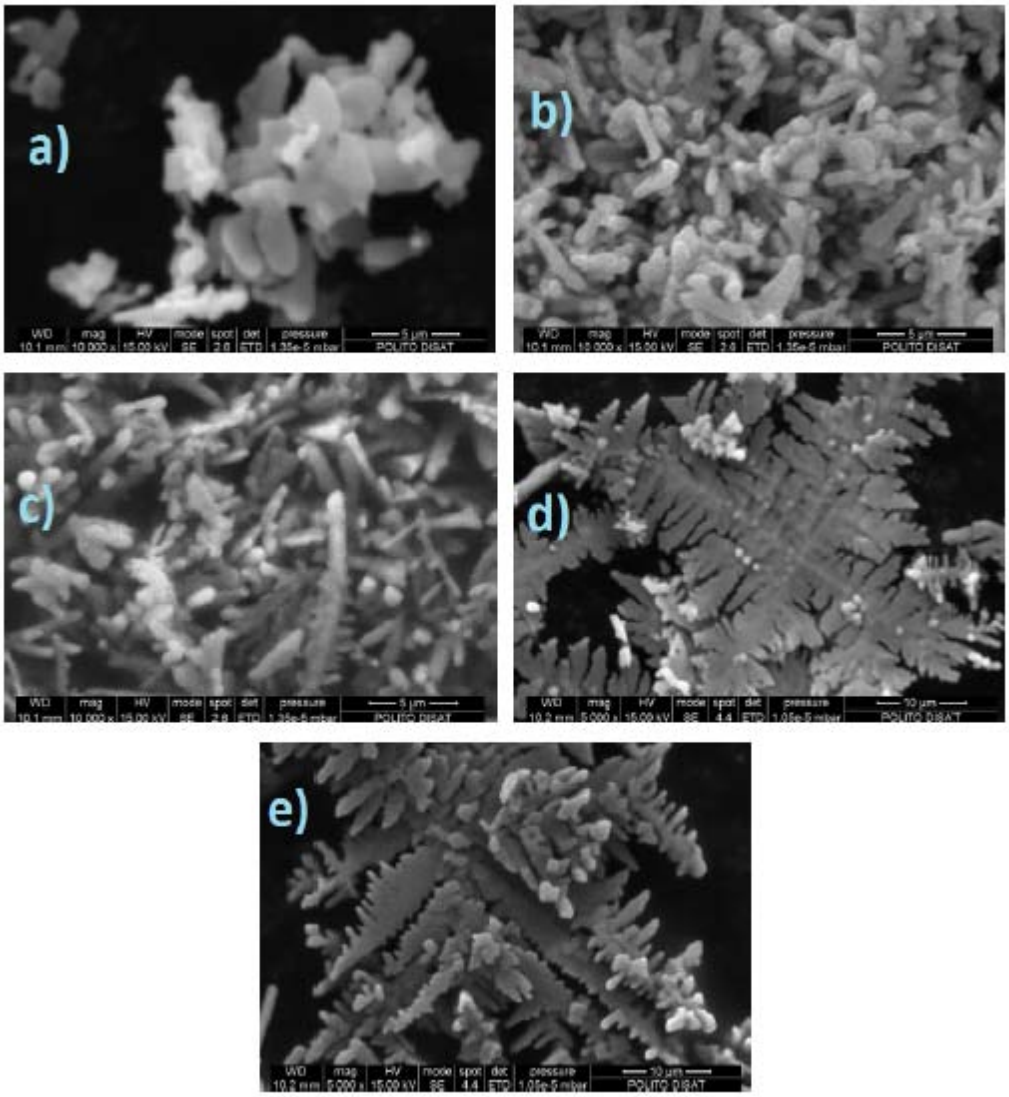

Figure: 6.6. SEM images of $BiVO_4$, W^{6+} and Mo^{6+} Doped samples synthesized under hydrothermal conditions for 12*h* at *pH* 8, values: a) $BiVO_4$; b)*Mo1wt*; c) *Mo3wt* , d)*W 1wt* and e)*W 5wt*

6.3.2. Photocatalytic activity and correlations with other characterizations of$BiVO_4$Powder Samples

The most relevant study in this work was to determine the photocatalytic O_2 evolution of the $BiVO_4$ sample and the Mo^{6+} and W^{6+} doped samples. The experiment was conducted in a pyrex reactor. In this reactor 0.0934*g* of the sacrificial reagent $(AgNO_3)$ which is necessary to promote the conditions for O_2 evolution in the system, were diluted in 11*ml* of bi-distillate water, then the oxygen evolution started with the addition of 0;01*g* of catalyst and leaving the system open for an hour to the simulated irradiation at $100mW.cm^{-2}$ provided by the plasma lamp (Solaronix model LIFI STA-40). The cumulative O_2 evolution was measured with a Clark-type electrode and collected using the software LabVIEW® platform. The fig.6.7 show the pyrex reactor, the clark electrode and the solar simulator lamp used in the experiments.The highest amount of oxygen produced in the experiment was $173\mu mol.g^{-1}cat.h^{-1}$, andcorresponded to the*Mo*1*wt*sample, while the values of cumulative O_2 evolution (R_{O2max}) for thesamples *Mo*5*wt*,*W*1*wt* and*W*5*wt* were 143, 87 and $71\mu mol.g^{-1}cat.h^{-1}$ respectively.

Moreover,the undoped sample presented a value of cumulative O_2 evolution of 30$\mu mol.g^{-1}cat.h^{-1}$. Asexpected the undoped sample presented the minimum value of amount of oxygen produced,demonstrating the positive doping effect in the increase of the photocatalytic activity for the$BiVO_4$, reaching an increase of theO_2 produced of~6 times with the *Mo*1*wt* sample. Therespective plot for the cumulative O_2 evolution vs the irradiation time for all the samples isshow in fig.6.2.

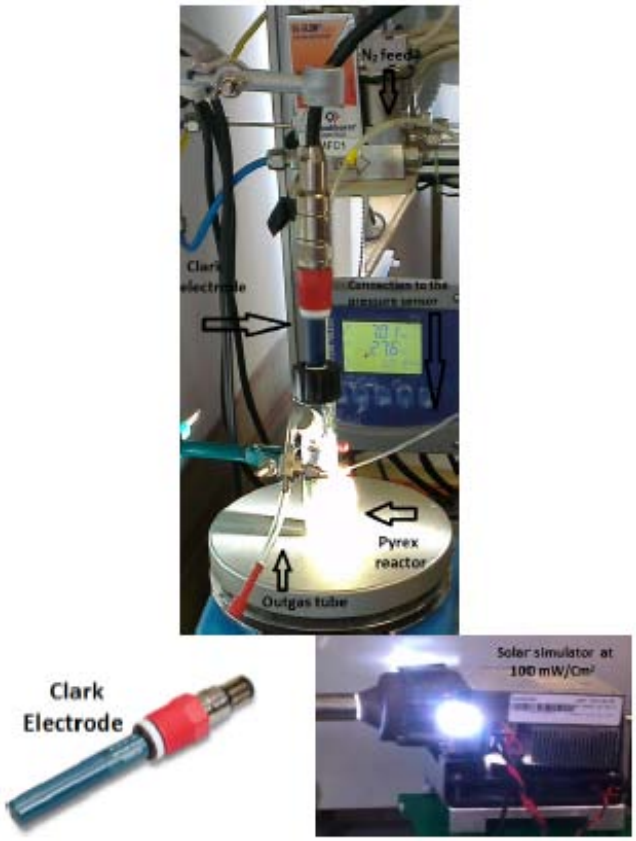

Figure: 6.7. Photocatalytic reactor for the O_2 evolution test a), Clark electrode b) and Solar simulator lamp c)

Otherwise, the fig.6.8 shows that over approximately 20*min* was created a gradual decline in the photo activity. This reduction is due at the interaction between the $BiVO_4$ surfaceand the reacting Ag^+ centers, in the experiment the $BiVO_4$ is covered with photodeposited Ag^+ clusters occupying in this way active sites of the $BiVO_4$ and forcing its deactivation which leads a reduction in the photocatalytic activity. However, the system works well and provided a good estimation of the photocatalytic activity of the powders in the time.

The fig.6.9 shows the initial production rate of O_2 (r_{O2}) for the Mo^{6+} or W^{6+}– doped samples and for the undoped $BiVO_4$ sample. These velocities were estimates making a linear regression in the first minutes of the experiment. It was possible because of the linear tendencies of the samples. In the fig.6.9, again the undoped sample presented the lower value with an initial production rate of 0:17$umol.g^{-1}$ $cat.min^{-1}$, the *Mo*5*wt* and the *Mo*1*wt* doped samples presented the higher values 17:6 and 14:1 $\mu mol.g^{-1}cat.min^{-1}$respectively and the W^{6+} doped samples presented a slight difference in the values with 10.7 and 11.4 $\mu mol.g^{-1}cat.min^{-1}$ for the *W*1*wt* and *W*5*wt* doped samples respectively. The fig.6.10 shows a comparison between the initial production rate of O_2 (r_{O2}) and the cumulative O_2 evolution (R_{O2max}) for the five samples. in this graph can be seen that the *Mo*5*wt* doped samples presented a higher initial

production rate of O_2 (r_{O2}), being bigger for the Mo^{6+}-doped sample, this results suggested that the increase in the content of dopant positively affects the initial production rate of O_2, but increases to the deactivation provided by the Ag^+, resulting in lower values of cumulative O_2 evolution like show the fig.6.8.

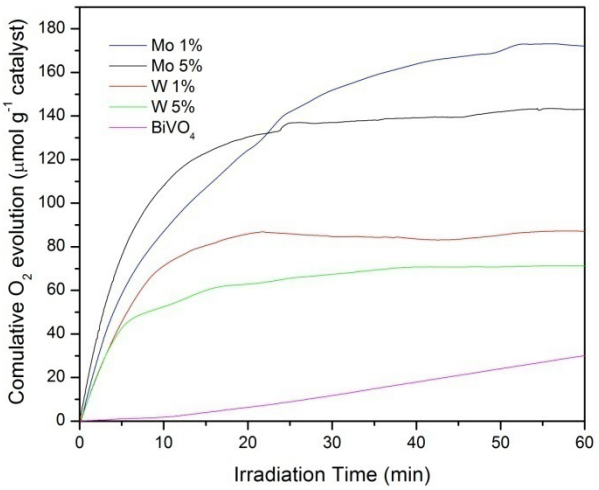

Figure: 6.8. Photocatalytic activities for the Mo^{6+}, W^{6+} doped powders and for the undoped $BiVO_4$ powder, made with the Clark-type electrode.

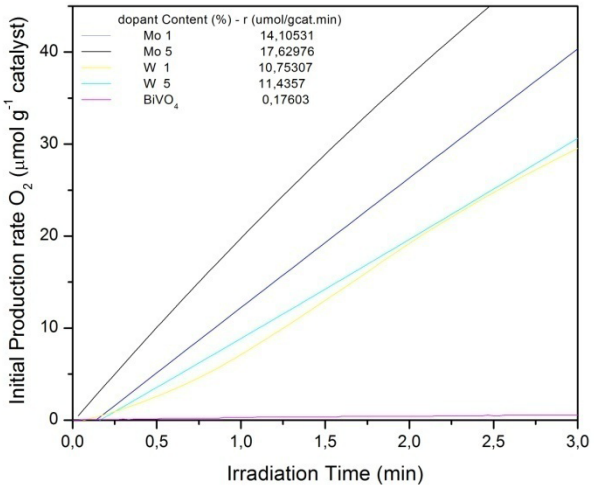

Figure: 6.9. Initial production rates r_{O2} for the Mo^{6+} andW^{6+} doped powders and for the undoped $BiVO_4$ powder.

In order to understand the results obtained in the O_2 evolution test for the $BiVO_4$ doped and undoped samples studied in the pyrex reactor, a summary of the physical properties, optical properties and the photocatalytic O_2 evolution results are shown in table 6.1 . The crystallite sizes were calculated with the Scherrer equation 6.1, and the relative intensities between (040) and (010) facets were estimated applying the corresponding XRD peak intensity ratios. In table 6.1 can be seen small difference in the Mo^{6+}-doped crystallite sizes, similar to the small difference presented in the peak intensity ratio (040)/(110), otherwise the

W^{6+}-doped samples show a notorious difference in the crystal sizes but the peak intensity ratio (040)/(110) remains invariable like the photocatalytic activity. The Mo^{6+}-doped samples were the most actives and presented lower values for the peak intensity ratio (040)/(110) , while the undoped sample presented the higher value in the peak intensity ratio (040)/(110) and the lower photocatalytic activity. This results suggested that the crystallite sizes not provided a good information for the photocatalytic behavior of the powder, but the photocatalytic behavior of the powders could be predicted by the peak intensity ratio (040)/(110) determined in the XRD patterns.

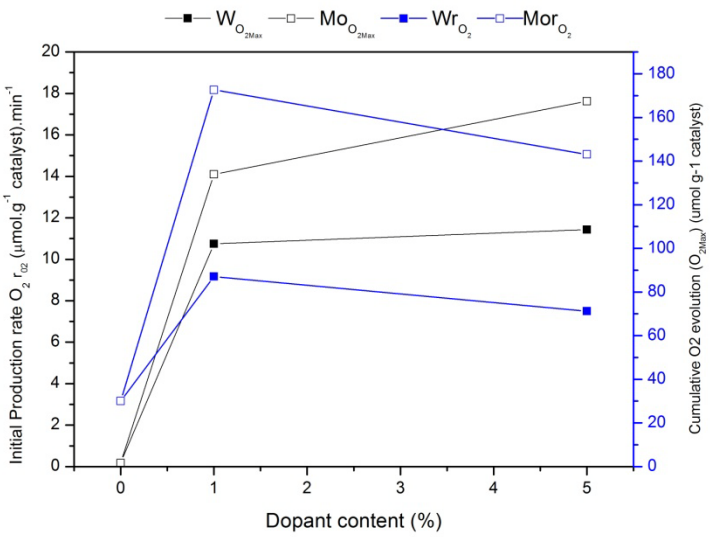

Figure: 6.10. Comparison between the cumulative O_2 evolution (R_{O2max}) andthe initial production rate of O_2 (r_{O2}) for Mo^{6+} andW^{6+} doped powders and theundoped $BiVO_4$ sample.

Table: 6.1. physical properties, optical properties and the photocatalytic O_2 evolution of the doped and undoped $BiVO_4$ samples

Sample	Crystallite size [Å]	Peak intensity Ratio (040)/(110)	Band Gap (E_g) [eV]	Cumulative O_2 evoltution (R_{O_2max}) [$\mu mol \cdot g_{cat}^{-1}$]	Initial Production rate of O_2 (r_{O_2}) [$\mu mol \cdot g_{cat}^{-1} \cdot min^{-1}$]
undoped $BiVO_4$	867	19.6	2.45	30	0.17
$Mo1wt$	884	2.5	2.56	173	14.1
$Mo5wt$	832	4.2	2.58	143	17.6
$W1wt$	770	10.3	2.49	87	10.7
$W5wt$	925	10.6	2.52	71	11.4

The difference in the optical properties presented in the five samples has mentioned in the characterization section, suggest the presence of the tetragonal $BiVO_4$. In the Mo^{6+}-doped sample the values of E_g were the highest, but these samples presented the highest values in the cumulative O_2 evolution, otherwise theW^{6+}-doped samples presented lower values of E_g but lower values of cumulative O_2 evolution. Clearly the Mo^{6+} is better thanW^{6+} for the doping of $BiVO_4$ valuated of the point of the photocatalytic activity, in table 6.1 for the Mo^{6+}-doped samples the $Mo1wt$ sample presented the lower value of E_g confronted with the $Mo5wt$ sample, the same situation was found for theW^{6+}-doped samples, moreover the $Mo1wt$ samples were

the most active samples, presenting the highest values for the cumulative O_2 evolution, which gives importance at the optical properties suggesting that for improve the powders is necessary synthetize monoclinic $BiVO_4$ which provide lower E_g values and possibly a higher photocatalytic activity .

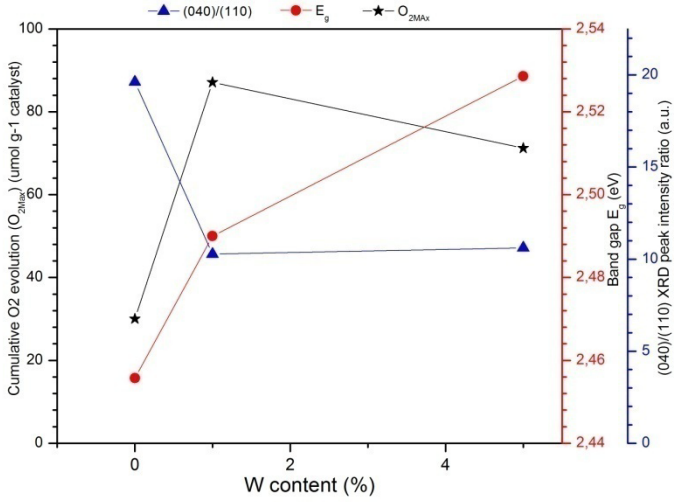

Figure: 6.11. Comparison of the cumulative O_2 evolution, band gap and (040)/(110) XRD peak intensity ratio forW^{6+} doped samples.

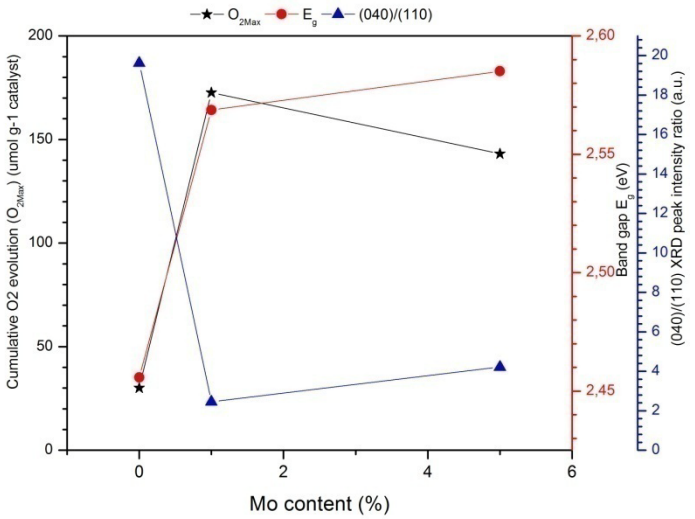

Figure: 6.12. Comparison of the cumulative O_2 evolution, band gap and (040)/(110) XRD peak intensity ratio for Mo^{6+} doped samples.

Based in the results obtained, the most relevant parameters to determine the photocatalytic activity of the doped powders were the peak intensity ratio (040)/(110) and the band gap values. In both cases the cumulative O_2 evolution is properly correlated to these parameters. The fig.6.11 shows a comparison between the most relevant parameters and the cumulative O_2 for the W^{6+}-doped samples and the fig.6.12 the same comparison but in this case for the Mo^{6+}-doped samples.

6.3.3. Characterization $BiVO_4$ Electrode Samples

X-ray diffraction (XRD) was performed to examine changes in the morphology of the samples, and to estimate crystallite sizes and lattice strain parameters for$BiVO_4$ catalysts. The fig.6.13 contains powder XRD patterns for A500x2*h*, A500x6*h*, A600x2*h*, B500x2*h* and B600x2*h* electrodes. *A* and *B* correspond to the 1:2 and 1:4 catalyst-solution proportion respectively. The clearest change was evident in the (040) peak increasing its intensity with the increase of temperature and calcination time, this change was attributed at the morphological changes that suffer the samples, as can be seen in the SEM images in fig.6.14. In the samples a, b and d calcined at 500°C were create aggregates of elongated crystals while in the samples c and e, the aggregates were higher, making the catalyst agglomerate to form large aggregates with larger gaps between them.

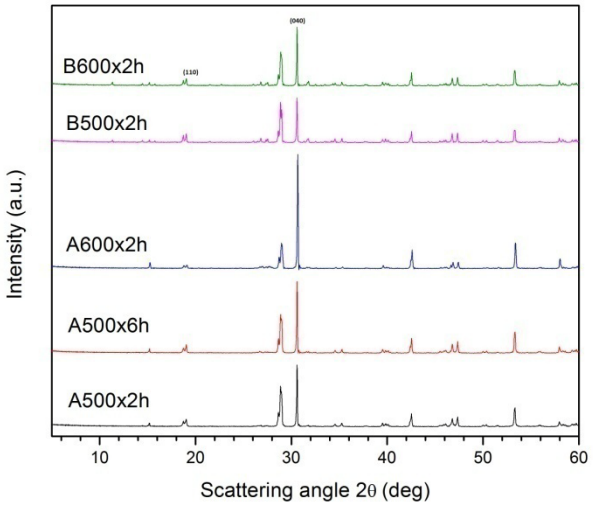

Figure: 6.13. XRD patterns for the $BiVO_4$ electrodes with different annealed treatment, prepared using the same $BiVO_4$ powder synthesized under hydrothermal conditions for 14*h* at *pH* 8.

This formation of larger aggregates can be attributed to the high temperatures to which the electrodes were subjected, creating changes in the crystal lattice that was reflected in the XRD patterns with the increase in the (040) peak. The increase in the (040) was much more noticeable for the sample with proportion 1:2 catalyst-solution. For the preparation of the electrodes were used two kinds of slurry one with a proportion catalyst- solution 1:2 and the other one with a proportion 1:4, the main objective of create two kinds of samples, one more diluted than the other, was the creation of thin films electrodes with thickness around 1*mm*, but the doctor blade technique allowed only reach thickness of 9:5*mm* for the more diluted slurry and thickness of 17*mm* for the less diluted one as can be seen in the SEM images of fig.6.15.

6.3.4. Performance of $BiVO_4$ Electrode Samples and their correlations

In order to have a more practical system, the fabrication of a $BiVO_4$ photoanode is a practical alternative for the design and construction of the photocatalytic devices. The second part of this work refers to the study of $BiVO_4$ electrodes, using $BiVO_4$ powder prepared by hydrothermal synthesis (HTS) and conventional slurry (CS) method for its fabrication. The

Photo-electrochemical characterization was carried out using a standard three electrodes setup described in section 4. The electrolyte used was a solution of Na_2SO_4 0.1*M*, buffered to *pH* 6:56. A *Xe* Arc Lamp (400*W*) connected to a Monochromator by Newport was used as a light source and gave monochromatic light. Photocurrent measurements were performed under simulated *AM*1:5 solar illumination (1000$mW.cm^{-2}$) (1 sun). The current and potential data were measured and regulated using the program "*e-lab*".

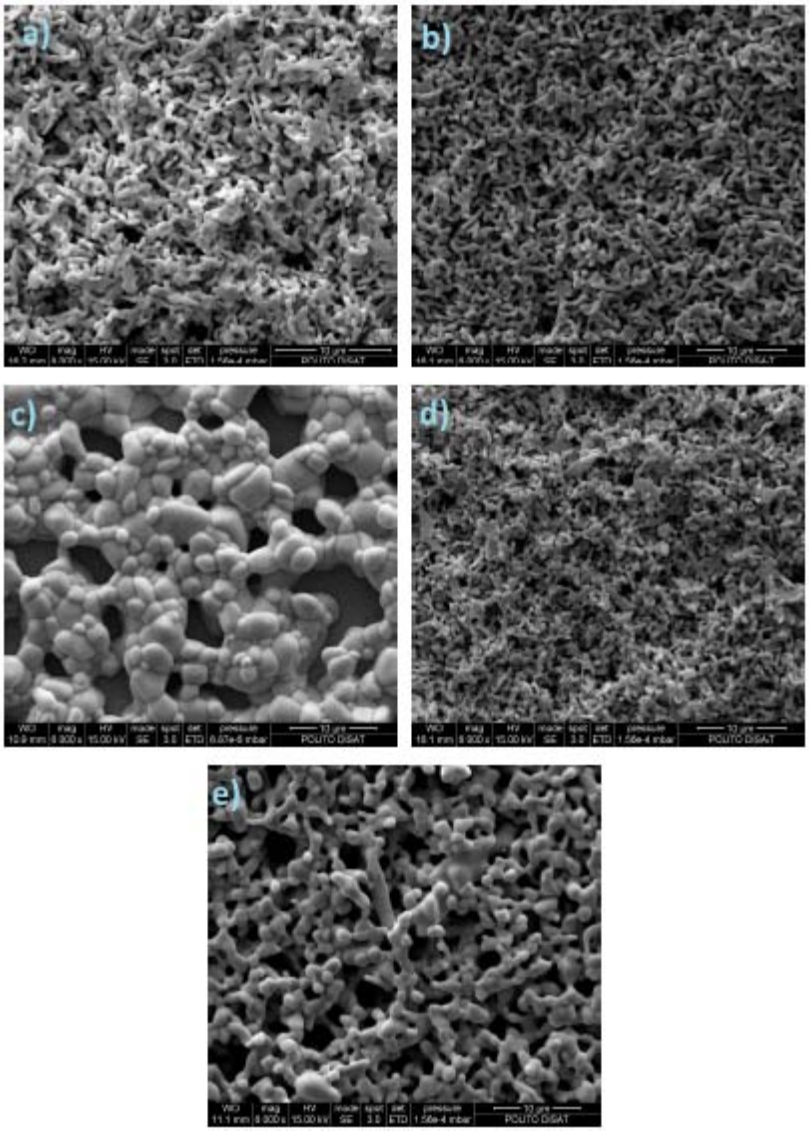

FIGURE: 6.14. SEM images for the $BiVO_4$ electrodes with different annealed treatment, prepared using the same $BiVO_4$ powder synthesized under hydrothermal conditions for 14*h* at *pH* 8. a) A500x2*h*; b) A500x6*h*; c) A600x2*h*; d) B500x2*h* and e) B600x2*h*

Table: 6.2. Summary with the peak intensity ratio (040)/(110) and the Photocurrent-voltage measurements for the $BiVO_4$ electrodes B600x2*h*, A600x2*h*, B500x2*h*, A500x6*h* and A500x2*h* fabricated using a conventional slurry (CS) method and the Doctor Blade technique.

Sample	Peak intensity ratio (040)/(110)	Photocurrent $[mA \cdot cm^{-2}]$
A500x2h	10.672	0.004
A500x6h	9.16	0.007
A600x2h	35.36	0.05
B500x2h	8.8	0.03
B600x2h	5.67	0.34

The highest photocurrent found in the experiment was 0:34$mA.cm^{-2}$ predicted at 1:23V vsRHE and corresponded to the electrode B600x2h while the photocurrent values for the electrodes A600x2*h*, B500x2*h*, A500x6*h* and A500x2*h* were 0:05, 0:03, 0:007, 0:004$mA.cm^{-2}$ predicted at 1:23V vsRHE respectively. As expected the electrodes with a smaller thickness presented a good performance compared with the more thick electrodes. Otherwise, the increase in the temperature for the thermic treatment generated in the electrodes free spaces between the lattices as can be seen in fig.6.14 , allowing light to pass through the electrode and creating a higher interaction with the catalyst. The respective plot for the photocurrent vs Potential vs. *RHE*, is show in fig.6.16.

In order to understand the results obtained in the photo-electrochemical test for the $BiVO_4$ electrodes studied in the standard three electrodes setup, a summary with the peak intensity ratio (040)/(110) and the Photocurrent-voltage measurements is show in table 6.2.

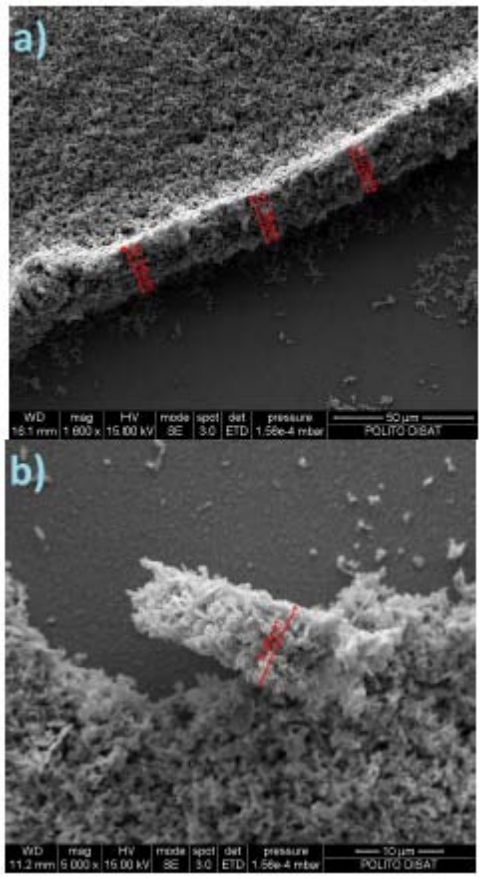

FIGURE 6.15. SEM images for the thickness of $BiVO_4$ electrodes prepared with different proportion catalyst-solution; a) proportion catalyst-solution 1:2; b) proportion catalyst-solution 1:4.

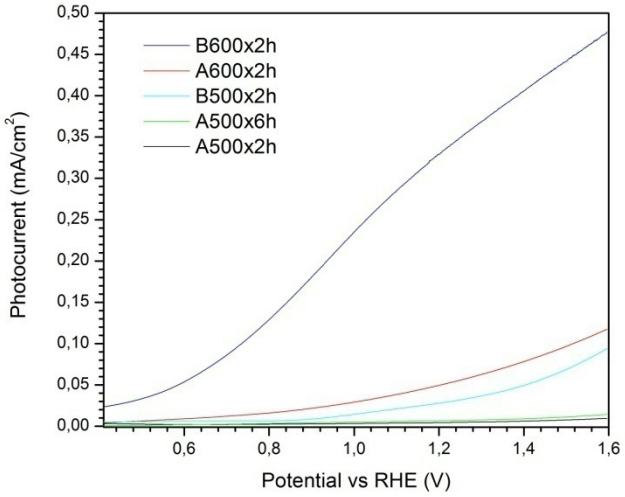

Figure 6.16. Photocurrent-voltage measurement of the back side after different thermic treatments for the electrodes B600x2*h*,A600x2*h*, B500x2*h*, A500x6*h* and A500x2*h* fabricated using conventional slurry (CS) method and the Doctor Blade technique.

The peak intensity ratio (040)/(110) was the main parameter in the previous study of the photocatalytic activity of the undoped and $BiVO_4$ doped powders, for this reason this parameter and the SEM images were the parameters to consider in the correlation for the photo-electrochemical activity of the electrodes. The higher value of peak intensity ratio (040)/(110) was 35:36 and corresponded to the A600x2*h* electrode, this value is the result of the huge agglomeration that the powder suffered to have such a large thickness and having been calcined at high temperature as, however the formation of large spaces between each lattice favoring the passage of light and creating a higher interaction with the catalyst. In the other hand the lower value of peak intensity ratio (040)/(110) was 5:67 and corresponded to the most active electrode, this electrode presented spaces between each lattice and aggregates of elongated crystals whose formation is favored by the decrease of the thickness of the film. The samples A500x2*h* and A500x6*h* presented almost the same values of peak intensity ratio (040)/(110), 10:672 and 9:16 respectively, and very low and similar values of photo-electrochemical activities, it suggest that long periods of time for the calcined process does not affect the photo-electrochemical activities of the electrodes.

6.4. Conclusions

The $BiVO_4$ powder and W^{6+} or Mo^{6+}-doped $BiVO_4$ were obtained using hydrothermal synthesis (HTS) method buffered to *pH* 8 for 14 *h*. All the samples were characterized as monoclinic $BiVO_4$ with some traces of tetragonal phase. The correct incorporation of the cations W^{6+} and Mo^{6+} was determinate by a shift in an specific peak of the XRD patterns for W^{6+}or Mo^{6+}doped $BiVO^4$ compared with the undoped $BiVO_4$ powder. All the doped samples showed an increase in the photocatalytic activity comparing with the undoped powder, being the most active the Mo^{6+}-doped samples, more specifically the Mo^{6+}-doped sample with a dopant content of *Mo*1*wt*.

The correlation of the physical parameters and photocatalytic activity helped to establish that the peak intensity ratio (040)/(110) was the parameter who maintained a high

degree of compatibility with the results of the photocatalytic activity, presenting for the lowest values of peak intensity ratio (040)/(110) the highest activity and vice versa. Otherwise the band gap values are strongly linked to the $BiVO_4$ morphology, and traces of tetragonal $BiVO_4$ could increase the band gap values, like in the Mo^{6+}-doped samples where the presence of tetragonal $BiVO_4$ caused an increase in the band gap values and possibly a decrease in its photocatalytic activity, however were the most actives powders and presented the higher values of production of O_2.

The use of $AgNO_3$ is necessary to carry out the O_2 evolution experiment, however the reduction in the photocatalytic activity due at the interaction between the $BiVO_4$ surface and the reacting Ag^+ centers, imposes severe limitations to the system quickly wearing the catalyst.

In the other hand, were fabricated five $BiVO_4$ electrodes from the $BiVO_4$ powder studied in the first section of this work, using conventional slurry (CS) method and a technique called doctor blade for the deposition of the $BiVO_4$ slurry in the electrodes. The use of the doctor blade technique was not the best option for the deposition of the slurry in the fabrication of thin electrodes, because the thickness reached were not sufficient to meet the desired thickness that revolves around $1\mu m$, nevertheless the study helped to establish three important parameters for the fabrication of the $BiVO_4$ electrodes, i.e. i) The electrodes must be thick enough to let through light and freely interact with the catalyst; ii) The increase in the temperature is important to promote the formation of aggregates with elongated crystals and spaces between them and iii) Long times of calcined are not necessary to improve the photoelectrochemical activity of the electrodes.

6.5. References

1. B. Zhou, J. Qu, X. Zhao, and H. Liu, “Fabrication and photoelectrocatalytic properties of nanocrystalline monoclinic $BiVO_4$ thin-film electrode,” *J. Environ. Sci.-China*, vol. 23, no. 1, pp. 151–159, 2011.

2. G. Xi and J. Ye, “Synthesis of bismuth vanadate nanoplates with exposed {001} facets and enhanced visible-light photocatalytic properties,” *Chem. Commun.*, vol. 46, no. 11, pp. 1893–1895, 2010.

3. D. Ressnig, R. Kontic, and G. R. Patzke, “Morphology control of $BiVO_4$ photocatalysts: *pH* optimization vs. self-organization,” *Mater. Chem. Phys.*, vol. 135, no. 2–3, pp. 457–466, Aug. 2012.

4. S. Obregon, A. Caballero, and G. Colon, “Hydrothermal synthesis of $BiVO_4$: Structural and morphological influence on the photocatalytic activity,” *Appl. Catal. B-Environ.*, vol. 117, pp. 59–66, May 2012.

5. D. Wang, R. Li, J. Zhu, J. Shi, J. Han, X. Zong, and C. Li, “Photocatalytic Water Oxidation on $BiVO_4$ with the Electrocatalyst as an Oxidation Cocatalyst: Essential Relations between Electrocatalyst and Photocatalyst,” *J. Phys. Chem. C*, vol. 116, no. 8, pp. 5082–5089, Mar. 2012.

6. J. Yang, D. Wang, X. Zhou, and C. Li, “A Theoretical Study on the Mechanism of Photocatalytic Oxygen Evolution on $BiVO_4$ in Aqueous Solution,” *Chem.- Eur. J.*, vol. 19, no. 4, pp. 1320–1326, Jan. 2013.

7. Y. Park, K. J. McDonald, and K.-S. Choi, “Progress in bismuth vanadate photoanodes for use in solar water oxidation,” *Chem. Soc. Rev.*, vol. 42, no. 6, pp. 2321–2337, 2013.

8. K. Maeda, “Photocatalytic water splitting using semiconductor particles: History and recent developments,” *J. Photochem. Photobiol. C-Photochem. Rev.*, vol. 12, no. 4, pp. 237–268, Dec. 2011.

9. K. P. S. Parmar, H. J. Kang, A. Bist, P. Dua, J. S. Jang, and J. S. Lee, “Photocatalytic and Photoelectrochemical Water Oxidation over Metal-Doped Monoclinic $BiVO_4$ Photoanodes,” *Chemsuschem*, vol. 5, no. 10, pp. 1926–1934, 2012.

10. H. S. Park, K. E. Kweon, H. Ye, E. Paek, G. S. Hwang, and A. J. Bard, “Factors in the Metal Doping of $BiVO_4$ for Improved Photoelectrocatalytic Activity as Studied by Scanning Electrochemical Microscopy and First-Principles Density-Functional Calculation,” *J. Phys. Chem. C*, vol. 115, no. 36, pp. 17870–17879, Sep. 2011.

11. H. W. Jeong, T. H. Jeon, J. S. Jang, W. Choi, and H. Park, “Strategic Modification of $BiVO_4$ for Improving Photoelectrochemical Water Oxidation Performance,” *J. Phys. Chem. C*, vol. 117, no. 18, pp. 9104–9112, Apr. 2013.

12. K. Gelderman, L. Lee, and S. W. Donne, “Flat-band potential of a semiconductor: using the Mott-Schottky equation,” *J. Chem. Educ.*, vol. 84, no. 4, pp. 685–688, Apr. 2007.

13. J. Langford and A. Wilson, “Scherrer After 60 Years - Survey And Some New Results In Determination,” J. Appl. Crystallogr., vol. 11, no. Apr, pp. 102–113, 1978.

14. Pankove, J. L. Optical Processes in Semiconductors; Prentice Hall: Englewood, Cliffs, New Jersey, 1971.

15. Finlayson, A. P.; Tsaneva, V. N.; Lyons, L.; Clark, M.; Glowacki, B. A. Physica Status Solidi a- Applications and Materials Science 2006, 203, 327-335.

16. “UV-vis Spectrometry,” ASCG. [Online]. Available:

17. http://www.msm.cam.ac.uk/ascg/characterisation/uvvis.php. [Accessed: 17-May-2014].

18. Kudo, A., Omori, K., & Kato, H. A novel aqueous process for preparation of crystal form-controlled and highly crystalline $BiVO_4$ powder from layered vanadates at room temperature and its photocatalytic and photophysical properties, J. Am. Chem. Soc. 121, 11459-11467 (1999).

19. A. Kudo, K. Ueda, H. Kato, and I. Mikami, “Photocatalytic O_2 evolution under visible light irradiation on $BiVO_4$ in aqueous $AgNO_3$ solution,” Catal. Lett., vol. 53, no. 3–4, pp. 229–230, Aug. 1998.

20. D. Wang, H. Jiang, X. Zong, Q. Xu, Y. Ma, G. Li, and C. Li, “Crystal Facet Dependence of Water Oxidation on $BiVO_4$ Sheets under Visible Light Irradiation,” Chem. – Eur. J., vol. 17, no. 4, pp. 1275–1282, 2011.

7. Chapter 7. Rapid Synthesis of $BiVO_4$ Thin Films on FTO Electrodes for Water Splitting Under Visible Light Irradiation

7.1. Introduction

The most promising technology for the production of hydrogen from renewable energy sources is photo-electrochemical water splitting exploiting solar light.(1,2) However, the greatest challenge of this technology is that anodic electrodes are needed to overcome the high over-potential required to perform the water oxidation four-electron reaction, which is responsible for the slow kinetics of such a photo-electrochemical system.(3) There is an ever increasing need to develop efficient and robust light harvesters, water oxidation catalysts and photo-catalysts in order to develop a commercially viable photo-electrochemical cell (PEC) for H_2 production, with a higher efficiency than 10%. Therefore, an improvement in charge generation, separation and transfer at the electrodes is required to enhance the efficiency of the PEC system, which is currently lower than photovoltaic cells coupled to electrolyzers.(4)

Semiconductor materials for this kind of approach have been studied extensively since the first report on photo-electrochemical water splitting with TiO_2 by Fujishima and Honda in 1972.(5) Of all the different kinds of semiconductor materials(6) that are available, metal oxides have attracted a great deal of interest thanks to their cost effectiveness and stability. Among these metal oxide semiconductors, Bismuth Vanadate has demonstrated to be a promising material for water oxidation.(7-9)$BiVO_4$ presents three crystal systems: a Scheelite structure with monoclinic *(s-m)* (highly active), tetragonal *(s-t)* phases, and a zirconia structure with a tetragonal *(z-t)* phase(8) Some of the commonly quoted advantages of $BiVO_4$ are: i) a low band gap of about 2.4 *eV* (for monoclinic scheelite), which roughly corresponds to a 520 *nm* wavelength that allows a good visible-photon absorbance capability;(8-10) ii) a Valence Band (VB) position which is sufficiently negative (ca. 2.4 *V* vs RHE) with respect to water oxidation, and a Conduction Band (CB) that is around 0 *V* vs. RHE, thus implying a thermodynamic level close to H_2;(8, 10-12) iii) the effective masses of the electrons and holes have been estimated to be lower than similar semiconductors (e.g. In_2O_3 or TiO_2), and this, in principle, would result in improved separation and extraction processes of the electron-hole pairs,(8, 10-12) iv) it is composed of inexpensive elements and is non-toxic.((11, 12)

Although the synthesis of $BiVO_4$ powders is useful for an in-depth analysis of crystal properties, these powders are actually unsuitable from the practical application point of view. For this reason, photoelectrodes are dealt with the development of devices for solar water oxidation. The photoelectrode concept has become popular, compared to the direct utilization of powder, since the compartmentalization of O_2 and H_2 is simpler. Different approaches with diverse performances and efficiencies have been applied to date. In general, the formation of a thin film over a conductive substrate, usually Fluorine doped Tin Oxide (FTO) or the more expensive Indium Tin Oxide (ITO), is achieved via a solution-based method,(13) electrochemical deposition,(14) direct crystal growth,(15) or powder synthesis (as described above) and later impregnation of these as films.(16)

Among the available in situ thin film deposition techniques, dip coating has attracted a great deal of attention because of its advantages. Dip coating is in fact a simple method of depositing a uniform liquid thin which then solidifies into a coating on a substrate.(13) Many reports have been written on the fabrication of thin $BiVO_4$ films by the available techniques,(8,

14, 17, 18) but there is still an urgent need to address the importance of the thickness of $BiVO_4$ films and their characteristics regarding the photocatalytic activity of the system.

The simple fabrication of stable and reproducible thin films of pure $BiVO_4$ on FTO conducting glass electrodes, employing a dip coating procedure, and their efficient use as photoanodes for the water oxidation reaction is herein reported. Insights are provided, from electrochemical impedance spectroscopy, about the different types of processes that occur in the film as a function of the thickness of the as synthesized $BiVO_4$ film. These images have clearly pointed out that the thickness of the film is a key factor for the performance of the catalyst.

7.2. Experimental Section

7.2.1. Materials

Bismuth *(III)* nitrate pentahydrate $(Bi(NO_3)_3.5H_2O)$, Ammonium metavanadate (NH_4VO_3) and Nitric acid (HNO_3) were purchased from Sigma Aldrich. The conductive FTO glasses, with a sheet resistance of 7 $\Omega.cm^{-2}$, were obtained from SOLARONIX Inc.

7.2.2. Synthesis of Thin Films

The raw materials involved in this process are Bismuth nitrate, Ammonium metavanadate and Nitric acid. 1.121 *g* of $Bi(NO_3).5H_2O$ and 0.292 *g* of NH_4VO_3 were mixed in 50 *ml* of 1*M* HNO_3 until a clear homogenous solution was obtained. The solution was then filtered through Whatman filter paper to obtain a clear solution. This solution was employed in the dip coating procedure. The FTO electrodes were cleaned in acetone, ethanol and then with distilled water using an ultrasound bath. The dip coating process was performed at a controlled speed of $1 mm \cdot s^{-1}$. A series of electrodes with different thicknesses was prepared by varying the number of layers through the dip-coating procedure. Thereafter, each sample is designated as *BV-n*, where *n* stands for the number of deposited layers. A calcination step was performed at 450 °*C* for 20 *min* in air after each dipping. A final calcination was performed on all of the samples at 450 ^oC for 2 *h* in air.

7.3. Characterization

7.3.1. Structural Characterization

The $BiVO_4$ samples were characterized through X-ray diffraction (XRD) using an X'Pert Phillips diffractometer equipped with *Cu Kα* radiation (λ = 1.5418 *Å*) at 40 *kV* and 30 *mA*. All the patterns were recorded in the 5 – 60 ° range, with a step size of 0.02 °. The crystallite sizes of the samples were estimated using the Scherrer formula.(13, 19)

$$D = K\lambda/\beta cos\theta \qquad Eq \rightarrow 7.1$$

where*D* is the average crystallite size *(nm)*, λ is the wavelength of the X-ray radiation, *K* is the shape factor (0.9), β is the peak width at half-maximum height, corrected for instrumental broadening, and 2θ = 30.6 °. The UV-Vis diffuse reflectance spectra were recorded on a UV-Vis Varian Cary 5000 spectrophotometer equipped with an integrating sphere. The morphology of the samples was investigated by means of scanning electron

microscopy (SEM) using a FE-SEM MERLIN ZEISS equipped with an energy dispersive analysis system (EDS), which was employed to obtain an insight into the bulk element composition of the sample.

7.3.2. Photo-electrochemical Characterization

The photoelectrochemical characterizations of the $BiVO_4$ electrodes used as photoanodes for the water oxidation reaction were carried out in an aqueous 0.1*M* Na_2SO_4 electrolyte solution (*pH*~ 6.2), employing a multi-channel VSP potentiostat/galvanostat made by BioLogic. A three-electrode system, consisting of the $BiVO_4$ material as the working electrode, a platinum counter electrode and an *Ag/AgCl* (3*M*) as the reference electrode was used. Linear scan voltammetries (LSVs) were performed in the dark and under simulated solar light, using a 450 *W* Xe lamp by Newport with an *AM* 1.5 filter and a water filter. The intensity of the light was maintained at 100 $mW\ cm^{-2}$ by adjusting the distance between the source and the PEC. Chrono-amperometry (*I-t*) measurements were performed at 0.6 *V* vs. *Ag/AgCl* over continuous light ON-OFF cycles. Electrochemical Impedance Spectroscopy (EIS) measurements were conducted in the 100 *mHz* to 1*MHz* frequency range, with an amplitude of 25 *mV*, under different applied DC potentials in the -0.3 *V* to 0.9 *V* vs. *Ag/AgCl*range,with 0.3 *V* steps. The EIS data were modeled using ZSimpWin (EChemSoftware). Incident-Photon-to-Current-Efficiency (IPCE) was recorded using a Newport Xe lamp (150 *W*) coupled to a monochromator (Cornestone 130 by Newport), by varying the wavelength of the incident light from 300 *nm* to 570 *nm* (step size: 10 *nm*), at an applied potential of 0.6 *V* vs. *Ag/AgCl*. The electrochemical data presented in the work refer to the reversible hydrogen electrode (RHE) potential, calculated with $E_{RHE} = E_{Ag/AgCl} + 0.209\ V + 0.059 \cdot pH$.

7.4.Results

7.4.1. Structural, Morphological and Optical Investigations

Prior to being used as photoanodes for the water splitting reaction, $BiVO_4$ films of various thickness were characterized through different techniques, such as XRD, UV-Vis spectroscopy, SEM and EDS.

The XRD analysis has confirmed that all the films exhibit the monoclinic phase of $BiVO_4$ (which is considered as the only active phase). The tetragonal zircon-type phase in fact changes to a monoclinic scheelite-type phase after calcining at higher temperatures than 400 ^oC.(20) It can be seen from Fig. 7.1 that, regardless of the number of deposited layers, the patterns of the diverse samples present the same typical peaks as the monoclinic family of $BiVO_4$ (standard card No. 14-0688, space group: *I2/a*, a = 5.195, b = 11.701, c = 5.092, β = 90.38 ^{o}). The monoclinic nature of $BiVO_4$ can be confirmed from the peak splitting that is observed at 18.5 ° and 35 ° of 2θ, which is indicated with arrows over the peaks. The intensity of the $BiVO_4$ peaks grows as the number of layers is increased, which indicates that a larger amount of material is deposited onto the FTO surface. In addition, the crystal sizes were also determined using the Scherrer equation, as stated in *eq. 1*, and are reported in Table 7.1. By observing these values, it can be concluded that the crystallite size increases as the number of deposited layers is incremented, probably due to the increased amount of material and the larger number of intermediate calcination steps performed at 450 ^oC for 20 *min*.

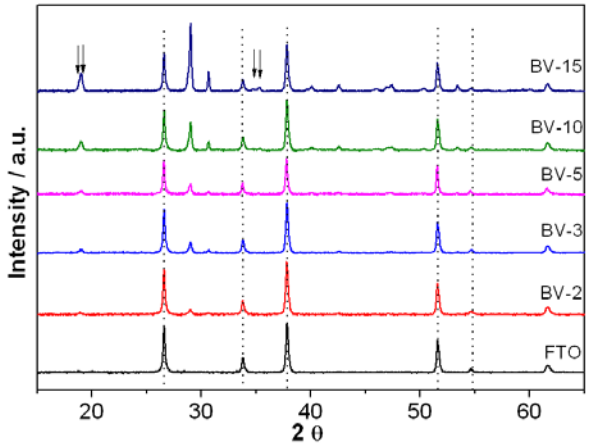

Figure:7.1. XRD spetra of the *BiVO₄* films for different numbers of dip-coated layers.

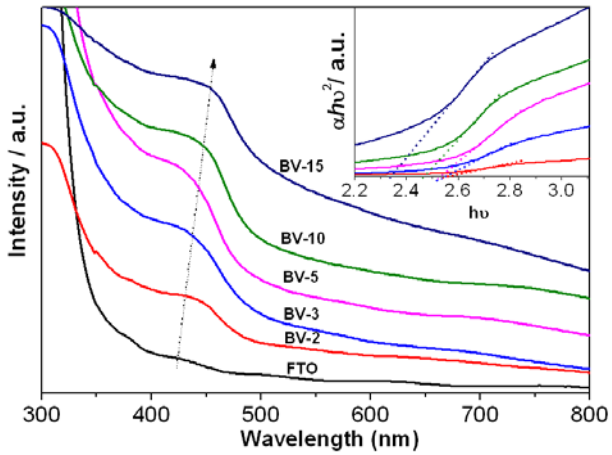

Figure:7.2. UV-Vis diffuse reflectance spectra of the *BiVO₄* films for different numbers of dip-coated layers. Inset: Tauc plots of the same films.

Table 7.1: Properties of the *BiVO₄* films as a function of the number of coated layers

Sample	Bi/atomic %	V/atomic %	Thickness/nm	Crystallite size/ nm	Band gap / eV
BV-2	0.65	1.28	60	24	2.55
BV-3	0.97	1.93	80	28	2.51
BV-5	1.86	2.90	115	34	2.50
BV-10	4.06	5.29	160	52	2.46
BV-15	6.79	7.60	210	65	2.35

To calculate the electronic states of the semiconductor materials, diffuse reflectance spectra (DRS) were used. Fig. 7.2 shows the UV-Vis reflectance spectra of the films, as well as that of the FTO substrate. The Tauc plots, which give indications on the band gap of the

material, are reported in the insert. All the samples show absorption in the visible region of the electromagnetic spectrum. This gives information about the monoclinic nature of the $BiVO_4$ samples.(21) Changes in the absorption edges can be recognized among the $BiVO_4$ samples along with the FTO substrate. In particular, a red shift was observed when the thickness of the film was increased. The band gaps were calculated using the Tauc plot and are reported in Table 7.1. A reduction in the band gap can be observed for an increase in the thickness and crystallite size of the $BiVO_4$. As in our previous work,(9) this could be explained by a higher delocalization of the electron and hole pairs and a greater overlapping between the *Bi 6s* and *O 2p* orbitals with an increase in $BiVO_4$ crystals. The morphologies of the deposited $BiVO_4$films were studied through FESEM analysis. A considerable difference in the samples can be observed from an examination of the top view in Fig. 7.3 (a, b and c). Some pores in fact form during the calcination process as the solvent evaporates and the particles start to agglomerate. This could facilitate the penetration of light and the electrolyte through the film. In addition, the thicknesses of the samples were determined by means of FESEM (see Fig. 7.3d), and the values are reported in Table 7.1. As expected, the larger the number of deposited layers, the higher the film thickness. A maximum of 210 *nm* was obtained after 15 repeated deposition steps. The atomic and weight percentages of Bismuth and Vanadium were acquired from EDX analysis, and are presented in Table 7.1. These percentages offer further confirmation of the increase in the amount of $BiVO_4$ material on the FTO electrode and of the purity of the material up to a certain extent.

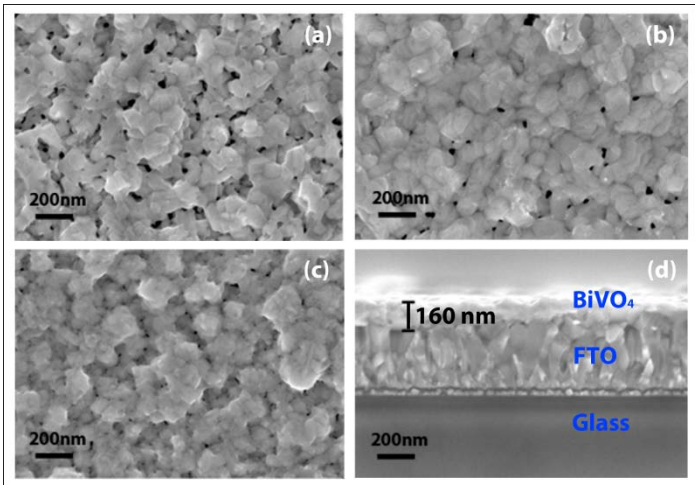

Figure:7.3.FESEM images of the $BiVO_4$ films: top view of the BV-3 (a), BV-10 (b) and BV-15 (c) samples, cross section of the BV-10samplewith measurement of the $BiVO_4$ film thickness.

7.4.2. Photo-Eletrochemical Performance

The photocatalytic activity of the $BiVO_4$films was evaluated by using them as anodes for the photo-electrochemical water splitting reaction. The LSV curves of the photoelectrodes acquired under *AM*1.5G illumination (see Fig. 7.4a) show the current density as a function of the applied potential in the PEC system. The current density remains negligible for all the samples until the water oxidation onset potential is reached: this potential represents the thermodynamic limit value, beyond which water electrolysis occurs. It is worth noting that all the curves are characterized by an onset potential well below 1.23 *V*, which represents the

minimum voltage that should be applied to obtain cold water dissociation in dark conditions (6, 22) this feature highlights the photocatalytic activity of the fabricated films. As can be observed from all the curves in Fig. 7.4a, the current increases quite linearly without any disturbances and so this indicates that the material is not undergoing any changes. The effect of the photo-anode thickness on the catalytic activity is also visible in the LSV curves. Thinner films are characterized by a rising current density while the number of deposited layers increases. The maximum photocatalytic activity was reached for the 10 layer sample, while the thickest film exhibited a lower current.

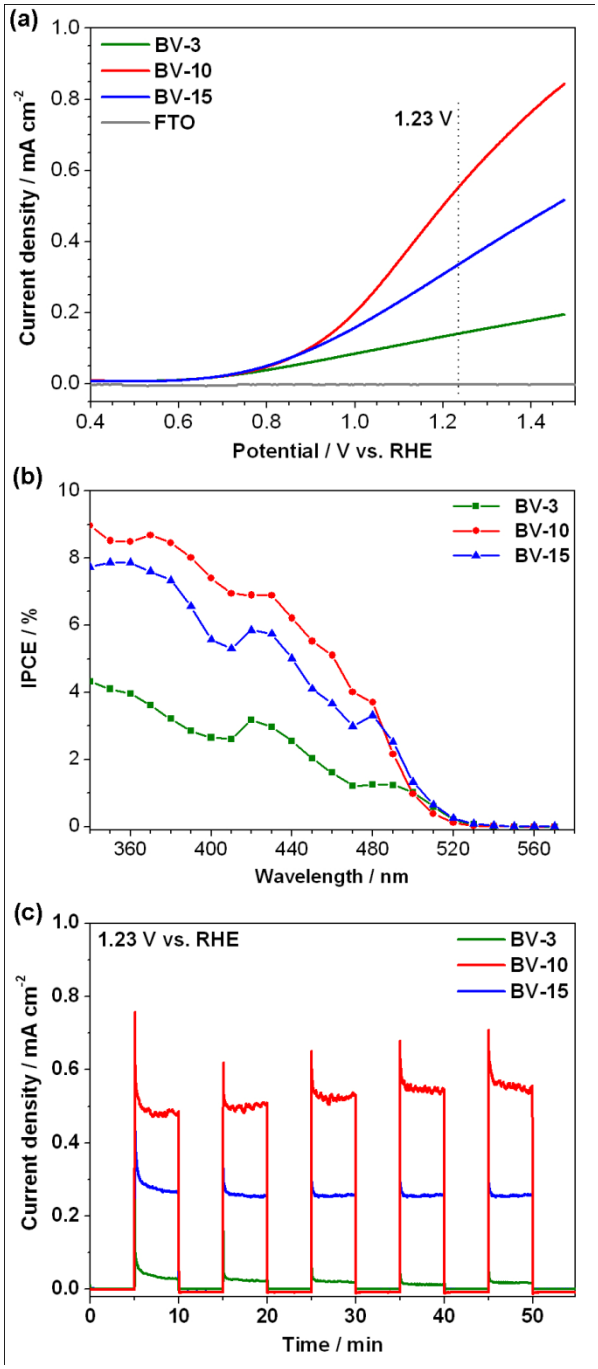

Figure:7.4. Photo-electrochemical characterization of the $BiVO_4$ electrodes with different thicknesses: (a) Photocurrentresponse vs. potential under simulated sunlight illumination (AM 1.5G, 100 $mW\ cm^{-2}$), (b) IPCE spectra, and (c) crono-amperometric curvesat 1.23V vs. RHE, under continuous dark-light (AM 1.5G, 100 $mW\ cm^{-2}$) cycles.

The same feature is also evident in the results of the IPCE measurements (Fig. 7.4b): the total photocurrent of the BV-10 film is larger than those of the thinner (BV-3) and thicker (BV-15) films. However, the IPCE spectrum of all the samples exhibits non-zero values for lower wavelengths than 530 *nm*, thus confirming that $BiVO_4$films are efficient catalytic materials for solar-driven oxidation reactions.

Similarly, the chrono-amperometric measurements, which were performed in order to check the stability of the $BiVO_4$ photoanodes, have also revealed that the current density dependence on the thickness of the material is not monotonic (see Fig. 7.4c). In fact, even though the *I-t* curves show good photocurrent stability under numerous light ON-OFF cycles over a longer period than 60 *min*, some limiting parameters emerge for thicker films, and show a negative influence on the activity. The charge transfer mechanism that occurs in thin $BiVO_4$ films was analyzed in detail by means of the electrochemical impedance spectroscopy technique in order to obtain a better understanding of this kind of behavior, as reported in the following section.

7.4.3. Electrochemical Impedance Spectroscopy Analysis

EIS is a well known technique that is widely employed in electrochemical systems and devices for different kinds of applications,(23) including photo-electrochemical water splitting.(24) Here it has been exploited to study the charge transfer process at the semiconductor/electrolyte interface. Examples of the results are reported in Fig. 7.5. A decrease in the total impedance for an increase in the applied potential is evident in the Bode plot of modulus related to the BV-10 sample, in agreement with the results obtained from LSV analysis. Looking at the phase spectrum, two processes can be recognized for low applied potentials, namely, the charge transfer at the solid/liquid interface (Helmholtz layer), which can be identified in the low frequency region, and the charge transport inside the film (depletion layer), which is distinguishable in the high frequency region.(25) The charge transfer becomes faster as the voltage increases (i.e. the corresponding peak shift towards higher frequencies), and is finally comparable with that of other processes for larger potentials than 0.6 *V* vs. *Ag/AgCl* (corresponding to the onset potential in Fig. 7.4a).

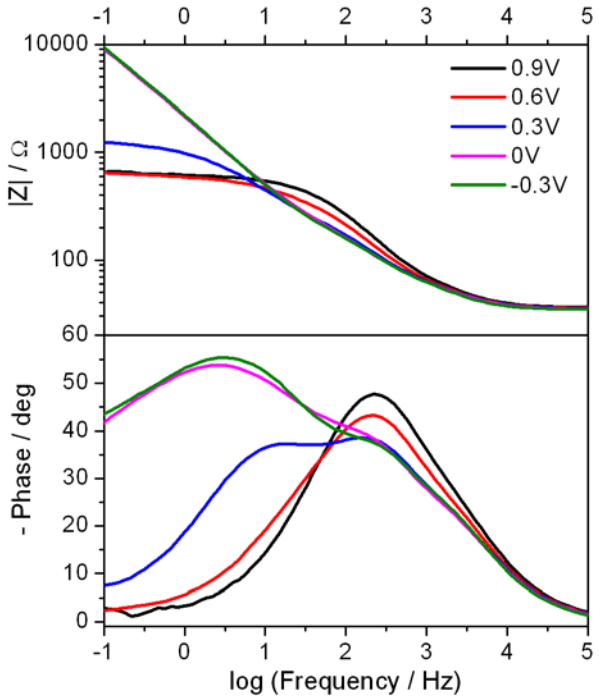

Figure:7.5: Bode plots of the EIS measurements in the BV-10 electrode at different applied potentials, under AM 1.5G light illumination (100 $mW\ cm^{-2}$).

The Bode plots of the impedance of the $BiVO_4$electrodes, with the different thicknesses acquired under illumination at 0.9 *V* vs. *Ag/AgCl* are reported in Fig. 7.6. The modulus of the BV-3 sample is characterized by larger impedance than the other two films, thus showing that a minor current is produced during the electrolysis reaction as a consequence of the reduced quantity of the deposited material. Conversely, the impedance of the thicker film is comparable with that of the BV-10 one. This behavior can be explained by examining the phase plots: the BV-15 sample is in fact characterized by an additional process that occurs at very large frequencies (around 5 *kHz*), as can be seen from the side feature that is visible in the main peak. This fact suggests that a charge transfer mechanism has occurred via surface states,(26, 27) which could be due to an imperfect interconnection between adjacent layers in the thicker films. On the other hand, the thinner films (up to ten layers) are characterized by a single charge transfer process.

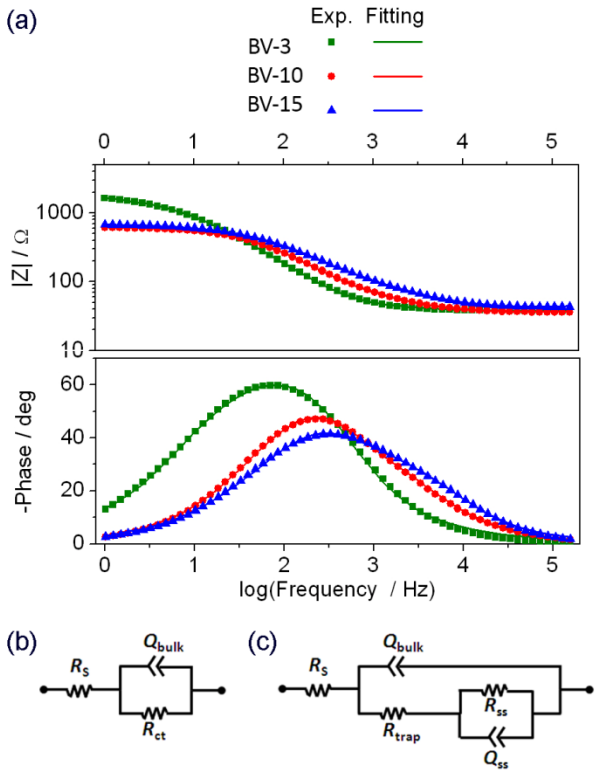

Figure:7.6. Bode plots of the EIS measurements (symbols) and fitted data (lines) acquired using the $BiVO_4$ electrodes with different thicknesses at 0.9*V* vs. *Ag/AgCl* under AM 1.5G light tillumination (100 $mW\ cm^{-2}$). The experimental data of the BV-3 and BV-10electrodeswere fitted using the equivalent circuit (EC) depicted in (b), whilethe EC in (c) was employed for the BV-15 electrode.

For this reason, two different equivalent circuits (ECs) were employed to fit the experimental EIS data: the one reported in Fig. 7.6b for thinner electrodes, the EC in Fig. 7.6c for the BV-15 film. The simpler circuit is constituted by the series resistance R_s (which accounts for the resistances of: the FTO film, the external electrical contacts and the liquid electrolyte resistance) and by the parallel between the charge transfer resistance R_{ct} and the constant phase element (CPE) Q_{bulk}, which represents the direct charge transfer at the semiconductor/electrolyte interface. CPEs were used instead of common capacitance to take into account the frequency dispersion due to the porosity of the films.(23, 28) In the EC in Fig. 7.6c, R_{ct} is substituted by the resistance *Rtrap* (which represents the trapping of charges in the surface states) and by the parallel between the resistance R_{ss} (which models the charge transfer between the electrolyte and the surface states) and the surface state CPE Q_{ss}.(26) The results of the fitting procedures are reported in Fig. 7.6a, where they are superimposed onto the experimental curves. The R_s values do not depend on the film thickness, as all the values are around 40 *Ω*. Conversely, the charge transfer resistances reduced when was increased and reached the number of deposited layers, reaching a minimum of 590 *Ω* for the BV-10 sample. The same behavior is exhibited by the charge transfer time, *τct*, calculated through the formula:(29)

$$\tau_{ct} = (R_{ct} Q_{bulk})^{1/n_{ct}} \qquad (2) \qquad \textit{Eq. 7.2}$$

where n_{ct} is the CPE index: this value is equal to 24 *ms* for the BV-3 film and reduces to 4 *ms* for the BV-10 film, thus evidencing a faster process as a consequence of the larger quantity of active material available for the water splitting reaction. As far as the BV-15 sample is concerned, the charge transfer (which occurs through the surface states) instead shows that is a time constant comparable with that of the BV-10 film (equal to 2.5 *ms*), but the presence of the additional trap resistance (equal to 44 Ω), leads to a reduced total catalytic activity compared to the sample grown with 10 deposited layers.

7.5. Conclusions

The photocatalytic activity of $BiVO_4$ has been assessed through the photoinduced oxidation of water. Linear scan voltammetries and chrono-amperometry measurements have been carried out to obtain insights into the activity and stability of the fabricated thin films. It has been revealed that an optimal thickness, which is necessary to obtain the maximum photocatalytic activity of pure $BiVO_4$ thin films, can be obtained.

EIS analysis has been conducted in order to understand the charge transfer process for different film thicknesses. It has been observed that the traps that are present in thicker films (which hinder the charge transfer process) are the main reason for the decrease in the photocatalytic activity of the whole system.

7.6. References

1. T. Bak, J. Nowotny, M. Rekas, C.C. Sorrell, Photo-electrochemical hydrogen generation from water using solar energy. Materials-related aspects, International Journal of Hydrogen Energy, 27 (2002) 991-1022.

2. Z. Li, W. Luo, M. Zhang, J. Feng, Z. Zou, Photoelectrochemical cells for solar hydrogen production: current state of promising photoelectrodes, methods to improve their properties, and outlook, Energy & Environmental Science, 6 (2013) 347-370.

3. M.W. Kanan, D.G. Nocera, In Situ Formation of an Oxygen-Evolving Catalyst in Neutral Water Containing Phosphate and Co^{2+}, Science, 321 (2008) 1072-1075.

4. M. Gratzel, Photoelectrochemical cells, Nature, 414 (2001) 338-344.

5. A. Fujishima, K. Honda, Electrochemical photolysis of water at a semiconductor electrode, Nature, 238 (1972) 37-38.

6. A. Kudo, Y. Miseki, Heterogeneous photocatalyst materials for water splitting, Chemical Society Reviews, 38 (2009) 253-278.

7. A. Kudo, K. Ueda, H. Kato, I. Mikami, Photocatalytic O_2 evolution under visible light irradiation on $BiVO_4$ in aqueous $AgNO_3$ solution, Catalysis Letters, 53 (1998) 229-230.

8. Y. Park, K.J. McDonald, K.-S. Choi, Progress in bismuth vanadate photoanodes for use in solar water oxidation, Chemical Society Reviews, 42 (2013) 2321-2337.

9. S.M. Thalluri, C. Martinez Suarez, M. Hussain, S. Hernandez, A. Virga, G. Saracco, N. Russo, Evaluation of the Parameters Affecting the Visible-Light-Induced Photocatalytic Activity of Monoclinic $BiVO_4$ for Water Oxidation, Industrial & Engineering Chemistry Research, 52 (2013) 17414-17418.

10. A. Walsh, Y. Yan, M.N. Huda, M.M. Al-Jassim, S.-H. Wei, Band Edge Electronic Structure of $BiVO_4$: Elucidating the Role of the *Bi s* and *V d* Orbitals, Chemistry of Materials, 21 (2009) 547-551.

11. K. Maeda, Photocatalytic water splitting using semiconductor particles: History and recent developments, Journal of Photochemistry and Photobiology C: Photochemistry Reviews, 12 (2011) 237-268.

12. Z. Zhao, Z. Li, Z. Zou, Electronic structure and optical properties of monoclinic clinobisvanite $BiVO_4$, Physical Chemistry Chemical Physics, 13 (2011) 4746-4753.

13. Q. Jia, K. Iwashina, A. Kudo, Facile fabrication of an efficient $BiVO_4$ thin film electrode for water splitting under visible light irradiation, Proceedings of the National Academy of Sciences, 109 (2012) 11564-11569.

14. R. Saito, Y. Miseki, K. Sayama, Highly efficient photoelectrochemical water splitting using a thin film photoanode of $BiVO_4/SnO_2/WO_3$ multi-composite in a carbonate electrolyte, Chemical Communications, 48 (2012) 3833-3835.

15. J. Su, L. Guo, S. Yoriya, C.A. Grimes, Aqueous Growth of Pyramidal-Shaped $BiVO_4$ Nanowire Arrays and Structural Characterization: Application to Photoelectrochemical Water Splitting, Crystal Growth & Design, 10 (2009) 856-861.

16. K.P.S. Parmar, H.J. Kang, A. Bist, P. Dua, J.S. Jang, J.S. Lee, Photocatalytic and Photoelectrochemical Water Oxidation over Metal-Doped Monoclinic $BiVO_4$ Photoanodes, ChemSusChem, 5 (2012) 1926-1934.

17. S.J. Hong, S. Lee, J.S. Jang, J.S. Lee, Heterojunction $BiVO_4/WO_3$ electrodes for enhanced photoactivity of water oxidation, Energy & Environmental Science, 4 (2011) 1781-1787.

18. F.F. Abdi, L. Han, A.H.M. Smets, M. Zeman, B. Dam, R. van de Krol, Efficient solar water splitting by enhanced charge separation in a bismuth vanadate-silicon tandem photoelectrode, Nat Commun, 4 (2013).

19. D. Grosso, How to exploit the full potential of the dip-coating process to better control film formation, Journal of Materials Chemistry, 21 (2011) 17033-17038.

20. H. Fan, T. Jiang, H. Li, D. Wang, L. Wang, J. Zhai, D. He, P. Wang, T. Xie, Effect of $BiVO_4$ Crystalline Phases on the Photoinduced Carriers Behavior and Photocatalytic Activity, The Journal of Physical Chemistry C, 116 (2011) 2425-2430.

21. S.M. Thalluri, C. Martinez Suarez, S. Hernández, S. Bensaid, G. Saracco, N. Russo, Elucidation of important parameters of $BiVO_4$ responsible for photo-catalytic O_2 evolution and insights about the rate of the catalytic process, Chemical Engineering Journal, 245 (2014) 124-132.

22. J.Y. Kim, G. Magesh, D.H. Youn, J.-W. Jang, J. Kubota, K. Domen, J.S. Lee, Single-crystalline, wormlike hematite photoanodes for efficient solar water splitting, Sci. Rep., 3 (2013).

23. X. Dominguez-Benetton, S. Sevda, K. Vanbroekhoven, D. Pant, The accurate use of impedance analysis for the study of microbial electrochemical systems, Chemical Society Reviews, 41 (2012) 7228-7246.

24. T. Lopes, L. Andrade, H.A. Ribeiro, A. Mendes, Characterization of photoelectrochemical cells for water splitting by electrochemical impedance spectroscopy, International Journal of Hydrogen Energy, 35 (2010) 11601-11608.

25. D. Hidalgo, R. Messina, A. Sacco, D. Manfredi, S. Vankova, E. Garrone, G. Saracco, S. Hernández, Thick mesoporous TiO_2 films through a sol–gel method involving a non-ionic surfactant: Characterization and enhanced performance for water photo-electrolysis, International Journal of Hydrogen Energy, doi: 10.1016/j.ijhydene.2014.02.163 (2014).

26. B. Klahr, S. Gimenez, F. Fabregat-Santiago, T. Hamann, J. Bisquert, Water Oxidation at Hematite Photoelectrodes: The Role of Surface States, Journal of the American Chemical Society, 134 (2012) 4294-4302.

27. L. Badia-Bou, E. Mas-Marza, P. Rodenas, E.M. Barea, F. Fabregat-Santiago, S. Gimenez, E. Peris, J. Bisquert, Water Oxidation at Hematite Photoelectrodes with an Iridium-Based Catalyst, The Journal of Physical Chemistry C, 117 (2013) 3826-3833.

28. J. Bisquert, G. Garcia-Belmonte, F. Fabregat-Santiago, N.S. Ferriols, P. Bogdanoff, E.C. Pereira, Doubling Exponent Models for the Analysis of Porous Film Electrodes by Impedance. Relaxation of TiO2 Nanoporous in Aqueous Solution, The Journal of Physical Chemistry B, 104 (2000) 2287-2298.

29. S. Hernández, M. Tortello, A. Sacco, M. Quaglio, T. Meyer, S. Bianco, G. Saracco, C.F. Pirri, E. Tresso, New Transparent Laser-Drilled Fluorine-doped Tin Oxide covered Quartz Electrodes for Photo-Electrochemical Water Splitting, Electrochimica Acta, 131 (2014) 184-194 .

List of authors publications and conferences:

Publications:

1. Evaluation of the Parameters Affecting the Visible-Light-Induced Photocatalytic Activity of Monoclinic BiVO4 for Water Oxidation
   Sitaramanjaneya Thalluri, Conrado Martinez Suarez, Murid Hussain, Simelys Hernandez, Alessandro Virga, Guido Saracco, Nunzio Russo
   ·http://pubs.acs.org/doi/abs/10.1021/ie402930x
2. Elucidation of important parameters of $BiVO_4$ responsible for photo-catalytic O_2 evolution and insights about the rate of the catalytic process
   Sitaramanjaneya Mouli Thalluri,Conrado Martinez Suarez, Simelys Hernández, Samir Bensaida, Guido Saracco,Nunzio Russo
3. Green-Synthesized $BiVO_4$ Oriented along {040} Facets for Visible-Light-Driven Ethylene Degradation
   Sitaramanjaneya Mouli Thalluri, Murid Hussain, Guido Saracco, James Barber, and Nunzio Russo
4. Rapid synthesis of $BiVO_4$ thin films on FTO electrodes for water splitting under visible light irradiation
   Sitaramanjaneya Mouli Thalluri, Adriano Sacco, Samir Bensaid, Guido Saracco, Nunzio Russo and Simelys Hernández (Submitted to Chemical Engineering journal)
5. Doping of *$BiVO_4$* Powders Oriented along {040} Facets with Tungston and Molybdenum and Evaluation of their Performance by Photchemical and Photoelctro Chemical Characterizations
   In the process of manuscript preparation

Conference proceedings:

1. 15th International Congress on Catalysis 2012, Munich, Germany. "Metal-organic frameworks as water splitting photocatalysts", S. Vankova, C. Pagliano, E. Celasco, M. Thalluri, S. Hernandez, D. Hidalgo, G. Saracco, B. Onida, J. Barber. poster and short oral presentation
2. 17th International Zeolite conference-Moscow, Russia "Electrochemical Synthesis of cobalt containing Metal-Organic frameworks" S.K. Vankova, M. Cataldo Hernandez, M. Thalluri, N. Russo, G. Saracco.
3. Poster contribution in JEP 2013: "European symposium on Photocatalysis" 25-27th September 2013, Portoroz, Slovenia. "Optimization of dip coating procedure aiming towards an efficient BiVO4 photoanode", Thalluri. S. R. M, Vankova. S, Marinez Suarez. C, Russo. N, Saracco. G.
4. 2013 4th international conference on chemical engineering and Applications (CCEA2013). Oral presentation: "Insights from crystal size and band gap on the catalytic activity of monoclinic BiVO4.", Thalluri M., Martinez-Suarez C., Virga A., Russo N., Saracco G.
5. Oral presentation in the symposium of “THIN FILMS” of the “VII International Conference on Surfaces, Materials and Vacuum 2014, Cancun, Mexico”."Synthesis And Characterization Of BiVO4 Thin Films": Roberto Mirabal, Osmary Depablos- Rivera, Mouli Thalluri, Francoise LeMarrec, Sandra Rodil
6. Bismuth Vanadate Thin Films Produced By Dual Magnetron Sputtering, M Thalluri, R. Mirabal-Rojas, O. Depablos-Rivera, F. LeMarrec, S. E. Rodil, oral presentation at 16th International Conference on Thin Films, 2014, Croatia.